

Comptes Rendus Biologies



Volume 340, Issue 1, Pages 1-62

(January 2017)

Comptes Rendus
Biologies

Tome 340 (2017) – N° 1 – janvier



Cover illustration: A hand-coloured 19th-Century engraving by the famous bird illustrator J G Keulemans (1842–1912), showing a couple of *Meriones meridianus* (gerbil). Public domain. For further details, see N. Semiane et al., this issue, pp. 25–36.

Continued on the next page

Contents (continued)

Taxonomy / Taxinomie

Biodiversity / Biodiversité

Guide for authors: http://www.em-consulte.com/produit/crass3

Electronic Submission: http://ees.elsevier.com/crbiologies

C. R. Biologies 340 (2017) 1–6

Contents lists available at ScienceDirect

Comptes Rendus Biologies

www.sciencedirect.com



Molecular biology and genetics/Biologie et génétique moléculaires

Transcription factors regulating *uspA* genes in *Catharanthus roseus*



Ahmed Bahieldin [a,b,*], Ahmed Atef [a], Ahmed M. Shokry [a,c], Saleh Al-Karim [a], Sanaa G. Al Attas [a], Nour O. Gadallah [a,d], Sherif Edris [a,b,e], Magdy A. Al-Kordy [a,d], Sabah M. Hassan [a,b], Salah Abo-Aba [a,f], Fotouh M. El-Domyati [a,b]

[a] *Department of Biological Sciences, Faculty of Science, King Abdulaziz University (KAU), P.O. Box 80141, 21589 Jeddah, Saudi Arabia*
[b] *Department of Genetics, Faculty of Agriculture, Ain Shams University, Cairo, Egypt*
[c] *Agricultural Genetic Engineering Research Institute (AGERI), Agriculture Research Center (ARC), Giza, Egypt*
[d] *Genetics and Cytology Department, Genetic Engineering and Biotechnology Division, National Research Center, Dokki, Egypt*
[e] *Princess Al-Jawhara Al-Brahim Centre of Excellence in Research of Hereditary Disorders (PACER-HD), Faculty of Medicine, King Abdulaziz University (KAU), Jeddah, Saudi Arabia*
[f] *Microbial Genetics Department, Genetic Engineering and Biotechnology Division, National Research Centre, Giza, Egypt*

A R T I C L E   I N F O

Article history:
Received 10 June 2016
Accepted after revision 20 October 2016
Available online 24 November 2016

Keywords:
Transcription factor
Co-expression
Erf
BHLH
WRKY
RNA-Seq
SqRT-PCR

Abbreviations :
USP, universal stress protein
TF, transcription factor
bHLH, basic helix-loop-helix
ERF, ethylene responsive factor
sqRT-PCR, semi-quantitative RT-PCR
NCBI, National Center for Biotechnology Information
TIA, terpenoid indole alkaloid
DE, differentially expressed
iML, immature leaf

A B S T R A C T

RNA-Seq of the *Catharanthus roseus* SRA database was done in order to detect putative universal stress proteins (USPs) and their possible controlling factors. Previous analysis indicated the existence and characterization of *uspA*-like genes. *In silico* analysis of RNA-Seq database in several plant tissues revealed the possible functions and regulations of some *uspA*-like transcripts whose transcription factors (TFs) that might drive their expression were detected. BLAST indicated the existence of TF superfamilies erf (ethylene-responsive TF), bHLH (basic helix-loop-helix) and WRKY that might regulate several *uspA*-like genes. This data was proven via semi-quantitative RT-PCR in four plant tissues. Several of these transcription factor superfamilies are known for their action in the plant defense against biotic and abiotic stresses.

* Corresponding author. Department of Biological Sciences, Faculty of Science, King Abdulaziz University (KAU), P.O. Box 80141, Jeddah 21589, Saudi Arabia.

E-mail addresses: bahieldin55@gmail.com (A. Bahieldin), ahmed_atefaig2@yahoo.com (A. Atef), ahmedshokry1@gmail.com (A.M. Shokry), Skarim@kau.edu.sa (S. Al-Karim), sangtas@mit.edu (S.G. Al Attas), nouromar71@yahoo.com (N.O. Gadallah), sedris@aucegypt.edu (S. Edris), m_alkordy@yahoo.com (S.M. Hassan), sabmahmoud@yahoo.com (S. Abo-Aba), fm_domyati@hotmail.com (F.M. El-Domyati).

http://dx.doi.org/10.1016/j.crvi.2016.10.004
1631-0691/

ML, mature leaf
FL, flower
R, root
MTI, MAMP-triggered immunity
PTI, PAMP-triggered immunity
ETI, effector-triggered immunity
Trp, tryptophan
JA, jasmonic acid
SA, salicylic acid

1. Introduction

Vinca or *Catharanthus roseus* is an important medicinal plant species with several applications in pharmaceuticals and industry. This plant species is well known for the biosynthesis of two anticancer bisindole alkaloids, namely vinblastine and vincristine, produced during the terpenoid indole alkaloids (TIAs) pathway [1,2]. This wild plant species can tolerate several biotic and abiotic stresses [3,4]; hence, we screened its transcriptome for *usp*-like gene family that might act in conferring tolerance to such adverse conditions. Although the exact function of this gene family is unknown, it acts not only through improving tolerance to biotic and abiotic stresses, but also tolerance to other stresses, e.g., starvation and DNA damage [5].

The RNA-Seq data of different tissues that were deposited in the CathaCyc database come from a study originally conducted by Van Moerkercke et al. [6]. This database was previously utilized [7] for detecting and characterizing 24 *uspA*-like genes. Transcription factors (TFs) with known actions that might drive these *uspA*-like genes likely indicate the mode of action of these genes. TFs are key proteins required in the regulation of almost all biosynthetic pathways in life [8]. They bind to specific target DNA sequences controlling cellular transcription by either promoting or blocking the recruitment of RNA polymerase to the target genes. TFs usually bind directly to the target promoter regions; however, they sometimes bind to RNA polymerase. The action of TF directly affect downstream genes functioning at a particular time on target cells (gene-in-time/gene-in-site). They are also important in driving the plant's responses to biotic and abiotic stresses [9].

In the present study, an *in silico* analysis was conducted in order to detect the TFs that might regulate the expression of *uspA*-like genes in *C. roseus* in a trial to detect the possible role of these *uspA*-like genes under biotic and abiotic stresses.

2. Materials and methods

An RNA-seq analysis of *C. roseus* available at NCBI (http://www.ncbi.nlm.nih.gov/sra, experiment SRP005953) was conducted in order to detect TFs concordantly expressed with *uspA*-like genes that had been previously characterized [7]. The data were *de novo*-assembled using Trinity-RNAseq v (r2013_08_14), and the recovered transcripts were calculated for abundance and differential expression using the Rsem package and the edgR method [7]. Blast alignment was done as previously described [7], and the values of fpkm for the recovered *uspA*-like transcripts and their co-expressed transcripts were calculated. The resulted transcripts were clustered based on their expression patterns across different tissues, treatments and hairy root genotypes. Clusters were studied in order to detect TF transcripts co-expressed with *uspA*-like transcripts in *C. roseus*. A structural analysis was done for selected *C. roseus* TF transcripts frequently co-expressed with *uspA*-like transcripts.

To validate the RNA-Seq dataset of *C. roseus*, semi-quantitative RT-PCR (or sqRT-PCR) was conducted for seven transcripts of selected clusters. They included four *uspA*-like genes and three co-expressing TFs. RNAs were isolated from four pot-grown plant tissues (e.g., mature leaf, flower, root and stem) using the Trizol reagent method (Invitrogen) and treated with RNase-free DNase (Promega Inc.). Primers were designed using Netprimer software (http://www.premierbiosoft.com/netprimer/index.html) with the following criteria: length of 20–27 bases, GC content of ~50%, with minimal secondary structure, comparable annealing temperatures (48–55 °C) of the primer pairs, and PCR products of 281–300 bp (Table S1). sqRT-PCR was performed in forty cycles including denaturation at 94 °C for 15 s, annealing at 47–48 °C for 30 s, and extension at 72 °C for 45 s. Amounts of 1 ul cDNA, 1 × PCR buffer (with 1.5 mM $MgCl_2$), 200 uM dNTPs, 200 nM of each gene-specific primers and 0.2 U of *Taq* DNA polymerase (Promega Inc.) were used in the reaction. Amplicons were run on a 1.2% agarose gels stained with ethidium bromide and visualized using the Gel Doc XR from Bio-Rad Laboratories (Hercules, CA, <). The *actin* gene (250 bp) was used as the house-keeping control.

3. Results and discussion

RNA-Seq analysis of the *C. roseus* SRA database of different tissues resulted in the recovery of 50,723 transcripts that were calculated for abundance and differential expression. A number of 24 *uspA*-like transcripts were previously detected and characterized [7]. The *in silico* analysis of the present study resulted in the recovery of 1245 transcripts involving 13, out of the 24, *uspA*-like transcripts (Table S2). The rest of the transcripts were not regulated in different tissues of *C. roseus*, hence not presented in the clusters generated from the analysis. The regulated transcripts were shown in 12 clusters based on their expression patterns across different tissues. BLAST to detect hits in the NCBI indicated the occurrence of a large number of TFs mainly in the erf (ethylene-responsive TF), bHLH (basic helix-loop-helix) and WRKY gene

Table 1
Transcription factors in *Catharanthus roseus* assemblies and their NCBI protein and mRNA hits.

ID	Transcript ID	NCBI protein hit	Description
TF1	comp30166_c0	XP_004162335	*Cucumis sativus* ethylene-responsive transcription factor erf034-like mRNA
TF2	comp24014_c0	XP_004164936	*Cucumis sativus* ethylene-responsive transcription factor 5-like mRNA
TF3	comp30976_c0	XP_004173262	*Cucumis sativus* ap2-like ethylene-responsive transcription factor bbm2-like mRNA
TF4	comp16043_c0	XP_004169980	*Cucumis sativus* ethylene-responsive transcription factor erf008-like mRNA
TF5	comp10162_c0	XP_003521193	*Glycine max* transcription factor bhlh48-like mRNA
TF6	comp24246_c0	XP_004250124	*Solanum lycopersicum* transcription factor bhlh96-like mRNA
TF7	comp15693_c0	XP_006602463	*Glycine max* transcription factor bhlh78-like transcript variant mRNA
TF8	comp20416_c0	XP_011460603	Transcription factor bHLH106-like [*Fragaria vesca* subsp. vesca]
TF9	comp2848_c0	XP_006351643	*Solanum tuberosum* transcription factor bhlh155-like transcript variant mRNA
TF10	comp4341_c0	XP_006356833	*Solanum tuberosum* transcription factor bhlh74-like transcript variant mRNA
TF11	comp10042_c0	AJF11723	*Citrus sinensis* probable wrky transcription factor 40-like mRNA
TF12	comp11785_c0	XP_003534796	*Glycine max* probable wrky transcription factor 14-like transcript variant mRNA
TF13	comp3515_c1	XP_004235231	*Solanum lycopersicum* probable wrky transcription factor 70-like mRNA
TF14	comp20639_c0	XP_004165456	*Cucumis sativus* wrky transcription factor 72-like mRNA
TF15	comp21556_c0	XP_004504739	*Cicer arietinum* wrky transcription factor 9-like transcript variant mRNA
TF16	comp26488_c0	XP_004501445	*Cicer arietinum* wrky transcription factor 50-like mRNA
TF17	comp8026_c1	XP_004291261	*Fragaria vesca* wrky transcription factor 11-like mRNA

TF1–4: transcription factors with erf domain, TF5–10: transcription factors with bHLH domain, TF11–17: transcription factors with WRKY domain.

superfamilies. A number of 17 (four of erf, six of bHLH and seven of WRKY) TFs (see Table 1 for details) showed co-expression with six, out of the 13, *uspA*-like transcripts in five clusters, e.g., 4, 7, 8, 9 and 12 (Fig. 1 & Table S2). In cluster 4, the *uspA*-like transcript KJ634217 co-expressed with bHLH48. In cluster 7, the *uspA*-like transcripts KJ634222 and KJ634224 were in concordance with WRKY40, while the *uspA*-like transcript KJ634231 co-expressed with erf034. The *uspA*-like transcripts KJ634232 and KJ634221 co-expressed with a number of ten and five TFs of the three families, respectively. sqRT-PCR was used for validating the RNA-Seq dataset utilizing the selected co-expressing *uspA*-like and TF transcripts of clusters 4, 7 and 8 with varying expression levels in the four selected tissues, e.g., immature leaf (iML), mature leaf (ML), flower (FL), and root (R). The results concerning sqRT-PCR shown in Fig. 2 indicated an alignment with the RNA-Seq dataset (Table S2 and Fig. 1).

The AP-2 – or activating protein-2 of ethylene responsive (ER) TF – domain represents a superfamily of closely related TFs, which plays a critical role in regulating gene expression during the early development [10]. It was also shown to interfere with other signal transduction pathways [11,12]. Ethylene-responsive element-binding factors (ERFs) are a superfamily of transcriptional factors [13] that induce many developmental processes, and are also involved in the adaptation to biotic or abiotic stresses such as pathogen attack, wounding, UV irradiation, extreme temperature, and drought [14–16]. This TF is a key element in the integration of both signals for the regulation of defense response genes [17]. Recent studies have extended the influence of ethylene signaling with plant responses to both salt and water stress [18,19]. The erf8 and erf34 were reported in *Arabidopsis* and rice to be involved in the regulation of gene expression by stress factors and components of stress signal transduction pathways [13]. The erf was further reported to operate during the progression of leaf senescence [20], while erf5 was reported in *Arabidopsis* to regulate the chitin-induced innate immunity response [21]. Similar results were reached in tomato (*Solanum lycopersicum*), tobacco (*Nicotiana tabacum*), and *Arabidopsis* [22,23].

The information available for the basic helix-loop-helix (bHLH) superfamily indicates its existence in eukaryotes with numerous functions [24,25]. It can be responsible for the incoming regulatory signals from various cellular pathways and the direction of the transcriptional activity of a target gene [26]. The function of bHLH48 is not available, although this TF was characterized in a number of plant species including *Arabidopsis* (www.ncbi.nlm.nih.gov/gene/818831), rice (www.ncbi.nlm.nih.gov/gene/4341525), *Glycine max* (soybean) (www.ncbi.nlm.nih.gov/gene/100814124), corn (*Zea mays*) (www.maizegdb.org/gene_center/gene/bhlh48) and Jatropha (*Jatropha curcas*) (www.ncbi.nlm.nih.gov/gene/105634733). In *Arabidopsis*, bHLH74 was reported to regulate the expression of a subset of genes involved in cell expansion, while bHLH78 was reported to trigger flowering in response to blue light [27]. bHLH96 and bHLH155 have no known role, except that the expression of the first one was reported to be constitutive in roots, leaves, stems and flowers, while the second is involved in root development [24]. The bHLH106 was recently reported to participate in salt stress tolerance in *Arabidopsis* [28]. Knockout lines of this TF were more sensitive to NaCl, KCl, LiCl, ABA, and to low temperatures than the wild type.

The third type of TF, namely WRKY, is a member of a family of TFs functioning in plant responses to various physiological processes of vegetative and reproductive growth [29]. This type of TF is important in plant defense mechanisms, including MAMP-triggered immunity (MTI) or PAMP-triggered immunity (PTI), effector-triggered immunity (ETI), and systemic acquired resistance [30]. It was also proven to have a regulatory role in salt and mannitol stresses in *Arabidopsis* [31] and in cold and drought responses in barley (*Hordeum vulgare*) [32]. In addition, WRKY TFs regulate trichome and seed coat development in *Arabidopsis* [33], sesquiterpene biosynthesis in cotton (*Gossypium hirsutum*) [34], seed development in barley [35] and *Arabidopsis* [36], respectively, and

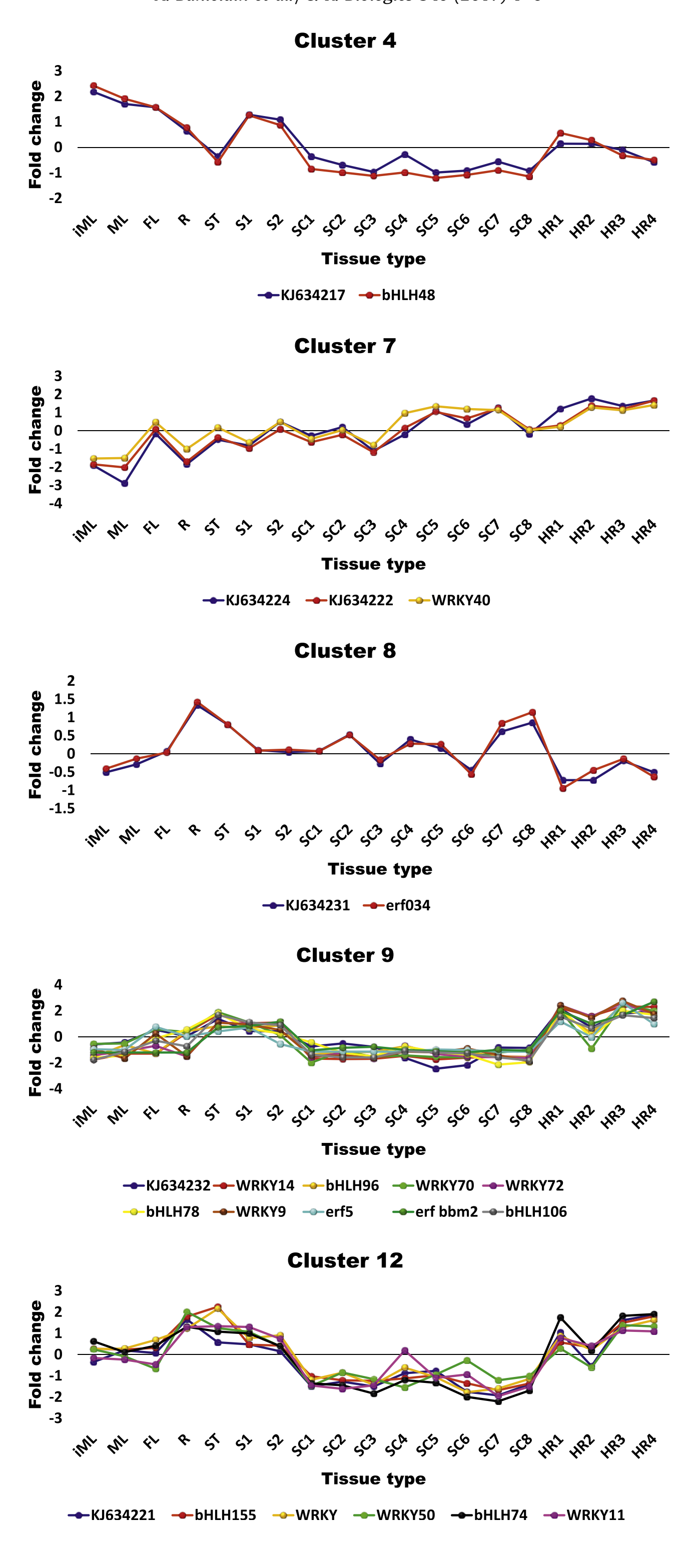


Fig. 1. Co-expression of *uspA*-like transcripts and putative transcription factors (see Table 1 for details) of erf, bHLH and WRKY superfamilies in clusters 4, 7, 8, 9 and 12 (see Table S2) across *Catharanthus roseus* plant tissues. iML: immature leaf, ML: mature leaf, FL: flower, R: root, ST: stem, S: seedling, SC: suspension culture, HR: hairy root. TF1–4: transcription factors with erf domain, TF5–10: transcription factors with bHLH domain, TF11–17: transcription factors with WRKY domain.

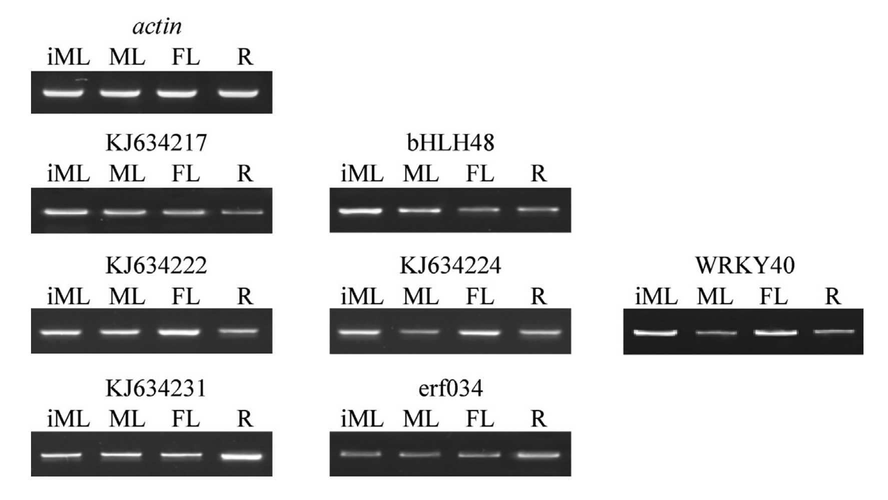


Fig. 2. Semi-quantitative RT-PCR used for validating RNA-Seq analysis for three transcription factors (bHLH48, WRKY40 and erf034) and four *uspA* (IDs KJ634217, KJ634222, KJ634224 and KJ634231) genes of clusters 4, 7 and 8. Complete description of different TFs and co-expressing *uspA*-like genes and their expression patterns in immature leaf (iML), mature leaf (ML), flower (FL) and root (R) are shown in Table S2 and Fig. 1. The *actin* gene was used as the house-keeping control. Amplicons were run against 100-bp ladder DNA standard (Bioron).

senescence in *Arabidopsis* [37]. The WRKY1 of tobacco [38], similar to WRKY9 in *Arabidopsis* [39], was reported to be phosphorylated by the MAPK, namely SIPK, in order to mediate HR-like cell death. The WRKY11 and WRKY70 were reported more recently to participate in regulating the signal transduction pathways involved in triggering induced systemic resistance in *Arabidopsis* [40]. The WRKY14 was reported to act as a key regulatory role in methanol-induced tryptophan (Trp) and Trp-derived secondary metabolite biosynthesis during senescence in rice leaves [41]. The WRKY40 participates as transcriptional regulator in ABA signal transduction in *Arabidopsis* [42]. In the presence of the signal, WRKY40 relocalises to the nucleoplasm. Interestingly, the relocalisation was not observed in response to other abiotic or biotic stimuli. Recent reports indicated that WRKY50 is involved in low oleic acid- and SA-derived repression of jasmonic acid (JA)-inducible defense responses in *Arabidopsis* [43]. The WRKY72 was reported to participate in basal immunity in tomato and *Arabidopsis*, while appeared to be largely non-responsive to the defense hormone salicylic acid (SA) [44].

In general, we anticipate that the information in the present study highlights the possible functions of *uspA*-like genes in *C. roseus* in terms of cell response to biotic and abiotic stress. This is because a number of *C. roseus uspA*-like transcripts co-expressed with many putative ethylene-responsive, bHLH or WRKY putative TFs, whose analogues of some of them are known for their action in the plant defense against biotic and abiotic stresses.

Acknowledgments

This project was funded by the Deanship of Scientific Research (DSR), King Abdulaziz University, Jeddah, under Grant No. (15-3-1432/HiCi). The authors, therefore, acknowledge with thanks technical and financial support from DSR.

Appendix A. Supplementary data

Supplementary data associated with this article can be found, in the online version, at http://dx.doi.org/10.1016/j.crvi.2016.10.004.

References

[1] S.K. Rijhwani, J.V. Shanks, Effect of elicitor dosage and exposure time on biosynthesis of indole alkaloids by *Catharanthus roseus* hairy root cultures, Biotech. Progress 14 (1998) 442–449.
[2] H. Rischer, M. Orešič, T. Seppänen-Laakso, M. Katajamaa, F. Lammertyn, et al., Gene-to-metabolite networks for terpenoid indole alkaloid biosynthesis in *Catharanthus roseus* cells, Proc. Natl. Acad. Sci. USA 103 (2006) 5614–5619.
[3] T. Nystrom, F.C. Neidhardt, Expression and role of the universal stress protein, UspA, of *Escherichia coli* during growth arrest, Mol. Microbiol. 11 (1994) 537–544.
[4] R. Van der Heijden, D.I. Jacobs, W. Snoeijer, D. Hallard, R. Verpoorte, The *Catharanthus* alkaloids: pharmacognosy and biotechnology, Curr. Med. Chem. 11 (2004) 1241–1253.
[5] W.T. Li, Y.M. Wei, J.R. Wang, C.J. Liu, X.J. Lan, et al., Identification, localization, and characterization of putative *USP* genes in barley, Theor. Applied Genet. 121 (2010) 907–917.
[6] A. Van Moerkercke, M. Fabris, J. Pollier, G.J.E. Baart, S. Rombauts, et al., CathaCyc, a metabolic pathway database built from *Catharanthus roseus* RNA-Seq data, Plant Cell Physiol. 54 (2013) 673–685.
[7] A. Bahieldin, A. Atef, A.M. Shokry, S. Al-Karim, S.G. Al Attas, et al., Structural identification of putative USPs in *Catharanthus roseus*, C. R. Biol. 338 (2015) 643–649.
[8] D.S. Latchman, Transcription factors: an overview, Int. J. Biochem. Cell Biol. 29 (1997) 1305–1312.
[9] S. Lindemose, C. O'Shea, M.K. Jensen, K. Skriver, Structure, function and networks of transcription factors involved in abiotic stress responses, Int. J. Mol. Sci. 14 (2013) 5842–5878.
[10] K. Hilger-Eversheim, M. Moser, H. Schorle, R. Buettner, Regulatory roles of AP-2 transcription factors in vertebrate development, apoptosis and cell-cycle control, Gene 260 (2000) 1–12.
[11] D. Eckert, S. Buhl, S. Weber, R. Jäger, H. Schorle, The AP-2 family of transcription factors, Genome Biol. 6 (2005) 246.
[12] Q. Li, R.H. Dashwood, Activator protein 2alpha associates with adenomatous polyposis coli/beta-catenin and inhibits beta-catenin/T-cell factor transcriptional activity in colorectal cancer cells, J. Biol. Chem. 279 (2004) 45669–45675.
[13] T. Nakano, K. Suzuki, T. Fujimura, H. Shinshi, Genome-wide analysis of the ERF gene family in *Arabidopsis* and rice, Plant Physiol. 140 (2006) 411–432.

[14] D. Hao, M. Ohme-Takagi, A. Sarai, Unique mode of GCC box recognition by the DNA-binding domain of ethylene-responsive element-binding factor (ERF domain) in plant, J. Biol. Chem. 273 (1998) 26857–26861.
[15] P.J. O'Donnel, C. Calvert, R. Atzorn, C. Wasternack, H.M.O. Leyser, et al., Ethylene as a signal mediating the wound response of tomato plants, Science 274 (1996) 1914–1917.
[16] I.A. Penninckx, K. Eggermont, F.R. Terras, B.P. Thomma, G.W. De Samblanx, et al., Pathogen-induced systemic activation of a plant defensin gene in Arabidopsis follows a salicylic acid-independent pathway, Plant Cell 8 (1996) 2309–2323.
[17] O. Lorenzo, R. Piqueras, J.J. Sánchez-Serrano, R. Solano, Ethylene response factor1 integrates signals from ethylene and jasmonate pathways in plant defense, Plant Cell 15 (2003) 165–178.
[18] Y.R. Cao, S.Y. Chen, J.S. Zhang, Ethylene signaling regulates salt stress response: an overview, Plant Signal. Behav. 3 (2008) 761–763.
[19] J. Cela, C. Chang, S. Munné-Bosch, Accumulation of γ- rather than α-tocopherol alters ethylene signaling gene expression in the vte4 mutant of *Arabidopsis thaliana*, Plant Cell Physiol. 52 (2011) 1389–1400.
[20] T. Koyama, H. Nii, N. Mitsuda, M. Ohta, S. Kitajima, et al., A regulatory cascade involving class II ethylene response factor transcriptional repressors operates in the progression of leaf senescence, Plant Physiol. 162 (2013) 991–1005.
[21] G.H. Son, J. Wan, H.J. Kim, X.C. Nguyen, W.S. Chung, et al., Ethylene-responsive element-binding factor 5, ERF5, is involved in chitin-induced innate immunity response, Mol. Plant Microbe Interact. 25 (2012) 48–60.
[22] H. Wang, Z. Huang, Q. Chen, Z. Zhang, H. Zhang, et al., Ectopic overexpression of tomato JERF3 in tobacco activates downstream gene expression and enhances salt tolerance, Plant Mol. Biol. 55 (2004) 183–192.
[23] C. Weiste, T. Iven, U. Fischer, L. Oñate-Sánchez, W. Dröge-Laser, *In planta* ORFeome analysis by large-scale over-expression of GATEWAY compatible cDNA clones: screening of ERF transcription factors involved in abiotic stress defense, Plant J. 52 (2007) 382–390.
[24] M.A. Heim, M. Jakoby, M. Werber, C. Martin, B. Weisshaar, et al., The basic helix-loop-helix transcription factor family in plants: a genome-wide study of protein structure and functional diversity, Mol. Biol. Evol. 20 (2003) 735–747.
[25] A.W. Moore, S. Barbel, L.Y. Jan, Y.N. Jan, A genomewide survey of basic helix-loop-helix factors in *Drosophila*, Proc. Natl. Acad. Sci. USA 97 (2000) 10436–10441.
[26] G. Toledo-Ortiz, E. Huq, P.H. Quail, The *Arabidopsis* basic/helix-loop-helix transcription factor family, Plant Cell 15 (2003) 1749–1770.
[27] Y. Liu, X. Li, K. Li, H. Liu, C. Lin, Multiple bHLH proteins form heterodimers to mediate CRY2-dependent regulation of flowering-time in *Arabidopsis*, Plos Genet. 9 (2013) e1003861.
[28] A. Ahmad, Y. Niwa, S. Goto, T. Ogawa, M. Shimizu, et al., bHLH106 integrates functions of multiple genes through their G-Box to confer salt tolerance on *Arabidopsis*, Plos One 10 (2015) e0126872.
[29] P.J. Rushton, I.E. Somssich, P. Ringler, Q.J. Shen, WRKY transcription factors, Trends Plant Sci. 15 (2010) 247–258.
[30] N. Ishihama, H. Yoshioka, Post-translational regulation of WRKY transcription factors in plant immunity, Curr. Opin. Plant Biol. 15 (2012) 431–437.
[31] L. Chen, Y. Song, S. Li, L. Zhang, C. Zou, et al., The role of WRKY transcription factors in plant abiotic stresses, Biochim. Biophys. Acta 1819 (2012) 120–128.
[32] C. Mare, E. Mazzucotelli, C. Crosatti, E. Francia, A.M. Stanca, et al., Hv-WRKY38: a new transcription factor involved in cold- and drought-response in barley, Plant Mol. Biol. 55 (2004) 399–416.
[33] C.S. Johnson, B. Kolevski, D.R. Smyth, *TRANSPARENT TESTA GLABRA2*, a trichome and seed coat development gene of Arabidopsis, encodes a WRKY transcription factor, Plant Cell 14 (2002) 1359–1375.
[34] Y.H. Xu, J.W. Wang, S. Wang, J.Y. Wang, X.Y. Chen, Characterization of GaWRKY1, a cotton transcription factor that regulates the sesquiterpene synthase gene (+)-delta-cadinene synthase-A, Plant Physiol. 135 (2004) 507–515.
[35] M. Luo, E.S. Dennis, F. Berger, W.J. Peacock, A. Chaudhury, MINISEED3 (MINI3), a WRKY family gene, and HAIKU2 (IKU2), a leucine-rich repeat (LRR) KINASE gene, are regulators of seed size in *Arabidopsis*, Proc. Natl. Acad. Sci. 102 (2005) 17531–17536.
[36] C. Sun, S. Palmqvist, H. Olsson, M. Boren, S. Ahlandsberg, et al., A novel WRKY transcription factor, SUSIBA2, participates in sugar signaling in barley by binding to the sugar-responsive elements of the iso1 promoter, Plant Cell 15 (2003) 2076–2092.
[37] Y. Miao, A. Smykowski, U. Zentgraf, A novel upstream regulator of WRKY53 transcription during leaf senescence in *Arabidopsis thaliana*, Plant Biol. (Stuttgart, Germany) Suppl. 1 (2008) 110–120.
[38] F.L. Menke, H.G. Kang, Z. Chen, J.M. Park, D. Kumar, et al., Tobacco transcription factor WRKY1 is phosphorylated by the MAP kinase SIPK and mediates HR-like cell death in tobacco, Mol. Plant Microbe Interact. 18 (2005) 1027–1034.
[39] H. Adachi, T. Nakano, N. Miyagawa, N. Ishihama, M. Yoshioka, et al., WRKY transcription factors phosphorylated by MAPK regulate a plant immune NADPH oxidase in *Nicotiana benthamiana*, Plant Cell 27 (2015) 2645–2663.
[40] C.H. Jiang, Z.Y. Huang, P. Xie, C. Gu, K. Li, et al., Transcription factors WRKY70 and WRKY11 served as regulators in rhizobacterium *Bacillus cereus* AR156-induced systemic resistance to *Pseudomonas syringae* pv. tomato DC3000 in *Arabidopsis*, J. Exp. Bot. 67 (2016) 157–174.
[41] K. Kang, S. Park, U. Natsagdorj, Y.S. Kim, K. Back, Methanol is an endogenous elicitor molecule for the synthesis of tryptophan and tryptophan-derived secondary metabolites upon senescence of detached rice leaves, Plant J. 66 (2011) 247–257.
[42] K. Geilen, M. Böhmer, Dynamic subnuclear relocalisation of WRKY40 in response to Abscisic acid in *Arabidopsis thaliana*, Sci. Rep. 5 (2015) (Article 13369).
[43] Q.M. Gao, S. Venugopal, D. Navarre, A. Kachroo, Low oleic acid-derived repression of jasmonic acid-inducible defense responses requires the WRKY50 and WRKY51 proteins, Plant Physiol. 155 (2011) 464–476.
[44] K.K. Bhattarai, H.S. Atamian, I. Kaloshian, T. Eulgem, WRKY72-type transcription factors contribute to basal immunity in tomato and Arabidopsis as well as gene-for-gene resistance mediated by the tomato R gene Mi-1, Plant J. 63 (2010) 229–240.

C. R. Biologies 340 (2017) 7–12

Contents lists available at ScienceDirect

Comptes Rendus Biologies

www.sciencedirect.com



Molecular biology and genetics/Biologie et génétique moléculaires

Expression of the *Galanthus nivalis* agglutinin (*GNA*) gene in transgenic potato plants confers resistance to aphids



Xiaoxiao Mi [a,b,c], Xue Liu [a,b], Haolu Yan [a,b], Lina Liang [a,b], Xiangyan Zhou [a,b], Jiangwei Yang [a,b], Huaijun Si [a,b], Ning Zhang [a,b,*]

[a] *Gansu Provincial Key Laboratory of Aridland Crop Science, Gansu Key Laboratory of Crop Genetic and Germplasm Enhancement, Gansu Agricultural University, Lanzhou 730070, People's Republic of China*
[b] *College of Life Science and Technology, Gansu Agricultural University, Lanzhou 730070, People's Republic of China*
[c] *The Eighth Middle School of Tianshui City, Tianshui 620500, Gansu Province, People's Republic of China*

ARTICLE INFO

Article history:
Received 20 July 2016
Accepted after revision 23 October 2016
Available online 7 December 2016

Keywords:
Aphid
GNA
Transgenic potato
Insect resistance
Leaf and stem-specific promoter

ABSTRACT

Aphids, the largest group of sap-sucking pests, cause significant yield losses in agricultural crops worldwide every year. The massive use of pesticides to combat this pest causes severe damage to the environment, putting in risk the human health. In this study, transgenic potato plants expressing *Galanthus nivalis* agglutinin (*GNA*) gene were developed using CaMV 35S and ST-LS1 promoters generating six transgenic lines (35S1-35S3 and ST1-ST3 corresponding to the first and second promoter, respectively). Quantitative real-time polymerase chain reaction (qRT-PCR) analysis indicated that the *GNA* gene was expressed in leaves, stems and roots of transgenic plants under the control of the CaMV 35S promoter, while it was only expressed in leaves and stems under the control of the ST-LS1 promoter. The levels of aphid mortality after 5 days of the inoculation in the assessed transgenic lines ranged from 20 to 53.3%. The range of the aphid population in transgenic plants 15 days after inoculation was between 17.0 ± 1.43 (ST2) and 36.6 ± 0.99 (35S3) aphids per plant, which corresponds to 24.9–53.5% of the aphid population in non-transformed plants. The results of our study suggest that GNA expressed in transgenic potato plants confers a potential tolerance to aphid attack, which appears to be an alternative against the use of pesticides in the future.

1. Introduction

Aphids are considered as the largest group of sap-sucking pests that cause significant yield losses in agricultural crops worldwide [1–3]. They induce damage to their host plants, modifying plant metabolism, ingesting plant nutrients from the phloem, and vectoring plant-pathogenic viruses [4,5]. *Macrosiphum euphorbiae* (Thomas), and *Myzus persicae* (Sulzer) aphid species constitute one of the major potato pests affecting the production of this crop [6], which is considered the fourth most important worldwide [7].

Despite the improvement of biopesticides like toxins derived from entomopathogenic fungus [8] and bacteria [9], and spiders venom [10] that have specificity for target pest species [11] and do not affect mammals [12], these substances remain in the epidermis, being effective only for crewing insects. Notwithstanding the fact they combat aphids, which are able to penetrate their long acupuncture mouthparts into plant phloem, it is necessary to search for effective substances that must be able to reach these active sites with a long-time permanence and low digestion ratio

* Corresponding author. Gansu Provincial Key Laboratory of Aridland Crop Science, Gansu Key Laboratory of Crop Genetic and Germplasm Enhancement, Gansu Agricultural University, Lanzhou 730070, People's Republic of China.
E-mail address: ningzh@gsau.edu.cn (N. Zhang).

http://dx.doi.org/10.1016/j.crvi.2016.10.003
1631-0691/

once it has been ingested by the insect. One candidate substance that complies with the aforementioned requirement is the snowdrop lectin *Galanthus nivalis* agglutinin (GNA), which is able to cross the midgut epithelium [13] remaining stable and active within the insect gut after having been ingested. It has been reported that GNA confers resistance to crewing and sap-sucking insects in rice, tobacco, cotton, rape, and wolfberry [14–16], without toxicity to higher animals [17]. The use of genetic engineering that allows the synthesis of GNA to improve the resistance of important crops like potato to aphids is yet a pending issue that needs to be implemented.

Transgenic technology has allowed the expression of a broad spectrum of promoters, which potentially are involved in the synthesis of lectins, one of them, the CaMV 35S promoter, is most widely used in transgenic plants, since it not only affects the associated transgene, but also exerts influence in thousands of base pairs up- or downstream of the insertion site on a given chromosome [18,19]. However, the foreign gene, driven by CaMV 35S promoter, is expressed in all tissues during plant growth and development [20]. It causes consumption of excessive matter and energy within the cells for the expression of the target gene, affecting its temporal and spatial effectiveness [21]. Furthermore, there are other promoters that are only expressed in photosynthetic tissues; this is the case of ST-LS1, a light-inducible promoter whose expression has been detected in leaves and photosynthetic stems of potato [22–24]. In the present study, the transgenic potato plants expressing *GNA* gene driven by CaMV 35S and ST-LS1 promoters respectively were obtained to find the difference of tissue-specific expression and to estimate the resistance of the transgenic potato plants to aphids. Our aims were to obtain the transgenic potato plants expressing the *GNA* gene driven by CaMV 35S and ST-LS1 promoters, respectively, to find the difference of the tissue-specific expression of the *GNA* gene and further to improve the resistance of potato to aphids.

2. Materials and methods

2.1. Plants and insects

The potato cv. 'Atlantic' was propagated *in vitro* by subculturing single-node cuttings on Murashige and Skoog medium [25] supplemented with 3% sucrose and 0.45% agar. Plantlets were grown in 150-mL flasks under white fluorescent light during 16 h and in the dark during 8 h, at a temperature of 24 ± 2 °C. Microtubers were induced in the dark at 24 ± 2 °C in an MS medium supplemented with 8% sucrose and 0.45% agar [26]. Green peach aphids (*M. persicae*, Sulzer) were collected from Yuzhong County in Gansu Province, China. Aphids were reared in a light incubator at 25 ± 2 °C under a 14 h light/10 h dark photoperiod, and fed with plantlets of potato cv. 'Atlantic'.

2.2. Construction of the plant expression vector

The fragment of *GNA* gene with nucleotide sequence (GenBank accession No. M55556.1) [27] was digested with *Bam*H I and *Sal* I from the clone vector and ligated into a binary vector pBI121 [28] and pBI121-ST-LS1 [24] resulting in the recombinant vectors pBI121-CaMV35S-GNA and pBI121-ST-LS1-GNA. These vectors were transformed into *Escherichia coli* DH5α respectively, and further verified by the same restriction endonuclease digestion. After that, pBI121-CaMV35S-GNA and pBI121-ST-LS1-GNA were transformed into *Agrobacterium tumefaciens* LBA4404, respectively, using the freeze-thaw method [29].

2.3. Transformation of potato

Potato transformation was performed according to the protocol of Si et al. [30]. Microtuber slices of potato cv. 'Atlantic' were co-cultured (media-MS + 1 mg/L IAA + 0.2 mg/L GA_3 + 0.5 mg/L 6-BA + 2 mg/L ZT) for 2 days with *A. tumefaciens* LBA4404 containing the plasmid pBI121-CaMV35S-GNA and pBI121-ST-LS1-GNA, respectively, then transferred into a selection media supplemented with 50 mg/L kanamycin. When green buds sprouted from the surface of the slices and reached a length of 1 cm, they were transferred to a selective rooting medium containing 100 mg/L of kanamycin and 200 mg/L of carbenicillin. Plantlets with well-developed roots were propagated for further molecular analysis.

High-quality DNA was isolated from the leaves of putatively transformed and non-transformed (NT) control potato plants for PCR according to the method proposed by Edwards et al. [31]. The part of the coding sequence of the *GNA* gene was amplified using a PCR Screening Kit (GenStar, Beijing, China) with forward primer (5′-GCGGATCCATGGCTAAGGCAAGTCTCC-3′) and reverse primer (5′-GTACGAGCTCTTACTTTGCCGTCACAAGCT-3′). Amplification was performed in a thermal cycler (T100^{TM}, BIO-RAD) programmed for one cycle of 3 min at 94 °C followed by 30 cycles of 30 s at 94 °C, 30 s at 66 °C, and 1 min at 72 °C. A final extension step was performed for 5 min at 72 °C. The amplification products with 500 bp in length were separated by electrophoresis on 1.0% agarose gels treated with GoldView II staining.

2.4. Gene expression analysis by qRT-PCR

Total RNAs were isolated from the transgenic lines and NT control using RNAsimple Total RNA Kit (lot#N2822, TIANGEN, Beijing, China) following the manufacturer's instructions. Reverse transcription was performed in 20 μL reaction mixture with the RevertAid First Strand cDNA Synthesis Kit (Cat No: 3K1622, Thermo Scientific) and qRT-PCR amplification was performed in 20 μL of the reaction mixture with the SuperReal PreMix Plus (SYBR Green) (lot#N3113, TIANGEN, Beijing, China), 10 μM of each primer (*ef1a* as an internal control gene and forward and reverse primers: 5′-CAAGGATGACCCAGCCAAG-3′ and 5′-TTCCTT ACCTGAACGCCTGT-3′, and the gene-specific forward and reverse primers: 5′-CTCACCACTTACGCACAAGC-3′ and 5′-CGGCAATATCCTCTTTCTCG-3′). Reactions were conducted with an ABI3000 device (Applied Biosystems 3000 Real-Time PCR System) using the default cycling conditions (30 s at 95 °C and 40 cycles of 95 °C for 5 s, 60 °C for 34 s, 15 s at 95 °C, 1 min at 60 °C and 95 °C for 15 s). Each experiment was repeated three times independently. After



Fig. 1. Insect bioassay setup was used to identify the resistance to aphids of the transgenic potato plants and NT. Left: insect bioassay setup. Right: enlarged view of the being tested potato plants. Inset in A shows aphid culture on potato plants. The bar represents 5 mm.

each reaction, dissociation curve analysis was carried out to verify the specificity of the amplification and $2^{-\Delta\Delta Ct}$ was used to calculate the relative expression levels.

2.5. Evaluation of resistance of the transgenic potato plants to aphids

Insect resistance bioassays were performed according to the method described by Cooper et al. [32] and Du et al. [33]. Thus, a 75-mm-long sample from the top of the stem was detached from 25-day-grown transgenic and NT plants. Stem wounds were wrapped in a wet tampon and each plant was placed into a glass cage (65 mm in diameter, 90 mm in height) (Fig. 1A). The plants were inoculated with two aphid larvae in the first-instar larva state. Five plants were used per transgenic individual and control plant. Three replications were performed for each individual line. All the cages were placed in the illumination incubator (LRH-300-G) at 24 ± 1 °C. The survival of insects within the cages was monitored at an interval 24 h for 15 days (Fig. 1B). The mean survival and mortality per plant was calculated as the numbers of surviving and dead (in the four days following inoculation) aphids per day. ANOVA followed by Duncan's multiple-range tests were conducted to compare differences in mortality and survival rate among transgenic and NT control plants for the insect bioassay experiment.

3. Results

3.1. Potato transformation and GNA gene expression analysis by qRT-PCR

After three weeks of infection with *A. tumefaciens* LBA4404 containing the plasmid pBI121-CaMV35S-GNA

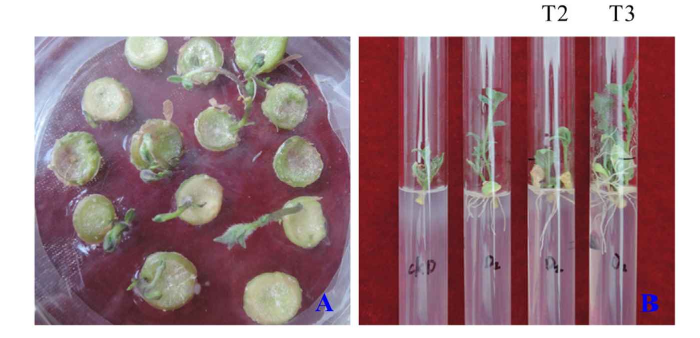


Fig. 2. Potato transformation. A. Shoot formation directly from transgenic microtuber discs of potato cv. 'Atlantic' after three weeks of culture in a selective medium (MS + 1 mg/L IAA + 0.2 mg/L GA3 + 0.5 mg/L 6-BA + 2 mg/L ZT + 50 mg/L kanamycin + 200 mg/L carbenicillin) and incubated under a photoperiod with 16 h light/8 h dark cycles at 24 °C. B. Roots were formed in about 10 days when green shoots were transferred to the selective rooting medium (MS + 100 mg/L kanamycin + 200 mg/L carbenicillin). NT: non-transformed potato plant as a negative control; T1-T3: three transgenic potato plants.

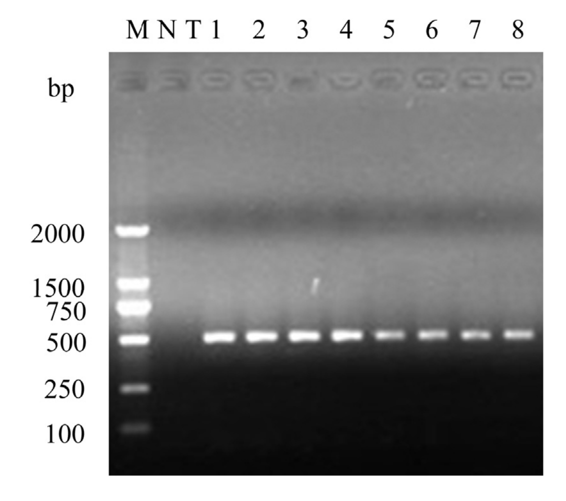


Fig. 3. Transgenic potato plants verification by PCR assay. M: DL2000 marker (TaKaRa); NT: non-transformed potato plant as negative control; 1: plasmid pBI121-CaMV35S-GNA as positive control; 2–8: seven transgenic potato plants.

and pBI121-ST-LS1-GNA respectively, green buds sprouted from the surface of the microtuber slices (Fig. 2A). Roots were formed in about 10 days (Fig. 2B) when the buds were transferred to a selective rooting media. PCR assay demonstrated that transformed plants showed a 500 bp amplification product, whereas no product was found in NT plants (Fig. 3). Here, we selected three transgenic lines 35S1-35S3 from the CaMV 35S promoter and three transgenic lines from the ST-LS1 promoter for further analysis. qRT-PCR analysis showed that the *GNA* gene was expressed in roots, stems and leaves of the transgenic potato plants transformed with pBI121-CaMV35S-GNA containing the constitutive promoter CaMV 35S (Fig. 4). However, in the transformation carried out by pBI121-ST-LS1-GNA, the *GNA* gene was expressed in all the organs except roots. *GNA* gene expression was higher in leaves than in stems of the transgenic plants (Fig. 4).

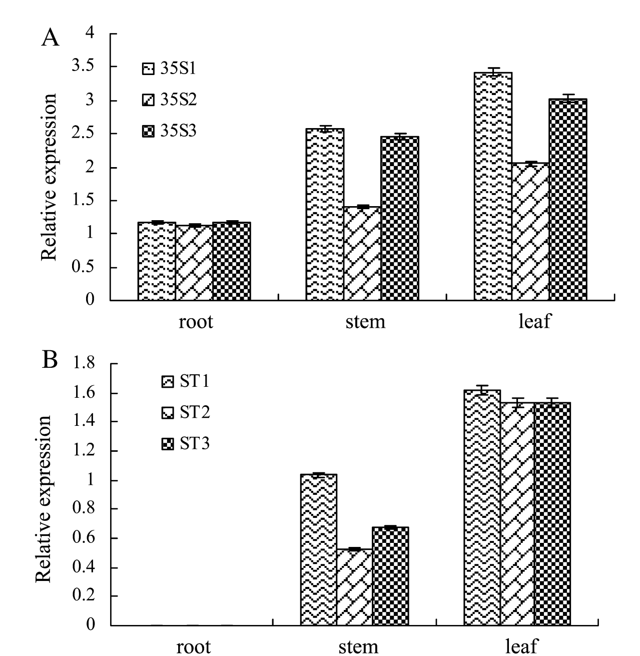


Fig. 4. Tissue-specific expression assay of *GNA* gene in the transgenic potato plants by qRT-PCR. A. Transgenic potato plants transformed with pBI121-CaMV35S-GNA. 35S1–35S3 are three different transgenic plant lines. B. Transgenic potato plants transformed with pBI121-ST-LS1-GNA. ST1-ST3 corresponds to different transgenic plant lines. Error bars indicate standard deviations obtained from three independent replicates.

3.2. *Bioassay of resistance of the transgenic potato plants to aphids*

3.2.1. *Aphid mortality analysis*

The aphid mortality levels after 5 days of inoculation in the transgenic lines ranged between 20 (35S1) and 53.3% (ST1) (Fig. 5). Differences (at $P < 0.05$) in the mortality level against the NT control were found, except for 35S1 and 35S2 lines.

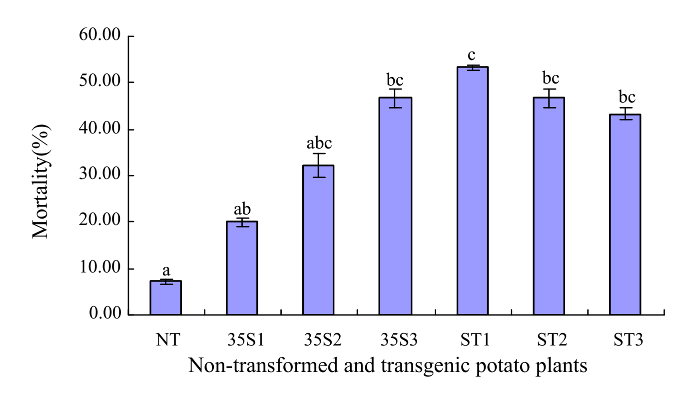


Fig. 5. Mortality analysis of first-instar larvae in the first five days following the inoculation in non-transformed and transgenic potato plants. NT: non-transformed potato plant; 35S1–35S3: transgenic plants driven by the CaMV 35S promoter; ST1–ST3: transgenic plants driven by the ST-LS1 promoter. Different small letters indicated a significant difference at $P < 0.05$ by Duncan's multiple-range test. Error bars indicate the standard deviations obtained from three independent replicates.

3.2.2. Aphid survival analysis

The aphid population on NT plants increased at a steady rate and soared up to a maximum of 68.3 ± 0.95 individuals per plant (Fig. 6). On transgenic lines, the aphid population increased more slowly than NT and rose to a maximum ranged from 17.0 ± 1.43 (ST2) to 36.6 ± 0.99 (35S3) individuals per plant, which corresponded from 24.9 to 53.5% of NT aphid population (Fig. 6).

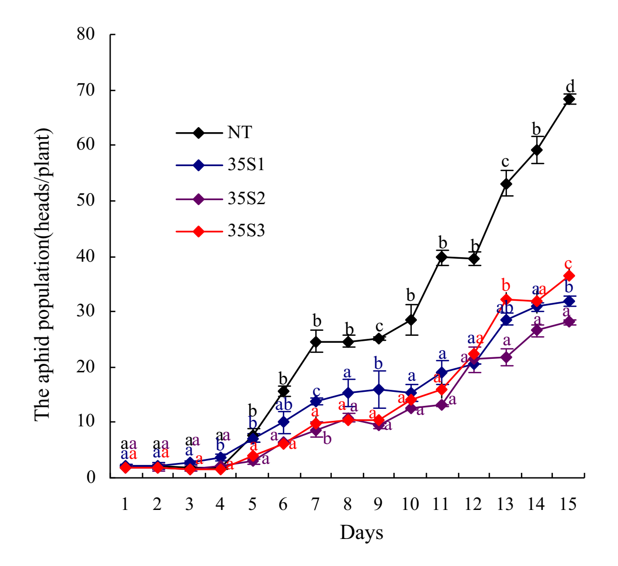
4. Discussion

Potato is the world's fourth-largest food crop, following maize, wheat, and rice. Because it supplies dietary fibers, carbohydrates, high quantities of proteins, vitamins and minerals, potato is usually regarded as a starchy food or a vegetable. China is one of the largest potato-producers worldwide. Aphids significantly impact agricultural and horticultural crops, either by causing direct damage to plants through feeding on the phloem, or indirectly by acting as vectors for plant-pathogenic viruses [34]. There are many measures, such as genetic engineering, which have been applied to reduce the damage caused by aphids to crops [10,35–37]. Aphids hinder worldwide potato production; therefore, to effectively control the damage of the aphid has become an important issue in potato production.

Since the snowdrop lectin (GNA) was separated in 1987 [38], its encoded gene was cloned and applied to plant genetic engineering [27]. Because of lacking receptors in mammals, GNA is relatively safe to the human body. Compared with pesticide residue and ecological destruction caused by the long-term use of chemical pesticides, GNA is regarded as the safer and more efficient approach to reduce the damage for crops against insects. In our experiment, the result showed that *GNA* could express in the transgenic potato plants and represent high mortality to aphid. It was found that the quantity of aphids on the transgenic potato plants was far less than on non-transgenic plants.

Similar to other phloem-specific promoters (RSs, ubi1) with insecticidal effects in sap-sucking homopteran [14], our study detected insecticidal effects toward the green peach aphid *M. persicae* (Sulzer) in transgenic potato plants with CaMV 35S and ST-LS1 promoters. However, the result from qRT-PCR assay showed that the expression of the *GNA* gene driven by the ST-LS1 promoter in the transgenic plants was higher in leaves than in stems, and no expression in roots (Fig. 4), and even the highest mortality (ST1) and lowest survival (ST2) of aphids were found in lines generated with this promoter.

Because tuber is the edible portion of potato, in accordance with our results, we hypothesize a no or less expression of *GNA* driven by ST-LS1 promoter in this organ of transgenic potato plants, guaranteeing a more safety to its use as food. However, this hypothesis will have to be tested in the future. Moreover, our study has been done *in vitro* conditions in plantlets, so it is needed to further grow plants in the field to assay their resistance to aphids. In addition, as potato is not the only plant-hosting aphids in China, the protection of other aphid hosts must be taken into consideration in order to prevent and control the damage caused by aphids for potato.



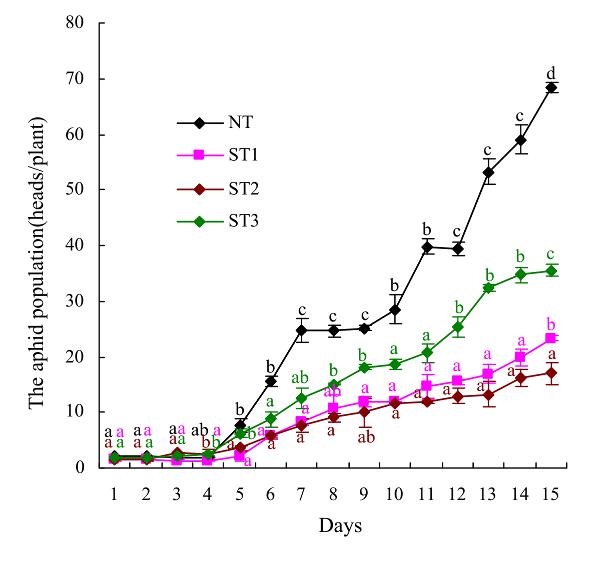


Fig. 6. Survival analysis of the aphid population during the first 15 days after inoculation with first-instar aphid larvae. NT: non-transformed potato plant; 35S1–35S3: transgenic plants driven by CaMV 35S promoter; ST1–ST3: transgenic plants driven by the ST-LS1 promoter. Different small letters indicate a significant difference at $P < 0.05$ by Duncan's multiple-range test. Error bars indicate the standard deviations obtained from three independent replicates.

Acknowledgements

This work was supported by the Agriculture Science and Technology Innovation Project of Gansu Province, China (GNCX-2011-49). We would like to thank Dr. Jiahe Wu (Institute of Microbiology, Chinese Academy of Sciences, Beijing, China) for kindly provided the vector of *GNA* gene and Dr. David A. Ramírez (International Potato Center, Lima, Peru) for editing the manuscript and valuable discussion.

References

[1] S.M. Guo, L.G. Kamphuis, L.L. Gao, J.P. Klingler, J. Lichtenzveig, O. Edwards, K.B. Singh, Identification of distinct quantitative trait loci associated with defence against the closely related aphids *Acythosiphon pisum* and *A. kondo* in *Medicago truncatula*, J. Exp. Bot. 63 (2012) 3913–3922.

[2] L.G. Kamphuis, J. Lichtenzveig, K. Peng, S.M. Guo, J.P. Klingler, K.H. Siddique, K.B. Singh, Characterization and genetic dissection of resistance to spotted alfalfa aphid (*Therioaphis trifolii*) in *Medicago truncatula*, J. Exp. Bot. 64 (2013) 5157–5172.

[3] D. Wang, Q. Liu, H.D. Jones, T. Bruce, L. Xia, Comparative transcriptomic analyses revealed divergences of two agriculturally important aphid species, BMC Genomics 15 (2014) 1023.

[4] P.J. Moran, G.A. Thompson, Molecular responses to aphid feeding in *Arabidopsis* in relation to plant defence pathways, Plant Physiol. 125 (2001) 1074–1085.

[5] C. Couldridge, H.J. Newbury, B.F. Lloyd, J.B.J. Pritchard, Exploring plant responses to aphid feeding using a full *Arabidopsis* microarray reveals a small number of genes with significantly altered expression, Bull. Entomol. Res. 97 (2007) 523–532.

[6] Y. Pelletier, D. Michaud, Insect pest control on potato: genetically-based control, in: R.M. Duchesne, G. Boiteau (Eds.), Potato insect pest control: development of a sustainable approach, Gouvernement du Québec, 1995, pp. 69–79.

[7] Food and Agriculture Organization of the United Nations (FAO), World crop production statistics, 2016 http://www.faostat.fao.org , . Accessed 10th September 2016.

[8] W. Liu, Y. Xie, J. Dong, J. Xue, Y. Zhang, Y. Lu, J. Wu, Pathogenicity of three entomopathogenic fungi to *Matsucoccus matsumurae*, PLoS One 9 (2014) e103350.

[9] F. Wang, Y. Liu, F. Zhang, L. Chai, L. Ruan, D. Peng, M. Sun, Improvement of crystal solubility and increasing toxicity against *Caenorhabditis elegans* by asparagine substitution in block 3 of *Bacillus thuringiensis* crystal protein Cry5Ba, Appl. Environ. Microbiol. 78 (2012) 7197–7204.

[10] J.R. Bloomquist, Mode of action of atracotoxin at central and peripheral synapses of insects, Invert. Neurosci. 5 (2003) 45–50.

[11] P.R. Whitehorn, S.O. Connor, F.L. Wackers, D. Goulson, Neonicotinoid pesticide reduces bumble bee colony growth and queen production, Science 336 (2012) 351–352.

[12] S.S. Pineda, D. Wilson, J.S. Mattick, G.F. King, The lethal toxin from Australian funnel-web spiders is encoded by an intronless gene, PLoS One 7 (2012) e43699.

[13] A.M. Gatehouse, J.A. Gatehouse, M. Bharathi, J. Spence, K.S. Powell, Immunohistochemical and developmental studies to elucidate the mechanism of action of the snowdrop lectin on the rice brown plant hopper, *Nilaparvata lugens* (Stal), J. Insect Physiol. 44 (1998) 529–539.

[14] K.V. Rao, K.S. Rathore, T.K. Hodges, X. Fu, E. Stoger, D. Sudhakar, Expression of snowdrop lectin (GNA) in transgenic rice plants confers resistance to rice brown plant hopper, Plant J. 15 (1998) 469–477.

[15] V.A. Hilder, K.S. Powell, A.M.R. Gatehouse, J.A. Gatehouse, L.N. Gatehouse, Y. Shi, W.J. Peumans, Expression of snowdrop lectin in transgenic tobacco plants results in added protection against aphids, Transgenic Res. 4 (1995) 18–25.

[16] X. Foissac, N.T. Loc, P. Christou, A.M. Gatehouse, J.A. Gatehouse, Resistance to green leaf hopper (*Nephotettix virescens*) and brown plant hopper (*Nilaparvata lugens*) in transgenic rice expressing snowdrop lectin (*Galanthus nivalis* agglutinin; GNA), J. Insect Physiol. 46 (2000) 573–583.

[17] A.M.R. Gatehouse, K.S. Powell, E.J.M.V. Damme, W.J. Peumans, Insecticidal properties of plant lectins: their potential in plant protection, in: A. Pusztai, S. Bardocz (Eds.), Lectins: Biomedical Perspectives, Taylor & Francis, London, 1995, pp. 35–57.

[18] A. Wilmink, B.C.D. Ven, J.J. Dons, Activity of constitutive promoters in various species from the *Liliaceae*, Plant Mol. Biol. 28 (1995) 949–955.

[19] C. Potenza, L. Aleman, C. Sengupta-Gopalan, Targeting transgene expression in research, agricultural, and environmental applications: promoters used in plant transformation, In Vitro Cell. Dev. Bio-Plant 40 (2004) 1–22.

[20] J.T. Odell, F. Nagy, N.H. Chua, Identification of DNA sequences required for activity of the cauliflower mosaic virus 35S promoter, Nature 313 (1985) 810–812.

[21] J.R. Gittins, T.K. Pellny, E.R. Hiles, C. Rosa, S. Biricolti, D.J. James, Transgene expression driven by heterologous ribulose-1,5-bisphosphate carboxylase/oxygenase small-subunit gene promoters in the vegetative tissues of apple (*Malus pumila* mill.), Planta 210 (2000) 232–240.

[22] J. Stockhaus, J. Schell, L. Willmitzer, Correlation of the expression of the nuclear photosynthetic gene ST-LS1 with the presence of chloroplasts, EMBO J 8 (1989) 2445–2451.

[23] P. Eckes, S. Rosahl, J. Schell, L. Willmitzer, Isolation and characterization of a light-inducible, organ-specific gene from potato and analysis of its expression after tagging and transfer into tobacco and potato shoots, Mol. Gen. Genet. 205 (1986) 14–22.

[24] Y. Qu, N. Zhang, J. Chang, X. Jin, Y.K. Wen, H.J. Si, D. Wang, Cloning and functional analysis of light-inducible, and stem and leaf-specific expression promoter ST-LS1 in potato (*Solanum tuberosum* L.), J. Agri. Biotechnol. 21 (2013) 828–837.

[25] T. Murashige, F. Skoog, A revised medium for rapid growth and bioassays with tobacco tissue cultures, Physiol. Plant. 15 (1962) 473–497.

[26] N. Zhang, H.J. Si, D. Wang, Cloning of rd29A gene promoter from *Arabidopsis thaliana* and its application in stress-resistance transgenic potato, Acta Agro. Sin. 31 (2005) 159–164.

[27] E.J.V. Damme, H. Kaku, F. Perini, I.J. Goldstein, B. Peeters, F. Yagi, B. Decock, W.J. Peumans, Biosynthesis, primary structure and molecular cloning of snowdrop (*Galanthus nivalis* L.) lectin, Eur. J. Biochem. 202 (1991) 23–30.

[28] T.Y. Li, Y.C. Tian, X.F. Qing, Studies on high-efficient insect resistance transgenic tobacco, China Sin. (B). 24 (1994) 268–276.

[29] R. Hofgen, L. Willmitzer, Storage of competent cells for *Agrobacterium* transformation, Nucleic Acid Res. 16 (1988) 9877.

[30] H.J. Si, C.H. Xie, J. Liu, An efficient protocol for *Agrobacterium*-mediated transformation of microtuber and the introduction of antisense class I patatin gene into potato, Acta Agro. Sin. 29 (2003) 801–805.

[31] K. Edwards, C. Johnstone, C. Thompson, A simple and rapid method for the preparation of genomic DNA for PCR analysis, Nucleic Acids Res. 16 (1991) 1349.

[32] S.G. Cooper, D.S. Douches, E.J. Grafius, Combining genetic engineering and traditional breeding to provide elevated resistance in potatoes to Colorado potato beetle, Entomol Exp. Appl. 112 (2004) 37–46.

[33] J.L. Du, D.G. Wu, T.W. Zhang, X.J. Qian, C.Z. Liu, Effect of UV-B for different radiation durations on biological characteristics of two color morphs of pea aphid *Acyrthosiphon pisum* (Harris) offspring, Acta Agrestia Sin. 20 (2012) 961–966.

[34] E.Y. Nakasu, M.G. Edwards, E. Fitches, J.A. Gatehouse, A.M. Gatehouse, Transgenic plants expressing ω-ACTX-Hv1a and snowdrop lectin (GNA) fusion protein show enhanced resistance to aphids, Front Plant Sci. 5 (2014) 673.

[35] C.J. Burns, L.J. McIntosh, P.J. Mink, A.M. Jurek, A.A. Li, Pesticide exposure and neurodevelopmental outcomes: review of the epidemiologic and animal studies, J. Toxicol. Environ. Health B Crit. Rev. 16 (2013) 127–283.

[36] T. Blacquière, G. Smagghe, C.A.V. Gestel, V. Mommaerts, Neonicotinoids in bees: a review on concentrations, side-effects and risk assessment, Ecotoxicology 21 (2012) 973–992.

[37] K. Derecka, M.J. Blythe, S. Malla, D.P. Genereux, A. Guffanti, P. Pavan, D.A. Barrett, Transient exposure to low levels of insecticide affects metabolic networks of honeybee larvae, PLoS One. 8 (2013) e68191.

[38] E.J.V. Damme, A.K. Allen, W.J. Peumans, Isolation and characterization of a lectin with exclusive specificity towards mannose from snowdrop (*Galanthus nivalis* L.) bulbs, FEBS Lett. 215 (1987) 140–144.

C. R. Biologies 340 (2017) 13–17

Contents lists available at ScienceDirect

Comptes Rendus Biologies

www.sciencedirect.com



Molecular biology and genetics/Biologie et génétique moléculaires

Age-related changes of metallothionein 1/2 and metallothionein 3 expression in rat brain



Rosaria Scudiero *, Luisa Cigliano, Mariailaria Verderame

Department of Biology, University of Naples Federico II, via Mezzocannone 8, 80134 Napoli, Italy

ARTICLE INFO

Article history:
Received 13 October 2016
Accepted after revision 15 November 2016
Available online 8 December 2016

Keywords:
Brain aging
Metallothionein isoforms
MT1/2 and *MT3* gene expression
Rattus
Real-time PCR

ABSTRACT

Neurodegeneration is one of the main physiological consequences of aging on brain. Metallothioneins (MTs), low molecular weight, cysteine-rich proteins that bind heavy-metal ions and oxygen-free radicals, are commonly expressed in various tissues of mammals. MTs are involved in the regulation of cell proliferation and protection, and may be engaged in aging. Expression of the ubiquitous MTs (1 and 2) and the brain specific MT3 have been studied in many neurodegenerative disorders. The research results indicate that MTs may play important, although not yet fully known, roles in brain diseases; in addition, data lack the ability to identify the MT isoforms functionally involved. The aim of this study was to analyse the level of gene expression of selected MT isoforms during brain aging. By using real-time PCR analysis, we determined the MT1/2 and MT3 expression profiles in cerebral cortex and hippocampus of adolescent (2 months), adult (4 and 8 months), and middle-aged (16 months) rats. We show that the relative abundance of all types of MT transcripts changes during aging in both hippocampus and cortex; the first effect is a generalized decrease in the content of MTs transcripts from 2- to 8-months-old rats. After passing middle age, at 16 months, we observe a huge increase in MT3 transcripts in both cortical and hippocampal areas, while the MT1/2 mRNA content increases slightly, returning to the levels measured in adolescent rats. These findings demonstrate an age-related expression of the *MT3* gene. A possible link between the increasing amount of MT3 in brain aging and its different metal-binding behaviour is discussed.

1. Introduction

Metallothioneins (MTs) are small, intracellular heavy-metal-binding proteins involved in metal detoxification and protection against oxidative stress [1,2]. Ubiquitously present in living organisms [3,4], the mammalian MT family falls into four subgroups: MT1, MT2, MT3, and MT4 [5]. MT1 and MT2 encode through a series of gene duplication events for multiple isoforms present in almost all tissues, while MT3 and MT4 evolved in a single form to accomplish specific roles in brain and epithelium, respectively [6–8]. In the mammalian brain, MT1 and MT2 are preferentially expressed in astrocytes and activated microglia [9]; MT3 is expressed predominantly in neurons and, to a lesser extent, in astrocytes [10].

It has been demonstrated that MT1 and MT2 protect the central nervous system (CNS) in response to experimentally induced injury [11] and following viral infections [12], whereas MT3 neither affects inflammatory responses nor plays an important antioxidant role [11]. Indeed, the MT3 functional role and regulation in CNS is still a matter of debate [10,13]. MT3 is known as a growth inhibitory factor

* Corresponding author.
E-mail address: rosaria.scudiero@unina.it (R. Scudiero).

http://dx.doi.org/10.1016/j.crvi.2016.11.003
1631-0691/

able to inhibit the survival and neurite formation in cultured neurons in vitro [14]. MT3 mRNA and protein are upregulated following brain injury [15] and downregulated in Alzheimer's disease (AD) [14,16].

The known functions of MTs include metalloregulatory roles in cell growth and differentiation [17], so it is not surprising that most mammalian tissues contain age-related basal levels of MTs, with the major amount found in developing cells [18]. Enhanced synthesis of MTs is also observed in rapidly proliferating tissues, stressing their crucial role in normal and neoplastic cell growth [18–20]. However, the MTs' role in aging is controversial: in mammals, MT expression has been found to increase in aged kidney [21], whereas decreased significantly with aging in the skin [22].

Aging is a major risk factor for brain neurodegenerative disorders, including cerebrovascular disease, AD, Parkinson's disease (PD) and cancer [23–26]. Brain aging is accompanied with molecular, functional and genetic changes, leading to increased susceptibility to diseases and cognitive impairments. As it has been proven in the mouse, MTs downregulation results in a progressive neurodegeneration, leading to early aging, morbidity, and mortality [27]; the neurodegenerative alterations are attenuated by MTs overexpression, suggesting the neuroprotective role of MTs in aging [27]. These studies, however, did not include the identification of the MT isoforms functionally involved.

In this study, by using real-time PCR analysis, we examined and compared the expression of *MT1/2* and *MT3* genes during aging in the rat brain. In particular, we evaluated the MT1/2 and MT3 expression profiles in the cerebral cortex and hippocampus of pubertal (2 months), adult (4 and 8 months), and middle-aged (16 months) rats.

Our results demonstrate an age-related expression of the *MT3* gene, thus, suggesting its implication in physiological changes associated with aging.

2. Materials and methods

2.1. Animal and experimental design

Male Wistar rats (Charles River, Calco, Como, Italy) of 2 months of age (adolescent), with the same starting body weight (160 ± 10 g), were individually caged in a temperature-controlled room (23 ± 1 °C) submitted to a 12-h light/12-h dark cycle. Animals were housed in the Animal Care Facility at the Department of Biology, with ad libitum access to water and to a standard diet (Mucedola 4RF21; Settimo Milanese, Milan, Italy) up to 4 (social maturity, group 1), 8 (adulthood, group 2), or 16 (aged, group 3) months. Eight animals of each group were anesthetized with chloral hydrate (40 mg/100 g body wt) and killed by decapitation. Group 4 was comprised 8 adolescent rats sacrificed four days after their arrival in the animal facility. The brains were quickly removed and the cerebral cortex and hippocampus were dissected on ice. Samples of each brain region were snap frozen in liquid nitrogen immediately and stored at −80 °C for subsequent RNA isolation. The livers of the rats belonging to group 4 were also collected, frozen and stored at –80 °C for RNA isolation. The protocols for animal care and use were approved by the Scientific Ethics Committee on Animal Experimentation of the University Federico II of Naples. All experimental animal procedures were carried out in compliance with the national guidelines for the care and use of research animals (D.L.116/92, implementation of EEC directive 609/86). All efforts were made to minimize animal suffering and to reduce the number of animals used.

2.2. RNA purification and cDNA synthesis

Total RNA was extracted according to the TRI-Reagent (Sigma–Aldrich) protocol. The quality of each total RNA was checked by electrophoresis on 2% agarose gel stained with ethidium bromide and by measuring the optical density at 260/280 nm. A ratio of 1.8–2.0 was accepted for further reverse transcription. The QuantiTect Reverse Transcription Kit (Qiagen) was used for the removal of genomic DNA contamination and for the subsequent cDNA synthesis. Approximately 1 μg of total RNA was used, according to the kit's protocol.

2.3. Quantitative real-time PCR analysis

The real-time PCR reactions were carried out in quadruplicate in an Applied Biosystems 7500 Real-Time System by using the Power SYBR Green Master Mix PCR (Applied Biosystems) following procedures recommended by the manufacturer. Each SYBR Green reaction (total volume: 20 μL) contained 12 μL of real-time PCR Master Mix, 1 μL of each of the forward and reverse primers (10 μM), 2 μL of 1:1 diluted cDNA, and 4 μL of nuclease-free water. Nuclease-free water for the replacement of the cDNA template was used as a negative control. For the internal standard control, the expression of *β-actin* gene was quantified. Primer sequences were designed using Primer Express software (Applied Biosystems). A single pair of specific primers for both MT1 and MT2 isoforms was designed on the nucleotide sequences of *Rattus norvegicus* MT1 (NM 138826.4) and MT2 (NM 001137564.1). Specific primers for MT3 were designed on the *R. norvegicus* template NM 053968.3, choosing the most divergent sequence tracts rather than MT1/2 isoforms. β-actin primers were designed on the exon junction 75/76 (forward primer) on *R. norvegicus* template NM031144.2. All the primers used in real-time PCR analysis are listed in Table 1. PCR was performed under the following conditions: holding stage of 95 °C per 10 min; cycling stage (45 cycles): 95 °C × 10 s – 60 °C × 10 s – 72 °C × 10 s; melting stage: 95 °C × 5 s – 65 °C × 1 min – 95 °C × 30 s – 40 °C × 30 s. The melting curve analysis of PCR products was performed in

Table 1
Specific primers used for semiquantitative real-time PCR analyses.

Name	Nucleotide sequence (5′–3′)	Length	Direction
MT1/2_F	ATGGACCCCAACTGCTCCTG	20-mer	Sense
MT1/2_R	CTTTGCAGACACAGCCCTGGG	21-mer	Antisense
MT3_F	CCCCTGTCCTACTGGTGGT	19-mer	Sense
MT3_R	CTGCATTTCTCGGCCTTG	18-mer	Antisense
β-act_F	ACCCGCCACCAGTTCGCCAT	20-mer	Sense
β-act_R	CGGCCCACGATGGAGGGGAA	20-mer	Antisense

order to ensure gene-specific amplification. Changes in the gene expression relative to the different samples were calculated according to the standard $2^{-\Delta\Delta Ct}$ method described by Livak and Schmittgen [28].

2.4. Statistical analysis

Data are presented as mean ± standard error of the mean (SEM) from four separate experiments in each sample. Statistical analyses were carried out by StatView software (Altura Software, Inc.). The differences between the mean values were analysed by one-way analysis of variance (ANOVA) followed by Fisher's LSD test. The differences were considered significant when $P < 0.05$.

3. Results

3.1. Expression of MT isoforms in liver and brains of adolescent rats

As a preliminary step, we firstly decided to compare the relative abundance of MT1/2 and MT3 transcripts in the liver, the cerebral cortex, and the hippocampus of adolescent rats. As expected, MT1 and MT2 are the major forms in the liver, whereas MT3 is the most represented isoform (Fig. 1) in the two areas of the brain, with the level of the cortex higher than that of the hippocampus. However, a significant amount of MT3 transcripts was also detectable in the liver, as well as lower levels of MT1/MT2 isoforms were found both in the cortical and hippocampal areas (Fig. 1).

3.2. Expression of MT isoforms in the aging brain

Once the MTs gene expression profile in adolescent (2-month-old) rats established, we carried out the study evaluating MT1/2 and MT3 mRNAs levels in the hippocampus and the cortex of adult (4- and 8-month-old), and middle-aged (16-month-old) rats. Real-time PCR revealed a huge increase in MT3 expression in both regions of the brain, in aged rats. In particular, the level of this transcript increased by 16 times compared to the 2-month-old rats in the cerebral cortex (Fig. 2a) and by about 14 times in the hippocampus (Fig. 2b). Interestingly, we did not observe a linear increase in MT3 transcripts with the age from 2 to 8 months in both the hippocampus and the cortex; on the contrary, a slight but significant decrease in MT3 transcripts was observed in adult rats when compared with young rats (Fig. 2).

As regarding MT1/2 expression in brain areas, real-time PCR analysis demonstrated that the amount of these transcripts decreased in adults (4- and 8-month-old rats), and increased slightly only in aged rats (16 months),

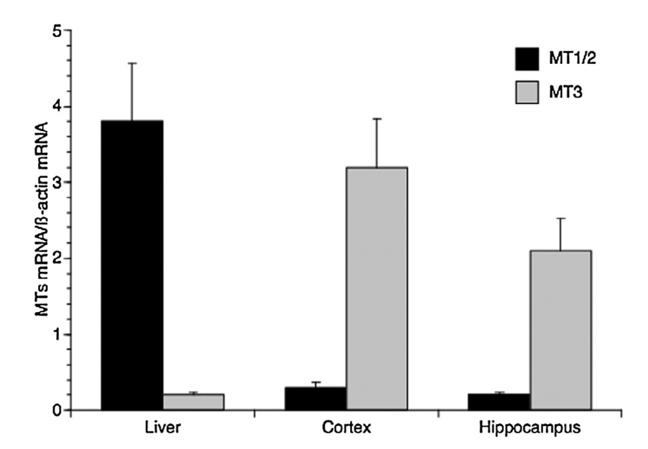
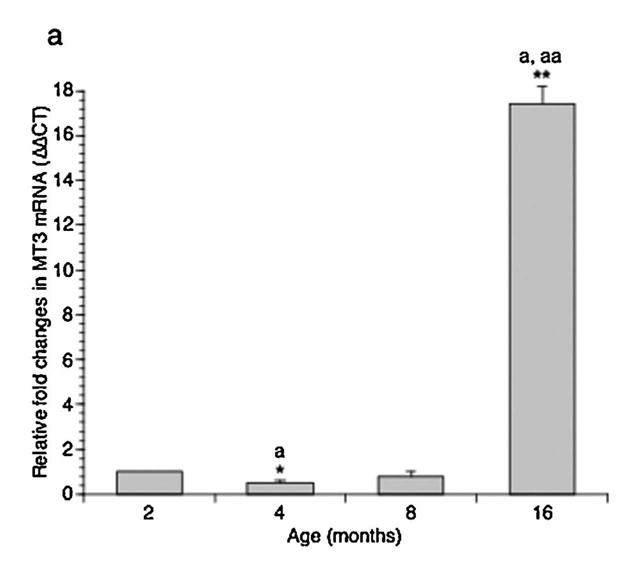


Fig. 1. Real-time PCR analysis of metallothionein isoforms expression in liver, cerebral cortex and hippocampus of 2-month-old rats. MT1/2 and MT3 mRNA levels are shown relative to β-actin mRNA. The data represent the mean ± SEM (eight rats per group).



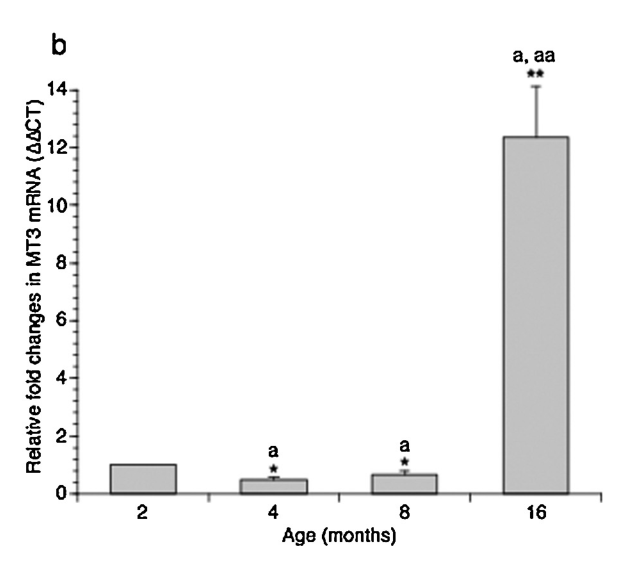


Fig. 2. Effect of aging on *MT3* gene expression in rat cortical (a) and hippocampal (b) areas. The MT3 mRNA expression was normalized to that of β-actin mRNA and converted in fold change, compared with 2-month-old rats. The data represent the mean ± SEM (eight rats per group). Significance of differences is shown. $^{*}P < 0.05$; $^{**}P < 0.001$. [a]Significance vs. 2 months; [aa]Significance vs. 4 and 8 months.

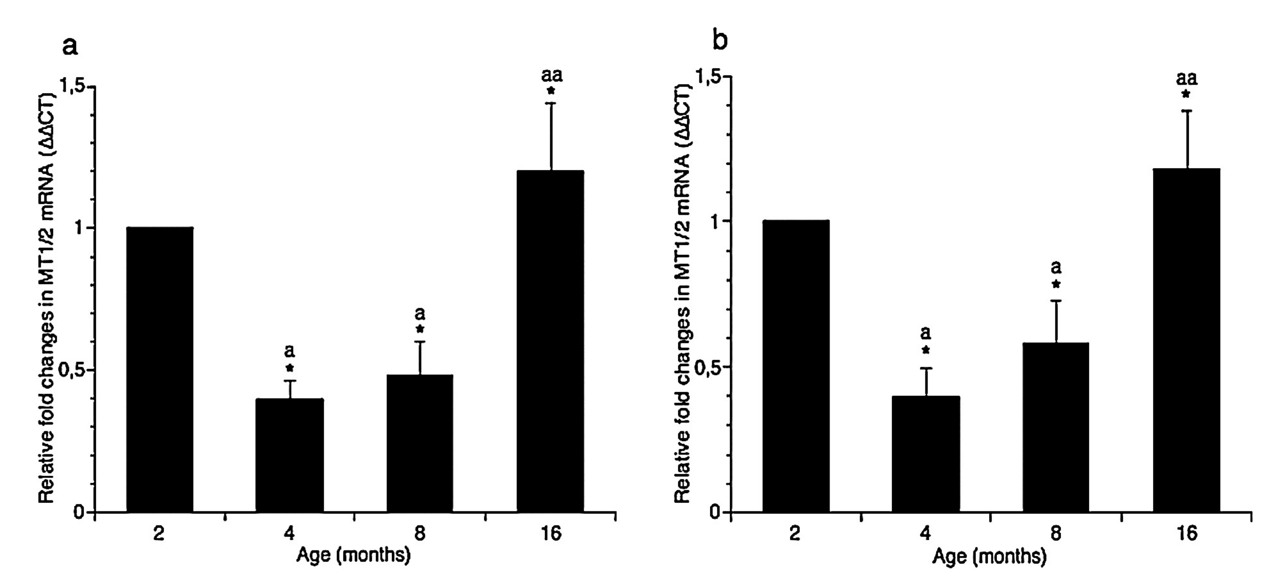


Fig. 3. Effect of aging on *MT1* and *MT2* genes expression in rat cortical (a) and hippocampal (b) areas. The MT1/2 mRNAs expression was normalized to that of β-actin mRNA and converted in fold change, compared with the 2-month-old rats. The data represent the mean ± SEM (eight rats per group). The significance of differences is shown. $^{*}P < 0.05$; ^{a}Significance vs. 2 months; ^{aa}Significance vs. 4 and 8 months.

reaching more or less the level measured in 2-months rats, both in cortical (Fig. 3a) and hippocampal (Fig. 3b) areas.

4. Discussion

Aging is a dominant risk factor for many CNS disorders, among which AD and PD [23,24,26,29]. Aging contributes to the physiological decline of cells and tissues; in the brain, it is associated with inflammation, increased oxidative damage, protein aggregate accumulation and demyelination, whereas it gives rise to a modest neuron and synapse loss [30,31]. Age-related changes in CNS gene expression levels have been reported and many genes, and relative proteins, have been suggested as prognostic biomarkers of neurodegenerative disorders [32–34]. Recently, MT genes have been introduced in the list of early biomarkers of neuronal disorders [27,29]. It has been demonstrated that MTs overexpression in mouse brain provide neuroprotection against deleterious consequences of oxidative and nitrosative stress. However, the authors did not identify the MT isoform(s) responsive to neurodegeneration [27]. Therefore, a major aim of this study was to show whether changes in MT isoforms ratio occur with aging in rats' hippocampus and cerebral cortex.

MT3 is reported as the most abundant isoform expressed in the brain, and our data are consistent with this result. Here, we also show that the relative abundance of all types of MT transcripts change during aging in both hippocampus and cortex; surprisingly, the first effect is a generalized decrease in the content of MTs transcripts from 2-month-old to 8-month-old rats. This pattern can be explained according to two hypotheses. In the first one, it is possible to assume that the rate of MT expression measured in adolescent rats is strictly linked to the physiological state of the brain, consisting of active, proliferating cells with a high metabolic rate. On the other hand, it cannot be excluded that the higher content of MTs detected in adolescent rats compared with adults is due to the stress that these animals undergo in their early stages of life. Indeed, once in the animal facility, the rats are maintained in individual cages under optimum conditions of humidity, temperature, photoperiod, with water ad libitum and right amount of food; these conditions would lead to a decrease in MTs expression, lacking the stressful factors that may cause their temporary increase.

After passing middle age, at 16 months, we observe a huge increase in MT3 transcripts in both cortical and hippocampal areas, while the MT1/2 mRNA content increases slightly, returning to the levels measured in young rats (2 months). These findings demonstrate an age-related expression of the *MT3* gene, whereas the lower levels of *MT1/2* genes might suggest a marginal role of these players, if any, in the aging process of the brain. Structural and functional studies on MT3 demonstrated the stronger Cu-thionein character of MT3 compared to that of MT1 and MT2 [35,36], corroborating the hypothesized role of this MT isoform in the brain as a key element in the homeostasis and metabolism of copper ions in the CNS [36]. Recently, Fu et al. have ascertained an age-dependent increase in the Cu levels in rat brains [37].

Therefore, it is conceivable that the increasing amount of MT3 expression in the aging brain might be linked to its different metal-binding behaviour with respect to the other MT isoforms and to its specific neuronal growth inhibitory bioactivity. Together, these features could better meet the needs of aged brain cells.

Disclosure of interest

The authors declare that they have no competing interest.

References

[1] S. Takahashi, Positive and negative regulators of the metallothionein gene (review), Mol. Med. Rep. 12 (2015) 795–799.
[2] X.B. Ling, H.W. Wei, J. Wang, Y.Q. Kong, Y.Y. Wu, J.L. Guo, T.F. Li, J.K. Li, Mammalian metallothionein-2A and oxidative stress, Int. J. Mol. Sci. 17 (2016) 1483.
[3] D.H. Hamer, Metallothionein, Annu. Rev. Biochem. 55 (1986) 913–951.
[4] G. Isani, E. Carpenè, Metallothioneins, unconventional proteins from unconventional animals: a long journey from nematodes to mammals, Biomolecules 4 (2014) 435–457.
[5] A.T. Miles, G.M. Hawksworth, J.H. Beattie, V. Rodilla, Induction, regulation, degradation, and biological significance of mammalian metallothioneins, Crit. Rev. Biochem. Mol. Biol. 35 (2000) 35–70.
[6] A. Moleirinho, J. Carneiro, R. Matthiesen, R.M. Silva, A. Amorim, L. Azevedo, Gains, losses and changes of function after gene duplication: study of the metallothionein family, PLoS One 6 (2011) e18487.
[7] R.D. Palmiter, S.D. Findley, T.E. Whitmore, D.M. Durnam, MT-III, a brain-specific member of the metallothionein gene family, Proc. Natl. Acad. Sci. U S A 89 (1992) 6333–6337.
[8] C.J. Quaife, S.D. Findley, J.C. Erickson, G.J. Froelick, E.J. Kelly, B.P. Zambrowicz, R.D. Palmiter, Induction of a new metallothionein isoform (MT-IV) occurs during differentiation of stratified squamous epithelia, Biochemistry 33 (1994) 7250–7259.
[9] M.Ø. Pedersen, R. Jensen, D.S. Pedersen, A.D. Skjolding, C. Hempel, L. Maretty, M. Penkowa, Metallothionein-I + II in neuroprotection, Biofactors 35 (2009) 315–325.
[10] S.J. Lee, J.Y. Koh, Roles of zinc and metallothionein-3 in oxidative stress-induced lysosomal dysfunction, cell death, and autophagy in neurons and astrocytes, Mol. Brain 3 (2010) 30.
[11] M. Giralt, M. Penkowa, N. Lago, A. Molinero, J. Hidalgo, Metallothionein-1 + 2 protect the CNS after a focal brain injury, Exp. Neurol. 173 (2002) 114–128.
[12] B.L. Williams, K. Yaddanapudi, C.M. Kirk, A. Soman, M. Hornig, W.I. Lipkin, Metallothioneins and zinc dysregulation contribute to neurodevelopmental damage in a model of perinatal viral infection, Brain Pathol. 16 (2006) 1–14.
[13] A.K. West, J. Hidalgo, D. Eddins, E.D. Levin, M. Aschner, Metallothionein in the central nervous system: roles in protection, regeneration and cognition, Neurotoxicology 29 (2008) 488–502.
[14] Y. Uchida, K. Takio, K. Titani, Y. Ihara, M. Tomonaga, The growth inhibitory factor that is deficient in the Alzheimer's disease brain is a 68 amino acid metallothionein-like protein, Neuron 7 (1991) 337–347.
[15] I. Hozumi, T. Inuzuka, S. Tsuji, Brain injury and growth inhibitory factor (GIF) – a mini review, Neurochem. Res. 23 (1998) 319–328.
[16] V. Colangelo, J. Schurr, M.J. Ball, R.P. Pelaez, N.G. Bazan, W.J. Lukiw, Gene expression profiling of 12633 genes in Alzheimer hippocampal CA1: transcription and neurotrophic factor down-regulation and up-regulation of apoptotic and pro-inflammatory signaling, J. Neurosci. Res. 70 (2002) 462–473.
[17] M.G. Cherian, M.D. Apostolova, Nuclear localization of metallothionein during cell proliferation and differentiation, Cell Mol. Biol. (Noisy-le-Grand) 46 (2000) 347–356.
[18] N. Thirumoorthy, K.T. Manisenthil Kumar, A. Shyam Sundar, L. Panayappan, M. Chatterjee, Metallothionein: an overview, World J. Gastroenterol. 13 (2007) 993–996.
[19] D. Lim, K.M. Jocelyn, G.W. Yip, B.H. Bay, Silencing the metallothionein-2A gene inhibits cell cycle progression from G1- to S-phase involving ATM and cdc25A signaling in breast cancer cells, Cancer Lett. 276 (2009) 109–117.
[20] R. Mehrian-Shai, M. Yalon, A.J. Simon, E. Eyal, T. Pismenyuk, I. Moshe, S. Constantini, A. Toren, High metallothionein predicts poor survival in glioblastoma multiform, BMC Med. Genomics 8 (2015) 68.
[21] J. Leierer, M. Rudnicki, S.J. Braniff, P. Perco, C. Koppelstaetter, I. Mühlberger, S. Eder, J. Kerschbaum, C. Schwarzer, A. Schroll, G. Weiss, S. Schneeberger, S. Wagner, A. Königsrainer, G.A. Böhmig, G. Mayer, Metallothioneins and renal ageing, Nephrol. Dial. Transplant. 31 (2016) 1444–1452.
[22] C. Ma, L.F. Li, X. Chen, Expression of metallothionein-I and II in skin ageing and its association with skin proliferation, Br. J. Dermatol. 164 (2011) 479–482.
[23] T. Niccoli, L. Partridge, Ageing as a risk factor for disease, Curr. Biol. 22 (2012) R741–R752.
[24] R.A. Harris, L. Tindale, R.C. Cumming, Age-dependent metabolic dysregulation in cancer and Alzheimer's disease, Biogerontology 15 (2014) 559–577.
[25] D.K. Smith, M. He, C.L. Zhang, J.C. Zheng, The therapeutic potential of cell identity reprogramming for the treatment of aging-related neurodegenerative disorders, Prog. Neurobiol. (2016) 30067–30068 (S0301-0082).
[26] C. Rodríguez-Nogales, E. Garbayo, M.M. Carmona-Abellán, M.R. Luquin, M.J. Blanco-Prieto, Brain aging and Parkinson's disease: new therapeutic approaches using drug delivery systems, Maturitas 84 (2016) 25–31.
[27] S. Sharma, M. Ebadi, Significance of metallothioneins in aging brain, Neurochem. Int. 65 (2014) 40–48.
[28] K.J. Livak, T.D. Schmittgen, Analysis of relative gene expression data using real-time quantitative PCR and the 2(-Delta Delta C(T)), Methods 25 (2001) 402–408.
[29] S. Sharma, C.S. Moon, A. Khogali, A. Haidous, A. Chabenne, C. Ojo, M. Jelebinkov, Y. Kurdi, M. Ebadi, Biomarkers in Parkinson's disease (recent update), Neurochem. Int. 63 (2013) 201–229.
[30] G. Bartzokis, T.A. Tishler, P.H. Lu, P. Villablanca, L.L. Altshuler, M. Carter, D. Huang, N. Edwards, J. Mintz, Brain ferritin iron may influence age- and gender-related risks of neurodegeneration, Neurobiol. Aging 28 (2007) 414–423.
[31] P.H. Lu, G.J. Lee, E.P. Raven, K. Tingus, T. Khoo, P.M. Thompson, G. Bartzokis, Age-related slowing in cognitive processing speed is associated with myelin integrity in a very healthy elderly sample, J. Clin. Exp. Neuropsychol. 33 (2011) 1059–1068.
[32] S.D. Ginsberg, Expression profile analysis of brain aging, in: D.R. Riddle (Ed.), SourceBrain Aging: Models, Methods, and Mechanisms, CRC Press/Taylor & Francis,, Boca Raton, FL, USA, 2007 (chapter 7).
[33] M.S. Spagnuolo, B. Maresca, M.P. Mollica, G. Cavaliere, C. Cefaliello, G. Trinchese, M.G. Esposito, R. Scudiero, M. Crispino, P. Abrescia, L. Cigliano, Haptoglobin increases with age in rat hippocampus and modulates Apolipoprotein E mediated cholesterol trafficking in neuroblastoma cell lines, Front Cell Neurosci. 8 (2014) 212.
[34] A. Elobeid, S. Libard, M. Leino, S.N. Popova, I. Alafuzoff, Altered proteins in the aging brain, J. Neuropathol. Exp. Neurol. 75 (2016) 316–325.
[35] S. Toriumi, T. Saito, T. Hosokawa, Y. Takahashi, T. Numata, M. Kurasaki, Metal binding ability of metallothionein-3 expressed in *Escherichia coli*, Basic Clin. Pharmacol. Toxicol. 96 (2005) 295–301.
[36] E. Artells, O. Palacios, M. Capdevila, S. Atrian, In vivo-folded metal-metallothionein 3 complexes reveal the Cu-thionein rather than Zn-thionein character of this brain-specific mammalian metallothionein, FEBS J. 281 (2014) 1659–1678.
[37] S. Fu, W. Jiang, W. Zheng, Age-dependent increase of brain copper levels and expressions of copper regulatory proteins in the subventricular zone and choroid plexus, Front Mol. Neurosci. 8 (2015) 22.

C. R. Biologies 340 (2017) 18–24

Contents lists available at ScienceDirect

Comptes Rendus Biologies

www.sciencedirect.com



Cell biology / Biologie cellulaire

Overexpression of HIF-1α in mesenchymal stem cells contributes to repairing hypoxic-ischemic brain damage in rats



Deju Lin [a], Liping Zhou [a], Biao Wang [a], Lizhen Liu [b], Li Cong [c], Chuanqin Hu [a], Tingting Ge [a], Qin Yu [a,*]

[a] College of Life Science, Zhejiang Chinese Medical University, Hangzhou, Zhejiang, China
[b] Bone Marrow Transplantation Center, The First Affiliate Hospital, Zhejiang University School of Medicine, Hangzhou, Zhejiang, China
[c] The First Clinical Medical College, Zhejiang Chinese Medical University, Hangzhou, Zhejiang, China

ARTICLE INFO

Article history:
Received 12 May 2016
Accepted after revision 6 November 2016
Available online 7 December 2016

Keywords:
Hypoxic-ischemic brain damage
Mesenchymal stem cell
Hypoxia inducible factor-1 alpha

ABSTRACT

Preclinical researches on mesenchymal stem cells (MSCs) transplantation, which is used to treat hypoxic-ischemic (HI) brain damage, have received inspiring achievements. However, the insufficient migration of active cells to damaged tissues has limited their potential therapeutic effects. There are some evidences that hypoxia inducible factor-1 alpha (HIF-1α) promotes the viability and migration of the cells. Here, we aim to investigate whether overexpression of HIF-1α in MSCs could improve the viability and migration capacity of cells, and its therapeutic efficiency on HI brain damage. In the study, MSCs with HIF-1α overexpression was achieved by recombinant lentiviral vector and transplanted to the rats subsequent to HI. Our data indicated that overexpression of HIF-1α promoted the viability and migration of MSCs, HIF-1α overexpressed MSCs also had a stronger therapeutic efficiency on HI brain damaged treatment by mitigating the injury on behavioral and histological changes evoked by HI insults, accompanied with more MSCs migrating to cerebral damaged area. This study demonstrated that HIF-1α overexpression could increase the MSCs' therapeutic efficiency in HI and the promotion of the cells' directional migration to cerebral HI area by overexpression may be responsible for it, which showed that transplantation of MSCs with HIF-1α overexpression is an attractive therapeutic option to treat HI-induced brain injury in the future.

1. Introduction

Hypoxic-ischemic (HI) brain damage is a clinical syndrome with high mortality and morbidity [1], and the survivors have suffered widely mental and physical disabilities [2]. However, there are no effective treatments available for HI brain damage at present.

Mesenchymal stem cells (MSCs), which are easily obtained from many tissues, have aroused great interest in regenerative medicine because of their multi-directional differentiation potential and hypo-immunogenicity properties [3]. In recent years, MSCs have showed a significant neuroprotective effects in experimental models of HI brain damage [4–6]. However, the main problem is that the low number of active cells reaching the target tissues after

* Corresponding author at: 548, Binwen Road, 310053 Hangzhou, Zhejiang, China.
E-mail address: qinyu3587@126.com (Q. Yu).

http://dx.doi.org/10.1016/j.crvi.2016.11.001
1631-0691/

transplantation blocks its potential therapeutic effects [7,8].

Previous studies suggested that delivering the desired genes into the cells may overcome some limitations of cells and facilitate therapeutic efficiency after cell transplantation [9,10]. Hypoxia inducible factor-1 alpha (HIF-1α) is one of the most important regulators in response to oxygen levels, and the stabilization of HIF-1α in cells may promote activation and migration [11–13].

In the present study, we intended to overexpress HIF-1α in MSCs by recombinant lentivirus and investigate the issue whether HIF-1α overexpression could promote the therapeutic efficiency of MSCs.

2. Materials and methods

2.1. Animals

All procedures related to the use of animals complied with the guide published by NIH [14]. Adult male Sprague-Dawley rats (80–100 g) were purchased from the Animal Center of Zhejiang Chinese Medical University, Hangzhou, China (Laboratory Animal Certificate: scxk 2008-0016).

2.2. Generation, culture and pretreatment of MSCs

MSCs were obtained from rat femoral and tibia bone marrow as previously described [15]. Briefly, muscles, connective tissue and epiphyses were removed from femur and tibia. Marrow was harvested by 1.0 mL syringe with cell medium that consist of Dulbecco's modified Eagle's medium/Ham's F-12 (DMEM/F-12; Invitrogen, Grand Island, NY, USA), 10% fetal bovine serum (FBS; Life Technologies, Carlsbad, CA, USA) and 1% penicillin-streptomycin (HyClone Laboratories, Inc., South Logan, Utah, USA). Cells were then centrifuged for 10 min at 1000 rpm, re-suspended in the cell medium and cultured at 37 °C, 5% CO_2. After 24 h, all non-adherent cells were removed by medium exchange; the fresh medium was subsequently replaced every 2 days. The adherent cells were trypsinized at 80% confluence, and passaged at 1:2. MSCs from passage 3 were used in the subsequent experiments.

MSCs had received a hypoxia pretreatment during 24 h to mimic the microenvironment in the damaged area in order to activate the endogenous gene expression, which is the natural effect of cells in response to hypoxia. Briefly, the cells were placed in a hypoxia incubator and balanced with a gas mixture (1% O_2, 5% CO_2, 94% N_2) for 10 min at a flow rate of 1 L/min. Then, the hypoxia incubator was sealed to maintain a hypoxic environment before being put into a cell incubator under 5% CO_2 at 37 °C.

2.3. Lentivirus-mediated gene transfer and experimental groups of cells

MSCs with HIF-1α overexpression were constructed by a lentivirus system following the manufacturer's instructions (Invitrogen, Carlsbad, CA, USA). The cells were infected with a lentivirus encoding either GFP alone or both GFP and HIF-1α. Then the MSCs were assigned into three experiment groups: HIF-1α-MSCs (transfection with HIF-1α and GFP), GFP-MSCs (transfection with GFP), NM-MSCs (undisturbed normal MSCs).

The transfection efficiency of the cells was detected by fluorescence microscopy analysis after transfecting for 48 h. The protein expression level of HIF-1α in MSCs was detected by Western blotting.

2.4. Western blotting

The expression level of HIF-1α was evaluated by western blotting after hypoxia pretreatment. Equal amounts of protein from MSCs were separated by 10% SDS-PAGE and transferred to polyvinylidene difluoride membranes (Millipore, Boston, MA). After being blocked with 5% nonfat dry milk for 2 h, the membranes were incubated with rabbit polyclonal antibodies against either HIF-1α (1:1000 dilution, Abcam Technology, Cambridge, MA, USA) or GAPDH (1:2000 dilution, Abcam Technology, Cambridge, MA, USA) overnight at 4 °C. The membranes were then incubated with a second antibody (anti-rabbit IgG HRP, 1:3000; Abcam Technology, Cambridge, MA, USA) and ECL detection systems (Thermo Fisher Scientific, Waltham, MA, USA) were used for detection, GAPDH was used as a loading control.

2.5. MTT assay

An assay with 3-(4,5-dimethylthiazol-2-yl)-2,5-diphenyltetrazolium bromide (MTT) was performed to determine the influence of HIF-1α overexpression on MSC viability. Briefly, pretreated MSCs were seeded in 96-well plates at a density of 2000 cells per well, and cultured for 48 h, and NM-MSCs were used as a control. 10 μL (5 g/L in PBS) of MTT (Sigma Chemical Co., St. Louis, MO, USA) were added to each well and incubated at 37 °C for 4 h. The supernatants were carefully discarded and 150 μL of dimethyl sulfoxide (Sigma Chemical Co., St. Louis, MO, USA) was added. Absorbance was measured at 490 nm by microplate reader (Bio-RAD Model 680, Cal, USA).

2.6. CM-DiI labelling

In order to make it easily observable, MSCs were stained with chloromethylbenzamido dialkylcarbocyanine (CM-DiI, Molecular Probes, USA) at the dose of 1 μg CM-DiI per million cells, and washed twice after incubation at 37 °C for 20 min. Labeled MSCs were used in the following experiments.

2.7. Migration assay

A cell migration assay was performed in Transwell chambers (pore size: 8 μm, polycarbonate membrane; Corning Incorporated, NY, USA) to evaluate the migratory capacity of MSCs. Transwell chambers were put into six well plates. CM-DiI labeled cells were harvested in a serum-free medium; the density was adjusted to 2×10^5 cells/ml. 200 μL of cell suspension were plated in the upper chamber and 500 μL of a fresh medium

containing 10% FBS were added to the lower chamber. After incubation at 37 °C under 5% CO_2 for 24 h, the cells on upper membrane layer were gently wiped away using a cotton swab and the cells migrating to the lower membrane were fixed with 4% paraformaldehyde. The number of cells in the lower side of the membranes was counted microscopically.

2.8. Hypoxic-ischemic model and experimental groups of rats

As HI model was established as in the previous method of Rice et al. [16]. The rats were anesthetized with a 10% chloral hydrate solution (0.3 mL/100 g), and the left carotid artery was isolated and ligated doubly. After 2–3 h, the waking rats were put into a transparent container which was ventilated with a constant flow of mixed gas containing 8% oxygen and 92% nitrogen for 2 h.

The animals were randomly assigned into four experimental groups after HI treatment: sham group, HI-vehicle group, HI-GFP-MSC group, HI-HIF-1α-MSC group. For the rats in the sham group, the carotid artery was isolated but not ligated, and no hypoxia exposure was performed. The rats in the HI-GFP-MSC group and the HI-HIF-1α-MSC group had received 5×10^5 MSCs re-suspended in 0.5 mL of a physiological saline solution by intravenous injection in the tail 24 h after HI treatment, and the other rats received the same volume of physiological saline solution.

2.9. Morris water maze test

Rats ($n = 6$ per group) have been submitted to the Morris water maze test [17] on day 14 after HI to evaluate their spatial learning and memory abilities. The maze consisted of a black circular tank (160 cm diameter × 50 cm height) filled with water (temperature: 22–24 °C). An automatic tracking system (San Diego Instruments, San Diego, CA, USA) was used to record the swimming path and time. Each rat was tested for five training days and one test day. In the task, the rat was put in every quadrant of the pool sequentially, and swam for 60 s to locate the submerged platform; if it failed, the experimenter would guide it to the platform. Then the rat was allowed to remain on the platform for 10 s. On the last day, the platform was removed before the test, and the swimming time in the former platform quadrant was recorded.

2.10. Tissue preparation and histological examination

Rats brains were obtained on days 7, 14 and 21 after HI (each time point $n = 6$ per group), and each hippocampus was embedded in paraffin. The paraffin sections (4 μm thick) were prepared for detection of the migration of MSCs and histological examination in the hippocampus. To measure the migrated cells' number, the sections were observed with a fluorescence microscope to count the CM-DiI positive cells. The histological examination was determined by hematoxylin and eosin (HE) staining.

2.11. Statistical analysis

The data obtained were presented as mean ± standard deviation (SD). Differences between groups were evaluate by analysis of variance for multiple comparisons using SPSS 19.0. A value of $P < 0.05$ was considered to be statistically significant.

3. Results

3.1. Overexpression of HIF-1α in MSCs

After transfection for two days, GFP expression observed under the fluorescence microscope reached up to 90% of the cultured MSCs (Fig. 1A). In the meantime, western blotting was performed to investigate the expression of HIF-1α in MSCs after hypoxia pretreatment. In the present study, the expression of HIF-1α in HIF-1α-MSCs was approximately two times that in NM-MSCs and GFP-MSCs, while the expression level in GFP-MSCs was in accordance with NM-MSCs (Fig. 1B and C). The results indicated that HIF-1α overexpressed MSCs were successfully constructed by a recombinant lentivirus system.

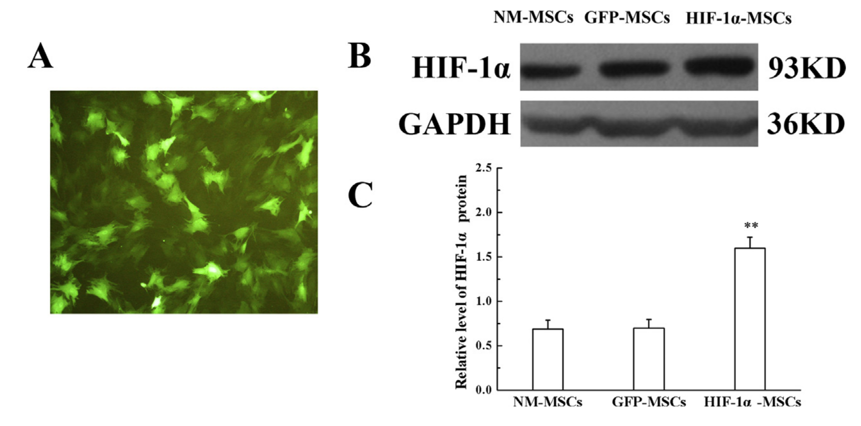


Fig. 1. Transfection efficiency of MSCs. A. The level of GFP expressed in MSCs was observed by fluorescence microscopy (magnification × 100). B. Protein level of HIF-1α in different groups; GAPDH was used as an inner control. C. Quantification of HIF-1α protein expression showed in B. **$P < 0.01$ versus the GFP-MSCs group.

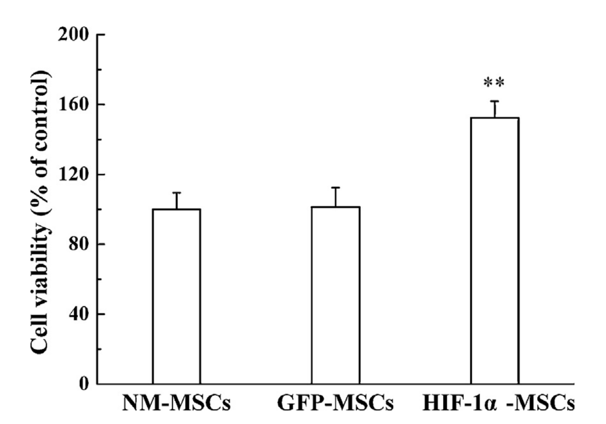


Fig. 2. MTT assay used to quantify the MSCs viability in different group. $^{**}P < 0.01$ versus the GFP-MSCs group.

3.2. HIF-1α overexpression improved the viability of MSCs

MSC viability was assessed by an MTT assay to determine the effect of HIF-1α overexpression. As shown by our results, HIF-1α overexpression immensely improved the viability of MSCs, while there was no significant difference between NM-MSC and GFP-MSC groups (Fig. 2A). The result implied that MSCs with overexpression of HIF-1α had better viability.

3.3. HIF-1α overexpression enhanced migration of MSCs both in vitro and in vivo

The migration of MSCs was analyzed both in in vitro and in vivo experiments. To observe the migration of MSCs directly, the cells were labeled with CM-DiI, a fluorescence marker. The results showed that more than 95% of MSCs were CM-DiI positive after having been labeled (Fig. 3A).

According to the Transwell assay, the number of cells migrating to the lower compartment in HIF-1α-MSC group was more than that in NM-MSC and GFP-MSC groups after hypoxia pretreatment, while no significant difference was found between NM-MSC and GFP-MSC groups after culturing for 24 h (Fig. 3B).

One day after HI, rats received an intravenous transplantation of MSCs, and the presence of migrated MSCs in the hippocampus after transplantation was investigated by observing CM-DiI positive cells. CM-DiI positive cells were clearly observed in the hippocampus on day 7 after HI. And from day 7 to day 21 subsequent to HI, the number of CM-DiI positive cells in the hippocampus increased gradually in a time-dependent manner. A remarkable increase in the recruitment of HIF-1α transduced MSCs was observed in the hippocampus at every time point compared with GFP transduced MSCs (Fig. 3C). Statistical analysis showed that HIF-1α overexpression improved the migration capacity of MSCs toward the sites of injury.

The quantitation of migrated cells demonstrated significant increases in MSCs motility in HIF-1α overexpressed MSCs both in in vitro and in vivo experiments in comparison to GFP infected cells.

3.4. HIF-1α overexpression strengthen the therapeutic efficiency of MSCs on HI rats

In order to investigate the therapeutic effect of HIF-1α transduced MSCs, the Morris water maze test and HE

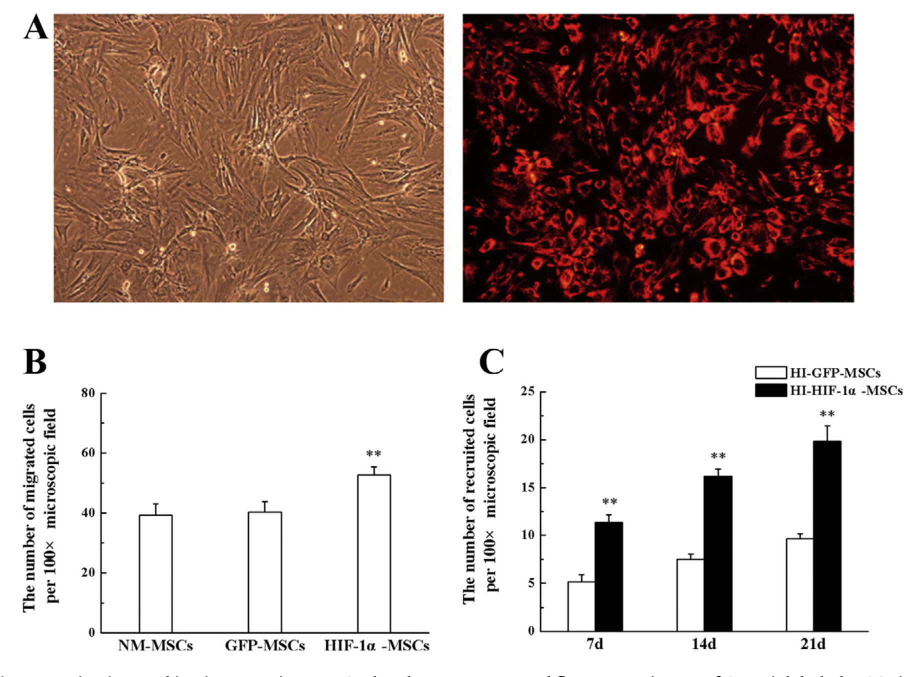


Fig. 3. MSCs migration assay in vitro and in vivo experiments. A. The phase-contrast and fluorescent image of CM-DiI labeled MSCs (magnification: × 100). B. Transwell migration assay, performed in vitro experiments. C. Transplanted MSCs homing to the hippocampus were counted at different time points. $^{**}P < 0.01$ versus the GFP-MSCs group.

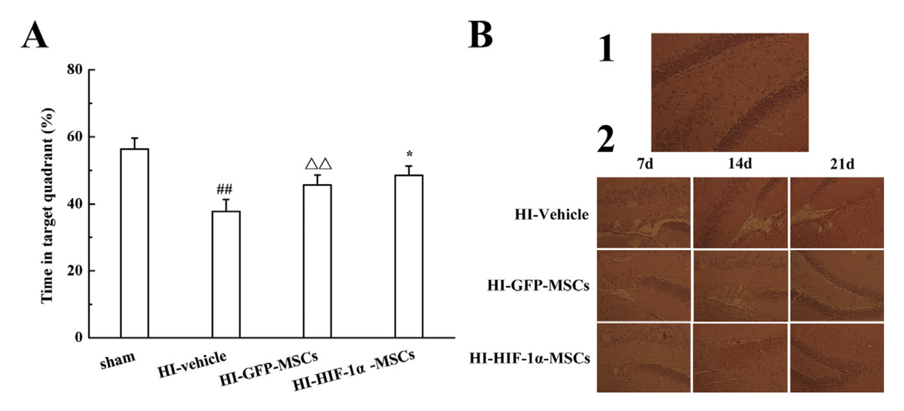


Fig. 4. The therapeutic efficiency of HIF-1α overexpressed MSCs in HI rats. A. Percentage of swimming time in the target quadrant in the Morris water maze. B. HE staining in different groups of the hippocampus. Representative images in the sham group (1), the pathological changes in the HI-Vehicle, HI-GFP-MSCs and HI-HIF-1α-MSCs groups at different time points (2). $^{\#\#}P < 0.01$ versus the sham group, $^{\Delta\Delta}P < 0.01$ versus the HI-Vehicle group, $^{*}P < 0.05$ versus the HI-GFP-MSCs group.

staining in the hippocampus were performed on HI rats. On day 14 after HI, the spatial performance of four groups was evaluated by the Morris water maze test. In the spatial probe test, spatial learning ability was significantly affected by HI, as HI-treated rats spent less time in the target quadrant compared to the sham group. The results suggested that the rats suffered from cognitive dysfunction due to HI treatment. There was a significant increase of time in the target quadrant in both MSC-transplanted groups compared with HI-vehicle group, but a more increase in the amount of time have been found in HI-HIF-1α-MSC group (Fig. 4A). These results indicated that the HI-induced rats achieved partial remission on memorial and cognitive functions after MSCs transplantation, while HIF-1α overexpression could promote this effect.

Some visualized pathological changes were found in HE staining. The data supported that the morphological structures of the hippocampus in the sham group were normal, with uniform dyeing (Fig. 4B1). In contrast with the sham group, the pathological changes in the hippocampus in the HI-vehicle group revealed serious injury, the cells were disordered, and cavitation was visible, suggesting that the HI model had been successfully established. Meanwhile, the rats in HI-GFP-MSC and HI-HIF-1α-MSC groups showed similar but slight pathological changes at every time point after having been subjected to HI, and the changes in the MSCs with HIF-1α transfection group were less marked than those of the GFP control group (Fig. 4B2). The results illustrated that the transplantation of MSCs ameliorated pathological changes after HI, while HIF-1α overexpression could enhance therapeutic efficiency.

4. Discussion

In recent years, abundant researches show that MSCs transplantation has been considered a promising strategy in HI-induced brain-damaged treatment [4,18,19]. However, the insufficient viability as well as the low number of cells transplanted to the target tissues limits the potential therapeutic effects [7,8]. Recent evidences have indicated that HIF-1α is important in cell viability, proliferation and migration following HI injury [12,13]. In the present study, we therefore investigated the therapeutic effect of HIF-1α overexpressed MSCs on HI brain damage. Firstly, overexpression was achieved using a recombinant lentiviral, and a robust overexpression of HIF-1α at the protein level has been seen. Additionally, the functions of HIF-1α overexpression in MSCs showed that HIF-1α overexpression resulted in increased viability and migration of MSCs. Finally, using a HI model, we found that HIF-1α overexpressed MSCs had a stronger therapeutic efficiency on HI brain-damaged treatment by mitigating the injury on behavioral and histological changes evoked by HI insults, accompanied with more MSCs migrating to the damaged cerebral area.

The hypoxia-inducible factor-1 (HIF-1) is recognized as the master regulator of hypoxia response. It is a heterodimeric transcription factor composed of an inducible HIF-1α subunit and a HIF-1β subunit, and HIF-1α is a crucial mediator of the cellular response to hypoxia in contrast to HIF-1β, implying that HIF-1α is a key mediator of the beneficial effect in a low oxygen environment [20]. In this study, just as expected, we have seen the expression of HIF-1α after hypoxia pretreatment, while overexpression increased the expression.

The present study showed that overexpression of HIF-1α enhanced MSCs viability in vitro, which was consistent with a previous study [21]. Intriguingly, the results also showed in our present study that HIF-1α overexpression could further promote the viability of MSCs in vitro in comparison to the effect of HIF-1α induced by hypoxia pretreatment, indicating that the expression level of endogenous HIF-1α, which achieved during hypoxia, does not reach the maximum required for HIF-1α transcription activities, and transfection with exogenous HIF-1α improves the transcription level.

Cerebral ischemia and hypoxia will result in cognitive dysfunction [22,23] as well as pathological changes [24], especially the changes in the hippocampus [25], which showed in the Morris water maze test and HE staining in our study. Transplantation of MSCs after HI contributed to an improved function recovery of neurological deficits

and reduced the degree of pathological changes [18,19,26]. Meanwhile, it was observed that HIF-1α overexpression led to a better efficiency of MSC transplantation. This result is not in keeping with studies by Lopez et al. [27], which showed that overexpression of HIF-1α did not have protective actions upon hypoxia-mediated neuronal death. However, enhanced therapeutic efficiency of cells on brain damage through upregulation of HIF-1α also been found in other groups [28,29]. These controversial results may be explained by the different damage degree (HI vs. mild hypoxia).

We also investigated the recruitment of MSCs in the hippocampus in time course experiments; the present study results together with that from previous study [30] demonstrated a number of MSCs in the hippocampus increasing continuously three weeks after transplantation. Consistently with in vitro experiments, HIF-1α overexpression also improved MSCs migration to the injured area. The upregulation of HIF-1α increased the migration of MSCs, as well as it enhanced the therapeutic efficiency of MSCs, which was also found by other groups [31,32]. Thus, enhancing the number of MSCs to the site of injury may improve the therapeutic efficiency of MSCs transplantation. In other words, the improvement of the therapeutic efficiency through overexpression of the HIF-1α of MSCs could be due to increased cell migration to the damaged area.

The limitation of this study is that the underlying associated mechanisms about HIF-1α promoting the directional migration of MSCs to the cerebral HI area need to be confirmed, which we will investigate in further studies.

In conclusion, this study demonstrated that HIF-1α overexpression could increase the therapeutic efficiency MSCs in HI, which will correlate well with the promotion cells' directional migration to the cerebral HI area. We propose that transplantation of MSCs with HIF-1α overexpression is an attractive therapeutic option to treat HI-induced brain injury in the future.

Acknowledgments

This work was financially supported by National Natural Science Foundation of China (Grant No. 81270566, Grant No. 81500114).

References

[1] F. Triulzi, C. Parazzini, A. Righini, Patterns of damage in the mature neonatal brain, Pediatr. Radiol. 36 (2006) 608–620.
[2] E.M. Graham, K.A. Ruis, A.L. Hartman, F.J. Northington, H.E. Fox, A systematic review of the role of intrapartum hypoxia-ischemia in the causation of neonatal encephalopathy, Am. J. Obstet. Gynecol. 199 (2008) 587–595.
[3] H.D. Zomer, A.S. Vidane, N.N. Goncalves, C.E. Ambrosio, Mesenchymal and induced pluripotent stem cells: general insights and clinical perspectives, Stem Cells Cloning 8 (2015) 125–134.
[4] E. Diez-Tejedor, M. Gutierrez-Fernandez, P. Martinez-Sanchez, B. Rodriguez-Frutos, G. Ruiz-Ares, M.L. Lara, B.F. Gimeno, Reparative therapy for acute ischemic stroke with allogeneic mesenchymal stem cells from adipose tissue: a safety assessment: a phase II randomized, double-blind, placebo-controlled, single-center, pilot clinical trial, J. Stroke Cerebrovasc. Dis. 23 (2014) 2694–2700.
[5] S.J. Kim, G.J. Moon, W.H. Chang, Y.H. Kim, O.Y. Bang, Intravenous transplantation of mesenchymal stem cells preconditioned with early phase stroke serum: current evidence and study protocol for a randomized trial, Trials 14 (2013) 317.
[6] H. Ding, H. Zhang, H. Ding, D. Li, X. Yi, X. Ma, R. Li, M. Huang, X. Ju, Transplantation of placenta-derived mesenchymal stem cells reduces hypoxic-ischemic brain damage in rats by ameliorating the inflammatory response, Cell Mol. Immunol. (2015), http://dx.doi.org/10.1038/cmi.2015.99.
[7] L.H. Shen, Y. Li, J. Chen, A. Zacharek, Q. Gao, A. Kapke, M. Lu, K. Raginski, P. Vanguri, A. Smith, M. Chopp, Therapeutic benefit of bone marrow stromal cells administered 1 month after stroke, J. Cereb. Blood Flow Metab. 27 (2007) 6–13.
[8] Z. Pasha, Y. Wang, R. Sheikh, D. Zhang, T. Zhao, M. Ashraf, Preconditioning enhances cell survival and differentiation of stem cells during transplantation in infarcted myocardium, Cardiovasc. Res. 77 (2008) 134–142.
[9] J. Wang, H. Wang, J. Shi, Y. Ding, Effects of bone marrow MSCs transfected with sRAGE on the intervention of HMGB1 induced immuno-inflammatory reaction, Int. J. Clin. Exp. Pathol. 8 (2015) 12028–12040.
[10] X. Si, X. Liu, J. Li, X. Wu, Transforming growth factor-beta1 promotes homing of bone marrow mesenchymal stem cells in renal ischemia-reperfusion injury, Int. J. Clin. Exp. Pathol. 8 (2015) 12368–12378.
[11] T.I. Nathaniel, J.O. Soyinka, A. Adedeji, A. Imeh-Nathaniel, Molecular and physiological factors of neuroprotection in hypoxia-tolerant models: pharmacological clues for the treatment of stroke, J. Exp. Neurosci. 9 (2015) 1–5.
[12] L.A. Cunningham, K. Candelario, L. Li, Roles for HIF-1alpha in neural stem cell function and the regenerative response to stroke, Behav. Brain Res. 227 (2012) 410–417.
[13] R.J. Ruthenborg, J.J. Ban, A. Wazir, N. Takeda, J.W. Kim, Regulation of wound healing and fibrosis by hypoxia and hypoxia-inducible factor-1, Mol. Cells 37 (2014) 637–643.
[14] R. National Research Council Institute for Laboratory and Animal, Guide for the care and use of laboratory animals, The National Academy of Sciences, Washington, DC, 1996.
[15] D.P. Lennon, A.I. Caplan, Isolation of rat marrow-derived mesenchymal stem cells, Exp. Hematol. 34 (2006) 1606–1607.
[16] J.E. Rice, R.C. Vannucci 3rd., J.B. Brierley, The influence of immaturity on hypoxic-ischemic brain damage in the rat, Ann. Neurol. 9 (1981) 131–141.
[17] R. Morris, Developments of a water-maze procedure for studying spatial learning in the rat, J. Neurosci. Methods 11 (1984) 47–60.
[18] C.T. van Velthoven, Y. van de Looij, A. Kavelaars, J. Zijlstra, F. van Bel, P.S. Huppi, S. Sizonenko, C.J. Heijnen, Mesenchymal stem cells restore cortical rewiring after neonatal ischemia in mice, Ann. Neurol. 71 (2012) 785–796.
[19] C.T. van Velthoven, A. Kavelaars, C.J. Heijnen, Mesenchymal stem cells as a treatment for neonatal ischemic brain damage, Pediatr. Res. 71 (2012) 474–481.
[20] Q. Ke, M. Costa, Hypoxia-inducible factor-1 (HIF-1), Mol. Pharmacol. 70 (2006) 1469–1480.
[21] F.M. Lampert, C. Kutscher, G.B. Stark, G. Finkenzeller, Overexpression of hif-1alpha in mesenchymal stem cells affects cell-autonomous angiogenic and osteogenic parameters, J. Cell Biochem. 117 (2016) 760–768.
[22] D.A. Tata, I. Markostamou, A. Ioannidis, M. Gkioka, C. Simeonidou, G. Anogianakis, E. Spandou, Effects of maternal separation on behavior and brain damage in adult rats exposed to neonatal hypoxia-ischemia, Behav. Brain Res. 280 (2015) 51–61.
[23] C.Z. Fang, Y.J. Yang, Q.H. Wang, Y. Yao, X.Y. Zhang, X.H. He, Intraventricular injection of human dental pulp stem cells improves hypoxic-ischemic brain damage in neonatal rats, PLoS One 8 (2013) e66748.
[24] Q. Yu, L. Zhou, L. Liu, L. Cong, Y. Wang, T. Ge, D. Lin, Stromal cell-derived factor-1 alpha alleviates hypoxic-ischemic brain damage in mice, Biochem. Biophys. Res. Commun. 464 (2015) 447–452.
[25] S.K. Hota, K. Barhwal, S.B. Singh, G. Ilavazhagan, Differential temporal response of hippocampus, cortex and cerebellum to hypobaric hypoxia: a biochemical approach, Neurochem. Int. 51 (2007) 384–390.
[26] R.K. Jellema, T.G. Wolfs, V. Lima Passos, A. Zwanenburg, D.R. Ophelders, E. Kuypers, A.H. Hopman, J. Dudink, H.W. Steinbusch, P. Andriessen, W.T. Germeraad, J. Vanderlocht, B.W. Kramer, Mesenchymal stem cells induce T-cell tolerance and protect the preterm brain after global hypoxia-ischemia, PLoS One 8 (2013) e73031.
[27] B. Lopez-Hernandez, I. Posadas, P. Podlesniy, M.A. Abad, R. Trullas, V. Cena, HIF-1alpha is neuroprotective during the early phases of mild hypoxia in rat cortical neurons, Exp. Neurol. 233 (2012) 543–554.
[28] W. Wu, X. Chen, C. Hu, J. Li, Z. Yu, W. Cai, Transplantation of neural stem cells expressing hypoxia-inducible factor-1alpha (HIF-1alpha) improves behavioral recovery in a rat stroke model, J. Clin. Neurosci. 17 (2010) 92–95.
[29] K. Chu, K.H. Jung, S.J. Kim, S.T. Lee, J. Kim, H.K. Park, E.C. Song, S.U. Kim, M. Kim, S.K. Lee, J.K. Roh, Transplantation of human neural stem cells

protect against ischemia in a preventive mode via hypoxia-inducible factor-1alpha stabilization in the host brain, Brain Res. 1207 (2008) 182–192.
[30] Y.X. Liu, X.M. Guo, J.F. Li, Y. Meng, H.T. Zhang, A.J. Liu, S.C. Li, Y.L. Liu, H. Zhu, J.H. Xue, Y. Zhang, Z.W. Zhang, Restoration of tissue damage, and never activity after hypoxia-ischemia by implantation of peripheral blood mononuclear cells, Brain Res. 1546 (2014) 34–45.
[31] X. Yu, C. Lu, H. Liu, S. Rao, J. Cai, S. Liu, A.J. Kriegel, A.S. Greene, M. Liang, X. Ding, Hypoxic preconditioning with cobalt of bone marrow mesenchymal stem cells improves cell migration and enhances therapy for treatment of ischemic acute kidney injury, PLoS One 8 (2013) e62703.
[32] I. Rosova, M. Dao, B. Capoccia, D. Link, J.A. Nolta, Hypoxic preconditioning results in increased motility and improved therapeutic potential of human mesenchymal stem cells, Stem Cells 26 (2008) 2173–2182.

C. R. Biologies 340 (2017) 25–36

Contents lists available at ScienceDirect

Comptes Rendus Biologies

www.sciencedirect.com



Animal biology and pathology/Biologie et pathologie animales

High carbohydrate diet induces nonalcoholic steato-hepatitis (NASH) in a desert gerbil



Induction d'une stéatose hépatique non alcoolique par une alimentation hyperglucidique chez une gerbille désertique

Nesrine Semiane [a,*], Fabienne Foufelle [b,c,d], Pascal Ferré [b,c,d], Isabelle Hainault [b,c], Souad Ameddah [e], Aicha Mallek [a], Ali Khalkhal [a], Yasmina Dahmani [a]

[a] *LBPO/Nutrition-métabolisme, FSB/USTHB, BP 32, El Alia, 16111 Alger, Algeria*
[b] *INSERM, UMR-S 872, centre de recherches des Cordeliers, 75006 Paris, France*
[c] *Université Paris-6–Pierre-et-Marie-Curie, UMR S 872, 75006 Paris, France*
[d] *Université Paris-Descartes, UMR S 872, 75006 Paris, France*
[e] *Laboratoire de biologie et environnement, université Mentouri, route de Ain El Bey, 25000 Constantine, Algeria*

ARTICLE INFO

Article history:
Received 11 July 2016
Accepted after revision 7 September 2016
Available online 30 September 2016

Keywords:
Gerbillus gerbillus
Insulin resistance
Lipogenesis
E.R. stress
Oxidative stress

ABSTRACT

A high intake of sugars has been linked to diet-induced health problems. The aim of this study was to assess whether the long-term consumption of a high-carbohydrate diet (HCD) would cause the hepatic histopathological and metabolic abnormalities that characterize nonalcoholic steatohepatitis (NASH) in a desert gerbil, *Gerbillus gerbillus*. Compared to natural diet, HCD leads to several metabolic disorders including adiposity, dyslipidemia, insulin resistance, ectopic fat deposition in the liver, which were associated with higher levels of transcripts of genes involved with fat synthesis, endoplasmic reticulum (ER) stress, and fibrosis. In the same way, the experimented animals showed enhanced oxidative stress. Taken together, these results demonstrate that HCD consumption in gerbils induces metabolic disorders and damaged liver, which are key contributors to NASH development. These results suggest that this rodent represents a valuable natural model for human diet-induced metabolic disorders and nonalcoholic fatty liver disease (NAFLD).

Mots clés :
Gerbillus gerbillus
Insulino-résistance
Lipogenèse
Stress R.E.
Stress oxydatif

RÉSUMÉ

Les effets d'un régime riche en hydrates de carbone (RHC) sur l'induction de dysfonctionnements métaboliques et d'altérations histopathologiques au niveau du foie caractérisant la stéatose hépatique non alcoolique (NASH) ont été étudiés chez la gerbille *Gerbillus gerbillus*. Comparativement au régime naturel, l'alimentation hyperglucidique induit des perturbations métaboliques marquées par une adiposité, une dyslipidémie, une insulinorésistance et un dépôt ectopique de graisses dans le foie, associé à l'augmentation des ARNm de gènes impliqués dans la synthèse des lipides, le stress du réticulum

* Corresponding author.
E-mail address: semianenesrine@yahoo.fr (N. Semiane).

http://dx.doi.org/10.1016/j.crvi.2016.09.002
1631-0691/

endoplasmique et la fibrose. Parallèlement, les animaux expérimentaux développent un état de stress oxydatif. Le RHC induit chez *G. gerbillus* des troubles métaboliques et des lésions hépatiques caractéristiques de la NASH. Nos résultats suggèrent que ce rongeur représente un modèle naturel de choix pour l'étude des dysfonctionnements métaboliques et hépatiques induits par une consommation excessive de glucides chez l'humain.

1. Introduction

Nonalcoholic fatty liver disease (NAFLD) is the main cause of hepatic dysfunction in developed countries and is closely related to components of metabolic syndrome such as obesity, dyslipidemia and type-2 diabetes [1]. Excessive accumulation of triglyceride (TG) in hepatocytes is the hallmark of NAFLD. The spectrum of NAFLD ranges from hepatic steatosis or fatty liver to nonalcoholic steatohepatitis (NASH), liver fibrosis, liver cirrhosis, and eventually hepatocellular carcinoma (HCC) [2]. The precise mechanisms of NAFLD remain poorly understood. The "multiple-hit hypothesis" is currently the most recognized theory to explain disease development and progression, the dysregulation in lipid metabolism being involved in the first hit [3]. It was estimated that 30 % of the TG content in NAFLD livers came from *de novo* lipogenesis, underlying the importance of this pathway in the etiology of NAFLD [4,5]. De novo lipogenesis (DNL) can be triggered by multiple mechanisms, including increased expression of lipogenic enzymes by several specific transcription factors; this is particularly true for members of the SREBP family. One of them, SREBP-1c, controls hepatic DNL primarily by regulation of expression of genes involved in DNL, lipid homeostasis and glucose metabolism [5,6]. Accordingly, hepatic expression of SREBP-1c and its target genes are increased in human fatty liver, compared to healthy individuals [7,8], although DNL is an important determinant of steatosis [9]. The second of the two hits could be due to (1) oxidative stress, (2) proinflammatory cytokines, (3) mitochondrial dysfunction, or/and (4) endoplasmic reticulum stress. Recently, accumulating data have implicated the disruption of endoplasmic reticulum (ER) homeostasis, or ER stress, in both the development of steatosis and progression to NASH [10,11]. ER stress may lead to the activation of various intracellular stress pathways that can initiate or exacerbate insulin resistance (IR) and inflammation and, in some cases, culminate in hepatocyte cell death and liver damage, all of which are important in the pathogenesis of NAFLD. In spite of growing knowledge, several aspects of NAFLD pathogenesis are still unknown.

Considering the difficulty in developing human studies to evaluate the influence of nutrition in the development of NAFLD and associated metabolic abnormalities, animal models constitute a reliable alternative way. Different animal models of NAFLD/NASH have been developed, but few of them replicate the entire human phenotype [12,13]. These models may be classified into three basic categories: those caused by either spontaneous or induced genetic mutation; those produced by either dietary or pharmacological manipulation; and those involving genetic mutation and dietary or chemical challenges. The dietary manipulations used in these last two types of models usually do not resemble the human dietary pattern.

The aim of this study was to determine the long-term impact of high-carbohydrate diet on liver morphology and function in a desert rodent (*Gerbillus gerbillus*). We therefore evaluated the markers involved in metabolic functions, i.e. lipogenesis, fibrosis, ER stress, histopathological changes, and oxidative stress. In the present study, we developed a model of obesity and obesity-related NAFLD in a desert rodent (*G. gerbillus*) using a simple carbohydrate-rich diet.

2. Materials and methods

2.1. Animals and diets

G. gerbillus individuals were collected from the semi-desert Algerian region of Beni-Abbes (30°7' latitude north and 2°10' longitude west). The authorization to capture the animals in desert region was given by the Ministry of Higher Education (Algeria). *G. gerbillus* specimens were maintained under controlled temperature (22 ± 1 °C), humidity (50%) with a fixed 12-h light/dark cycle. After two weeks of acclimatation, the adult gerbils of both sexes were randomly divided into two groups. The control group (n = 6) received a natural diet composed of halophile fresh plants, seeds, dry plants... whereas the experimental group (n = 6) received an HC diet (25 % of barley and 75 % of dried dates) corresponding to a daily caloric intake of 22.5 calories/animal. Details of the composition of the high-carbohydrate diet (HCD) are presented in Table 1. After six months of diet

Table 1
Diet compositions according to Nicole Tonelli and François Gallouin, Fruit and seeds comestibles worldwide, 7th edition. MedPharm Scientific Publishers/Taylor & Francis, 2008.

Nutritional composition	Barley (g/100 g)	Dried dates (g/100 g)
Carbohydrates	**63.30**	**65**
Starch	61.59	–
Simple sugars	1.71	
Glucose	–	25
Fructose	–	25
Saccharose	–	14
Sorbitol	–	1
Protein	11.2	2
Lipids	2.1	0.5
Water	12.2	20
Fibers	9.8	9
Vitamins	0.015	0.012
Minerals & Trace Elements	0.956	0.862
Calories	314 kcal	275 kcal

administration, the animals were killed by decapitation. The livers and fat pads (mesenteric. genital and perirenal) were totally removed, rinsed with cold 0.9 % NaCl, weighed, and cut. One part of the liver was fixed in 10% neutral buffered formalin for histopathological investigations. The other part was first frozen in liquid nitrogen and then stored at–80 °C for later use in biochemical studies.

2.2. Biochemical analyses

Blood samples were collected after 24 weeks of feeding by puncture from the retro-orbital venous plexus into heparinized or EDTA-containing tubes. The plasma was immediately separated by centrifugation at 3000 *g* for 10 min and rapidly stored at–20 °C until analysis. Plasma glucose, total cholesterol, triacylglycerol (TG), HDL cholesterol and reliable markers of hepatic function (aspartate aminotransferase, AST; alanine aminotransferase, ALT) were measured by using the corresponding kits for analysis (Spinreact, Spain). Plasma LDL cholesterol concentration was calculated by using the equation of Friedewald. Plasma insulin was measured by radioimmunoassay (INSULIN-CT kit, Cisbio assay, France). Homeostasis model assessment of insulin resistance (HOMA-IR) was calculated according to the following formula: HOMA-IR = fasting insulin (μU/mL) × fasting glucose (mmol/L)/22.5.

2.3. Histopathology

A portion of liver (100 mg) was fixed with 10% formalin for 24 h, dehydrated in graded ethanol, and embedded in paraffin. The samples were cut into 5-μm-thick sections and stained with Masson's trichrome for evaluation by light microscopy for fibrotic deposition.

2.4. Hepatic lipid analyses

Liver total lipids were extracted by the method of Folch et al. [14]. The concentrations of triglycerides and cholesterol in the hepatic lipid extracts were measured using the same enzymatic kits as those used for plasma analysis.

3. Estimation of hepatic oxidative stress

3.1. Liver homogenate preparation

Liver samples from each gerbil were homogenized in Tris/EDTA buffer (50 mM Tris. 0.1 mM EDTA. pH 7.6) to obtain a 10% (w/v) liver homogenate. An aliquot of tissue homogenate was centrifuged at 1,000 rpm for 5 min at 4 °C for the estimation of MDA (malondialdehyde). The remaining volume of homogenate was centrifuged at 9,600 rpm for 20 min at 4 °C. The supernatant was collected and used for the estimation of GSH (reduced glutathione), and for measuring the activity of SOD (superoxide dismutase), CAT (catalase), and GST (glutathione-*S*-transferase).

3.2. Markers of lipid peroxidation

Lipid peroxidation was assessed indirectly by the measurement of secondary products malondialdehyde (MDA) using a thiobarbituric acid (TBA) method according to the protocol. MDA formed a colored complex in the presence of thiobarbituric acid, which was detected by spectrophotometrical measurement of the absorbance at 535 nm [15].

3.3. Evaluation of antioxidant enzyme activity

3.3.1. Activity of SOD

Superoxide dismutase was estimated using the method described in [16]. Superoxide anions are generated during the oxidation of pyrogallol under test conditions and SOD enzyme inhibits the oxidation of pyrogallol. The enzyme activity is measured by monitoring the rate of decrease in optical density at 420 nm. One unit of enzyme was defined as the amount of enzyme required to produce 50% inhibition of pyrogallol autoxidation under the assay conditions and expressed as U/mg protein.

3.3.2. Activity of catalase

Catalase activity was assayed by the method of Aebi [17]. The rate of H_2O_2 decomposition was followed by monitoring absorption at 240 nm. The enzyme activity was expressed as millimoles of H_2O_2 consumed per minute per milligram of protein.

3.3.3. Activity of GST

GST activity was measured using the method of Habig et al. [18]. Briefly, 1 mM CDNB was added to a buffer solution containing 1 mM GSH and an aliquot of the sample to be tested. Upon addition of CDNB, the change in absorbance at 340 nm was measured as a function of time. The extinction coefficient for this reaction is 9.6 $mM^{-1}{\cdot}cm^{-1}$.

3.3.4. Concentration of GSH

GSH level was estimated using a colorimetric technique as mentioned by Ellman [19], based on the development of a yellow color when 5,5-dithio-bis-(2-nitrobenzoic acid) (DTNB) is added to compounds containing sulfhydryl groups. Absorbance was recorded at 412 nm. The total GSH content was expressed as nanomoles of GSH per milligram of protein.

3.4. Protein estimation

The protein content was determined using Bradford's method [20], bovine serum albumin being taken as the standard.

3.5. RNA extraction and RT-qPCR

Total RNA was isolated according to [21]. Real-time quantitative RT-PCR analyses were performed with 50 ng of cDNA/3 mM MgCl2/250 nM sense and antisense primers (Proligo, Boulder, CO, USA) in a final reaction volume of 25 μl by using the qPCR TM Core Kit (Eurogentec, Brussels) and the MyiQ real-time PCR detection system (Bio-Rad). Specific primers were designed with Primer Express software (Table 2). The relative quantitation of each gene was calculated after normalization to 18S ribosomal RNA by using the comparative CT method.

Table 2
Sequences of the primers used for quantitative real-time PCR.

Genes	primer sequenses
FAS	
Sense	5′-tgc tcc cag ctg cag gc -3′
AntiSense	5′-gcc cgg tag ctc tgg gtg ta-3′
SREBP1c	
Sense	5′-gga gcc atg gat tgc aca tt-3′
AntiSense	5′-ggc ccg gga agt cac tgt-3′
ACC	
Sense	5′-tgg gca cag acc gtg gta g-3′
AntiSense	5′-ggt ctt aaa tgc aga gtc tgg gaa-3′
SREBP2	
Sense	5′-ccc ttg act tcc ttg ctg ca-3′
AntiSense	5′-gcg tga gtg tgg gcg aat c-3′
HMG CoA synthase	
Sense	5′-gcc gtg aac tgg gtc gaa-3′
AntiSense	5′-gca tat ata gca atg tct cct gca a-3′
HMG CoA reductase	
Sense	5′-gat tct ggc agt cag tgg gaa-3′
AntiSense	5′-gtt gta gcc gcc tat gct cc-3′
aSma	
Sense	5′-ttg gaa aag atc tgg cac cac-3′
AntiSense	5′-gca gta gtc acg aag gaa tag-3′
Col1A1	
Sense	5′-ccc cgg gac tcc tgg act t-3′
AntiSense	5′-gctccgacacgccctctctc-3′
TGF-β	
Sense	5′-gcctgagtggctgtcttttgac-3′
AntiSense	5′-catggatggtgcccaggt-3′
GRP78	
Sense	5′-gaa agg atg gtt aat gat gct gag-3′
AntiSense	5′-gtc ttc aat gtc cgc atc ctg-3′
ORP150	
Sense	5′-tgt cct ctt ggc aga cct gtt g-3′
AntiSense	5′-ttt tcc tcc gag att cct tgt tc-3′
18S	
Sense	5′-ggg agc ctg aga aac ggc-3′
AntiSense	5′-ggg tcg gga gtg ggt aat tt-3′

3.6. Preparation of nuclear extracts

Nuclear extracts were prepared as described in [22]. Livers were removed and quickly rinsed in an ice-cold phosphate-buffered saline solution with pepstatin (5 μg/ml), leupeptin (5 μg/ml), and aprotinin (2 μg/ml) as protease inhibitors. The livers were then transferred into a beaker, on ice, containing the homogenization buffer (2 M sucrose, 10 mM Hepes, pH 7.6, 25 mM KCl, 0.15 mM spermine, 0.5 mM spermidine, 1 mM EDTA, 10% glycerol, 0.5 mM dithiothreitol) and minced with scissors. After processing in a Dounce apparatus in fresh buffer on ice, the homogenates were layered on 2 M sucrose cushions and centrifuged at 80,000 g for 35 min at 0 °C. The nuclear pellets were then rinsed in a buffer containing 10 mM of Tris, pH 7.4, 10 mM of NaCl, 3 mM of $MgCl_2$, resuspended in a 20 mM Hepes, pH 7.9, 0.4 M NaCl, 1 mM EDTA, 1 mM EGTA, 1 mM dithiothreitol buffer and incubated 15 min on ice. After spinning 5 min at 10,000 rpm, aliquots of the supernatants were stored at –80 °C. The protein content was determined as described by Bradford, using bovine serum albumin as a standard.

3.7. Statistical analysis

Data were statistically analyzed by performing a nonparametric Mann–Whitney test using GraphPad Prism to compare experimental groups (v. 6.00 for Windows, San Diego, CA, USA). Data were expressed as mean < remove picture pageno 5> standard error of the mean (SEM) and considered significant at $P < 0.05$.

4. Results

4.1. Body and liver weights, body fat accumulation and biochemical parameters

The administration of a high-carbohydrate diet for 6 months resulted in significant increases in the final body, liver and abdominal fat weights compared with those in the gerbils from the control group (Table 3). The liver and fat indices increased 1.08 and 2.5 times, respectively, compared to the control diet, after a 24-week HC diet. The HCD group showed higher plasma concentrations of triglycerides ($P < 0.001$) and total cholesterol ($P < 0.05$). However, the mean plasma HDL cholesterol and LDL cholesterol levels were not statistically different between the two groups. Plasma glucose was not modified in experimental gerbils ($P = 0.123$), whereas plasma insulin level and HOMA-IR index were significantly increased ($P < 0.05$) with the HCD compared to the control diet (Table 3). The 24-week feeding of HCD to gerbils did not significantly affect ALT and AST activities (markers of liver function) (Table 3).

4.2. Liver TG and cholesterol levels

The liver TG and TC levels are shown in Table 3. HCD feeding significantly increased the hepatic TG levels (188.4 ± 26.20 mg/g) compared with the control group (82.97 ± 12.07 mg/g; $P < 0.01$). The hepatic TC content in the HCD group was increased two times compared to control animals.

Table 3
Physiological and plasma parameters in control and HCD gerbils after 24 weeks of treatment.

	Control ($n = 6$)	Experimental ($n = 6$)
Body weight (g)	27.68 ± 0.88	31.43 ± 0.70**
Fat pads (mesenteric, genital and perirenal) (g)	0.49 ± 0.03	1.35 ± 0.15***
Fat to body weight ratio (%)	1.76 ± 0.10	4.35 ± 0.57**
Liver weight (g)	0.98 ± 0.005	1.19 ± 0.005*
Liver to body weight ratio (%)	3.51 ± 0.21	3.79 ± 0.11
Hepatic triglycerides (mg/g liver)	82.97 ± 12.07	188.4 ± 26.20**
Hepatic total cholesterol (mg/g liver)	41.45 ± 8.20	86.86 ± 3.85***
Plasma triglycerides (mg/dl)	93.91 ± 10.04	208 .7 ± 18.48***
Plasma total cholesterol (mg/dl)	103.1 ± 7.05	136.8 ± 9.03*
Plasma HDL-c (mg/dl)	57.07 ± 3.55	51.52 ± 5.20
Plasma LDL-c (mg/dl)	28.81 ± 8.95	42.33 ± 8.14
Plasma glucose (mg/dl)	94.74 ± 3.73	107.8 ± 6.78
Plasma insulin (mU/mL)	48.38 ± 2.21	183.9 ± 47.26*
HOMA-IR index	11.34 ± 0.79	48.91 ± 12.78*
ASAT (U/l)	32.08 ± 7.02	56.84 ± 25.71
ALAT (U/l)	18.95 ± 2.68	24.78 ± 4.17

Data are expressed as means ± SEM.
* $P < 0.05$.
** $P < 0.01$.
*** $P < 0.001$ versus the control group.

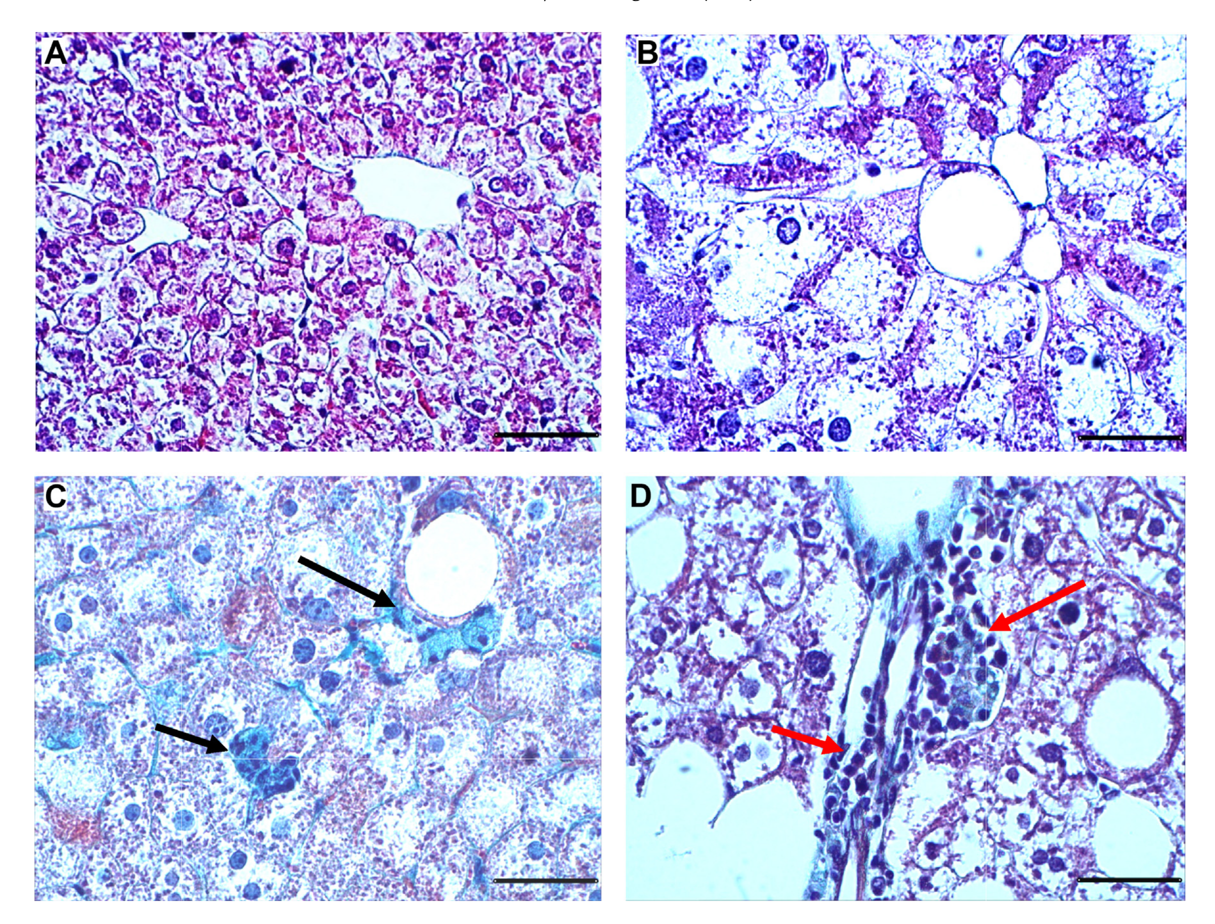


Fig. 1. Representative Masson Trichrome stained liver sections from gerbils fed with normal diet (A) or high carbohydrate diet (B–D) during 24 weeks. Trichrome Masson staining was performed to detect fibrotic areas (in green, indicated by arrows). Sections were observed at 400-fold magnification (scale bars: 50 μm).

4.3. Histological analysis of the liver tissues

Representative photomicrographs of liver sections are described in Fig. 1. Liver sections of control animals showed a normal liver architecture formed of hepatic lobules. Briefly, each lobule is made up of radialing plates. Strands of cells form a network around a central vein (Fig. 1A). The histological examination of liver tissue of gerbils submitted to the HC diet revealed variable changes. These changes were evidenced by a marked micro and macro steatosis characterizing the NAFLD status (Fig. 1B). Trichrome staining showed a marked collagen deposition within the pericellular space at sites where fatty degeneration of hepatocytes occurred (Fig. 1C). Also, marked mononuclear cell infiltrates in the portal system space (red arrows) were observed (Fig. 1D).

4.4. Lipid peroxidation of the liver

As shown in Fig. 2A, the level of malondialdehyde (MDA), an index of lipid peroxidation in liver homogenates was significantly increased by 67% in the HCD group ($P < 0.05$) compared to the control group.

4.5. Activities of antioxidant enzymes in liver tissue

The effect of a long-term administration of HCD on activities of liver antioxidant enzymes is depicted in Fig. 2(B–E). GSH (reduced glutathione) levels were statistically significantly lower in the HCD group than in the control group (Fig. 2B). SOD (superoxide dismutase) activities did not yield statistically significant differences due to the large variability observed (HCD: (0.600 ± 0.129 U/mg protein) vs. (0.914 ± 0.331 U/mg protein) in control animals). As illustrated in Fig. 2A and B, the GST (glutathione-*S*-transferase) and CAT (catalase) activities were unchanged between these two groups.

4.6. Hepatic gene expression in gerbils

4.6.1. mRNA expression of SREBP1c. ACC and FAS

Sterol regulatory element-binding protein-1 (SREBP-1) is a nuclear transcription factor that transcriptionally activates nearly all the genes involved in *de novo* lipogenesis [23]. Acetyl-CoA carboxylase (ACC) and fatty acid synthase (FAS) are important downstream target genes of SREBP-1 and are the rate-limiting enzymes of

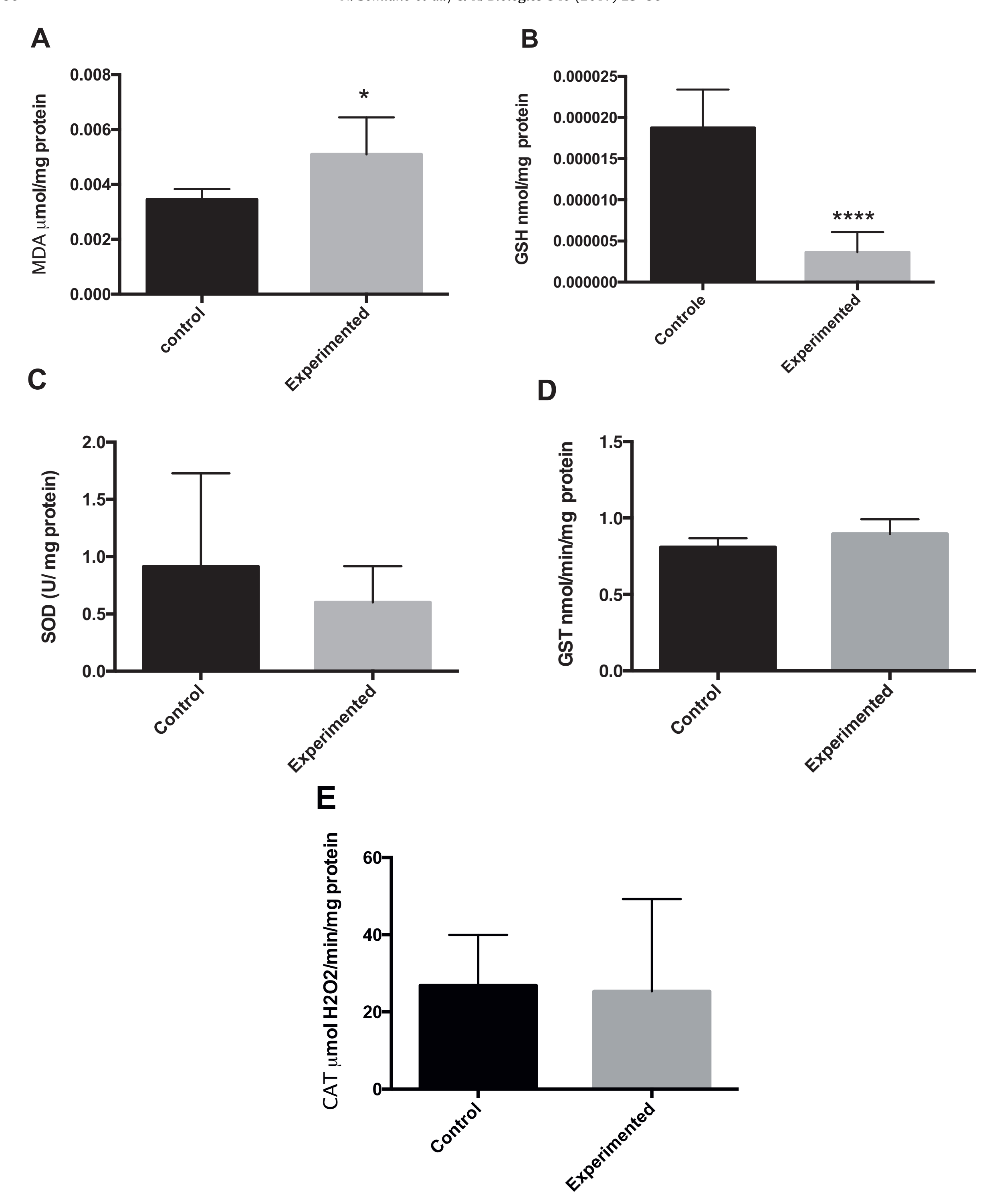


Fig. 2. Oxidative stress in liver tissue. The intrahepatic contents in MDA (A), GSH (B), SOD (C), GST (D) and CAT (E) were respectively measured in frozen liver homogenate of control or treated gerbils. * $P < 0.05$. **** $P < 0.0001$ versus control group.

palmitate formation. Compared with controls, HCD feeding alone significantly up-regulated the hepatic mRNA expression of SREBP1-c ($P < 0.01$), FAS ($P < 0.001$) and ACC ($P < 0.01$) (Fig. 3A–C).

4.6.2. mRNA expression of SREBP2, HMG CoA synthase and HMG CoA reductase

SREBP-2 preferentially regulates target genes involved in cholesterol biosynthesis and uptake in the liver, such as

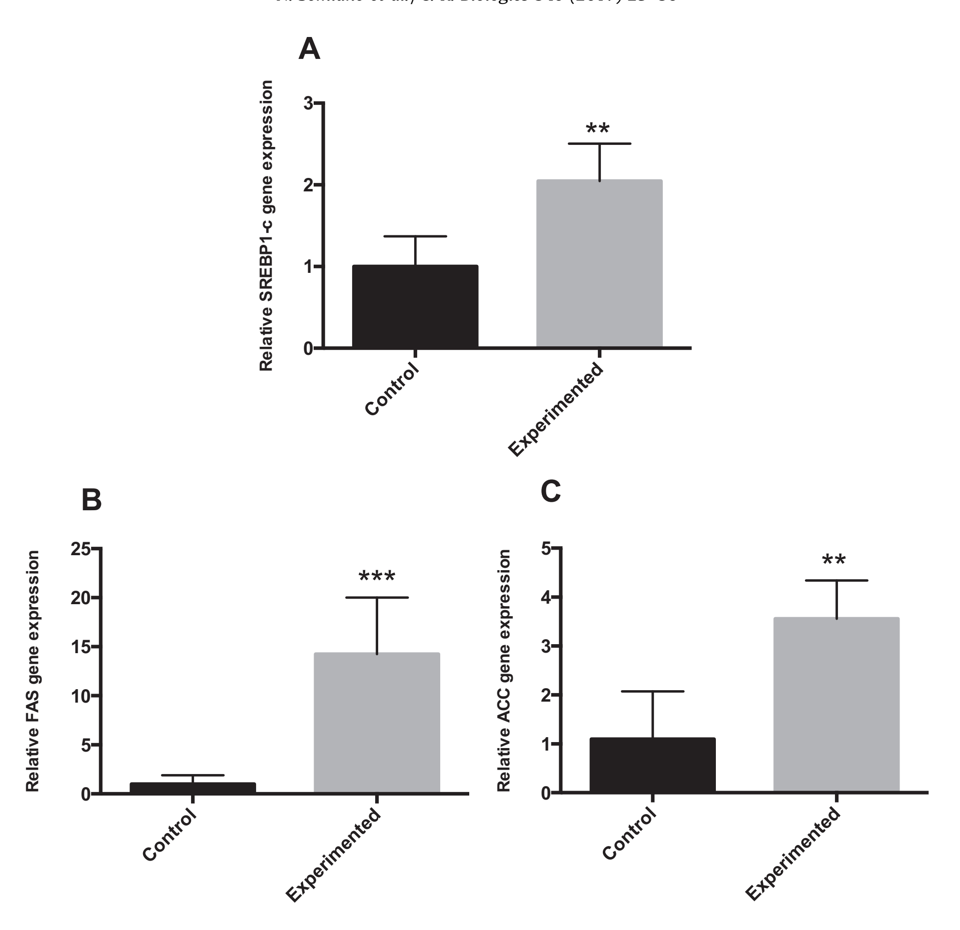


Fig. 3. mRNA expression for genes involved in fatty acid synthesis in the liver of gerbils fed normal diet or high carbohydrate diet for 24 weeks. ** $P < 0.01$. *** $P < 0.001$ vs. the corresponding values in control gerbils.

3-hydroxy-3-methylglutaryl-CoA synthase (HMGCS) and 3-hydroxy-3-methylglutaryl-CoA reductase (HMGCR) [24]. The mRNA expressions of SREBP-2 and HMG CoA synthase were significantly increased in HCD gerbils as compared to controls (Fig. 4A–B). However, HMGCoA reductase mRNA expression was not significantly different between the groups, due to the large variability observed, but tended to increase as compared to controls (Fig. 4C).

4.6.3. mRNA expression of α-SMA, Col1A1 and TGF-β

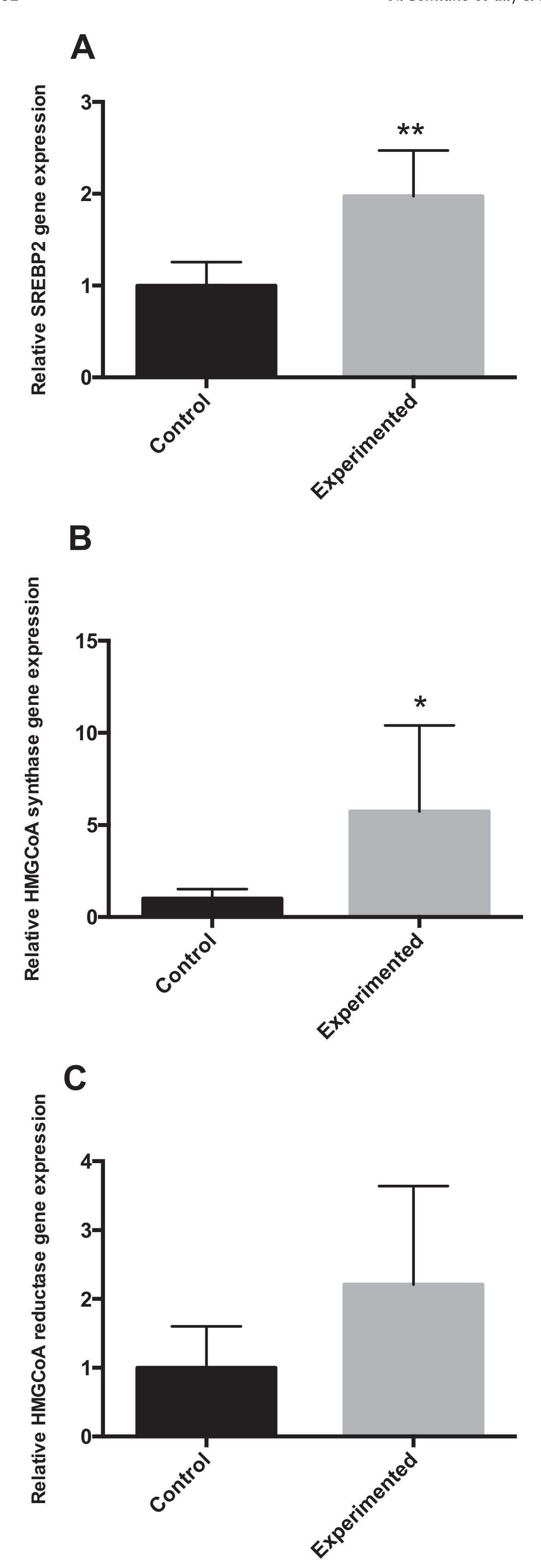
Our results show that mRNA gene expression for α-SMA (α-smooth muscle actin, a gene related to stellate cell activation) was approximatively two-fold higher in HCD group compared to control group ($P < 0.05$). Similarly, the hepatic mRNA expression of Col1A1 (collagen 1A1) was up-regulated (1.5-fold) in HCD group compared to control group (Fig. 5B). However, liver expression of TGF-β (transforming growth factor) remained unchanged between the two groups (Fig. 5C).

4.6.4. mRNA expression of GRP78 and ORP150

Abnormal endoplasmic reticulum (ER) stress contributes substantially to hepatocyte cell death during altered lipid metabolism [25]. To investigate whether ER stress was associated with the pathogenesis of hepatic steatosis, we studied GRP78 (glucose-regulated protein 78) by RT-PCR. GRP78 acts as an apoptotic regulator by protecting or promoting cell death during ER stress [26]. The RT-PCR results indicated that the GRP78 mRNA expression level was elevated in the experiment group, compared with the corresponding control groups (+ 44 %) (Fig. 6A). The 150-kDa oxygen-regulated protein (ORP150) is an anti-apoptotic ER resident chaperone that exerts a protective effect against ER stress-dependent apoptosis [27]. As shown in Fig. 6B, ORP150 mRNA expression was significantly increased in the HCD group compared with the control group ($P < 0.05$).

5. Discussion

In this study, after 24 weeks of feeding with HCD (dates and barley), gerbils exhibited increased body weight, visceral fat mass, visceral fat/body weight ratio, and liver/body weight ratio when compared with control animals. HCD treatment also caused significant increments in the plasma TC and TG levels, elevated hepatic TG and TC contents, and marked lipid droplet deposition in the liver sections, which are consistent with signs of fatty liver. At



this time, the liver enzymes (ALT and AST) levels were normal, suggesting that the presence of NASH does not necessarily correlate with higher levels of these liver transaminases. Indeed, ALT levels are persistently normal in more than one half of the patients with NAFLD and biopsy proven NASH [28]. It is interesting to note that after 24 weeks of dietary treatment, the HCD group exhibited no significant changes (but a 14% increased trend) in the plasma glucose level. In addition, HCD induced hyperinsulinemia and insulin resistance (confirmed by HOMA-IR calculation).

Body fat distribution appears to be even more important than the total amount of adipose tissue, and the visceral fat mass is strongly linked to insulin resistance and NAFLD [29]. Visceral fat-released FFAs are transported to the liver by the portal vein and may contribute to hepatic steatosis, production of triglyceride rich VLDL, and elevated β-oxidation [30].

A large body of evidence supports a complex interaction between NAFLD and insulin resistance [31]. Some studies have suggested that the abdominal adipose tissue plays an important role in the development of insulin resistance [32]. Furthermore, visceral adipose tissue (VAT), a harmful fat deposit, has been considered to induce liver insulin resistance and further induce systemic insulin resistance [33].

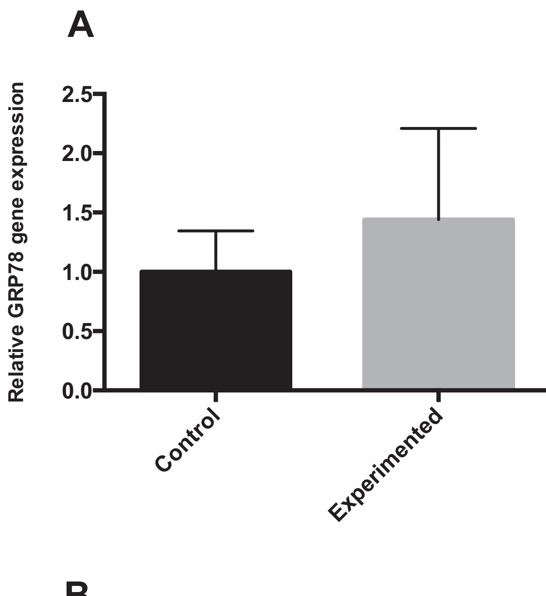
This study demonstrates that a high-carbohydrate diet was able to induce obesity-related NAFLD in our experimental model. Animal models in which NAFLD was induced by simple carbohydrate-rich diets (usually fructose) are less numerous, and in most of them only hepatic steatosis was observed [34,35]. Hyperinsulinemia led to increased hepatic synthesis of fatty acids, triglyceride accumulation in the hepatocytes, with subsequent steatosis. Several *in vivo* and *in vitro* studies have indicated that hepatic TG deposition may not be harmful; rather, it may represent a protective mechanism against FFA-induced lipotoxic liver injury by storing FFAs in the form of TGs [36].

Increased calorie intake, especially refined sugar and fructose, correlates with increases in dyslipidemia, IR, and nonalcoholic fatty liver disease (NAFLD) [37]. NAFLD is the first step in the hepatic diseases that can evolve into steatohepatitis (NASH), with inflammatory infiltration resulting in cirrhosis, and even hepatocarcinomas [38].

Epidemiologic studies suggested that a diet high in refined carbohydrates (HCD) (50–65% of energy from carbohydrates, high glycemic index, and low in fiber) could promote NAFLD progression [39]. Our work demonstrates that gerbils fed a high glycemic index diet (GI for dates is 70) for 24 weeks had greater hepatic TGs and adiposity than gerbils fed a low glycemic index diet. Our results fit with those of Scribner et al. [40]. In addition, several experiments showed that the high-glycemic index

Fig. 4. mRNA expression of SREBP2 and SREBP2 (HMGCoA synthase, HMGCoA reductase) target gene involved in cholesterol metabolism in the liver of gerbils fed with normal diet or high-carbohydrate diet for 24 weeks. * $P < 0.05$. ** $P < 0.01$ vs. the corresponding values in control gerbils.

Fig. 5. mRNA expression for genes related to hepatic fibrosis in the liver of gerbils fed with normal diet or high-carbohydrate diet for 24 weeks. * $P < 0.05$ vs. the corresponding value in control gerbils.



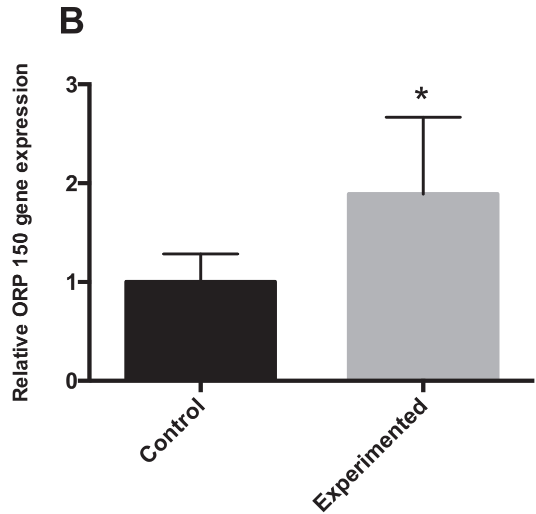


Fig. 6. Expression of ER stress markers in the livers of control and experimental gerbils. * $P < 0.05$ vs. the corresponding values in control gerbils.

carbohydrate has a close relationship with obesity, IR, and increased plasma and hepatic TGs [40]. The grade of hepatic steatosis seems to be associated with the glycemic index of the diet, regardless of total energy or carbohydrate intake [39]. The underlying mechanism is not fully elucidated, but some hypotheses have been proposed. Foods with high glycemic indices enhance the hepatic influx of glucose. The excess of hepatic glucose exceeds the ability of glycogen production; therefore, this carbohydrate will be used for the synthesis of new TG through DNL within the hepatocytes. An elevated-glycemic index food might augment oxidative stress, which can contribute to NASH development [41].

Similarly, Maersk et al. [42] found that a daily intake of 1 L of a sucrose-sweetened soft drink for six months increased liver lipids in overweight participants compared with the intake of the same amount of milk, diet cola, or

water. Carbohydrate-induced accumulation of fat in the liver can lead to nonalcoholic fatty liver disease (NAFLD) [43].

The composition of diet and especially the amount of glucose/starch may influence the health effects of fructose. As fructose is present with glucose in most food products, it is more practical and relevant to look at the effects of fructose and glucose together than at the effects of fructose alone. A larger increase in DNL after eating fructose and glucose together (50:50 glucose:fructose) rather than the same amount of pure glucose has been shown [44]. Eating glucose with fructose is likely to affect fructose's health effects by stimulating the flow of fructose to DNL [45]. This effect could be due to both increased absorption capacity for fructose when co-ingested with glucose and therefore greater availability of fructose carbon atoms going towards DNL and increased blood insulin levels when glucose is present in the diet. Insulin stimulates DNL directly and indirectly by inhibiting other important metabolic pathways for fructose, such as gluconeogenesis.

In the present study, HCD-fed gerbil had severe hepatic steatosis. This HCD-induced elevated steatosis was associated with the significant upregulation of DNL genes, including FAS (an enzyme that catalyzes long-chain fatty acid biosynthesis through the condensation of acetyl-CoA and malonyl-CoA and ACC, as well as SREBP (a key regulator of fatty acid synthesis in the liver gene expression). This evidence is consistent with previous in vivo studies and clinical observations that HCD-induced NAFLD was associated with elevated hepatic DNL [39]. Donnelly et al. [4] observed that patients with NAFLD have elevated fasting DNL compared with healthy individuals. Altering dietary macronutrient contents can induce differential metabolic consequences in the liver [46]. Excessive dietary carbohydrates induced glucose conversion to FA by DNL [46]. It is important to note that diets rich in complex carbohydrates and fibers did not induce clinical DNL in humans, suggesting a potential interaction between digestibility/structure of carbohydrates and DNL [47]. The deleterious effect of our diet is attributed to dry dates that contain essentially simple sugars.

The liver is the major organ involved in cholesterol metabolism. Sterol regulatory element-binding protein-2 (SREBP-2) promotes the expression of target genes involved in cholesterol biosynthesis and uptake in the liver, such as 3-hydroxy-3-methylglutaryl-CoA synthase (HMGCS) and 3-hydroxy-3-methylglutaryl-CoA reductase (HMGCR) [24]. The data from the present investigation (Fig. 4) showed that the SREBP-2 precursor and nuclear active forms as well as the HMGCR and HMGCS target genes were significantly up-regulated by HCD in gerbil.

Previous research has shown that a fatty liver induced by a high saturated fat diet shows signs of endoplasmic reticulum (ER) stress in a rodent model [48]. The endoplasmic reticulum is an important organelle responsible for protein synthesis, folding, assembly and transport in eukaryotic cells. GRP78 is a member of the HSP70 family abundant in the lumen of ER, and plays important roles as a molecular chaperone that removes misfolded proteins in ER lumen. Overexpression of GRP78 has been shown to increase ER stress resistance and to have beneficial effects in several cell types [49]. In addition, the survival response activates genes that encode ER-residing chaperones such as GRP78/Bip, which uses energy derived from ATP hydrolysis to prevent the aggregation of ER proteins, and is considered the classical marker of UPR activation.

To confirm the involvement of ER in fatty liver developed in our experimented gerbils, we studied GPR78 and ORP150 by quantitative RT-PCR, and the data in Fig. 5 show that GRP78 moderately increased in *G. gerbillus* liver. It was demonstrated that obesity is associated with the induction of ER stress predominantly in the liver and adipose tissues [50]. Previous research has shown that fatty liver induced by a high sucrose diet and high saturated fat diet shows clear ER stress events in a rodent model [48].

In the current study, we observed a coordinated transcriptional upregulation of lipogenesis genes together with ER stress. Lipid accumulation and lipotoxicity are known to positively regulate the ER stress response through a cycle that leads to further toxic insults upon the liver [51].

Abnormal ER stress contributes substantially to hepatocyte cell death during altered lipid metabolism [24]. Thus, modulation of hepatic ER stress becomes crucial in the understanding of the extent of its contribution to the pathogenesis of various hepatic disorders. Induction of ORP150 exhibits protective roles in the prevention of ER stress [27] and dysregulation of calcium homeostasis and apoptosis. Our work showed that the levels of ORP150 in the liver of control gerbils were significantly greater compared with that of experimented gerbils (Fig. 5B), which supports the speculation that ORP150 expression could be beneficial under the local challenging conditions of ER stress.

The induction of ORP150 mediates the amelioration of hepatic ER stress and apoptosis by AMPK *in vitro* and *in vivo*. [52] Collectively, these results indicate that chronic HC diet altered, at least partially, endoplasmic reticulum functions and induced stress conditions.

Collagen 1A1 (Col1A1) is the major hepatic collagen subtype associated with NASH in rodents and humans [53]. HC-feeding for 24 weeks greatly elevated biochemical and histological markers of fibrosis. The fibrotic status of the liver is governed by a balance between extracellular matrix (ECM) deposition and turnover. The biochemical (expression of αSMA) and histological evidence of fibrosis (Fig. 1) in HC fed gerbils provide clear evidence that the rate of collagen production exceeds that of its degradation.

Although it has been widely proposed that stellate cells are the main contributor to ECM deposits in the liver, it is possible that other cell types are involved [54]. MMPs are a family of zinc-dependent proteinases that are responsible for the degradation of ECM proteins. MMP dysregulation has been implicated in the pathophysiology of obesity and diabetes.

Overwhelming evidence indicates that the perisinusoidal hepatic stellate cells (HSCs) are the major source of liver fibrosis of any etiology [55]. During liver injury, HSCs

transdifferentiate from their quiescent physiologic to the fibrogenic phenotype. Such a transformation is induced by inflammatory mediators (e.g., TNFα) and reactive oxygen species and apoptotic bodies arising from dying hepatocytes, and activated HSCs are characterized by expression of αSMA, a marker not found in quiescent HSCs [56,57].

Activation of HSCs is further characterized by the overexpression of α-SMA, MMP-2, and MMP-9 [58]. Although the role of HSC activation in nonalcoholic fatty liver disease (NAFLD) has not been completely clarified, several studies have reported increased HSC activation in nonalcoholic steatohepatitis (NASH) [59].

Several studies have demonstrated that insulin resistance is associated with advanced stages of fibrosis in NAFLD [60]. Because insulin promotes HSC activation and insulin sensitizers can attenuate hepatic fibrosis in NASH, it has been suggested that insulin resistance plays an important role in NASH-related fibrogenesis [61]. It is understood that oxidative stress induces the activation of HSCs in NASH [62].

In addition to liver fibrosis, it is well-established that oxidative stress also is very important in the development and progression of NASH. It has been shown that chronic oxidative stress, generated through the oxidation of cytotoxic free fatty acids, may lead to cytokine upregulation and depletion of hepatic antioxidant levels [63]. In addition, enhanced lipid peroxidation leads to the generation of reactive by-products, such as MDA, which have been shown to further stimulate cytokine production [64]. In the current study, there was a significant decrease in GSH content and SOD activity in HC-fed gerbils, and a significant increase in MDA levels. These findings are in agreement with those of Leclercq [65], who reported that diets with high amounts of simple carbohydrates induce hypertriglyceridemia, resulting in a reduction of the antioxidant reserves [65].

Most previous studies reported alterations in the expression and activity of antioxidant enzymes in the liver of fructose-fed rodents, although the course of these alterations varied largely. Some authors observed that a fructose-rich diet reduced the antioxidant capacity and caused oxidative damages in the liver [66], whereas others reported the absence of oxidative stress [67] or adaptation to modest oxidative stress [68] in fructose-fed rats. Alternatively, Girard et al. [69] noticed that a fructose-rich diet enhanced the total antioxidant capacity of the liver.

6. Conclusion

In summary, the present study demonstrates that a long-term (24-week) consumption of a high-carbohydrate diet induces adiposity, insulin resistance, up-regulation of *de no*vo lipogenesis, ER stress, oxidative stress, and finally fatty liver. Altogether, these results suggest that *G. gerbillus* represents a valuable natural model for human diet-induced metabolic disorders and NAFLD.

Disclosure of interest

The authors declare that they have no competing interest.

Acknowledgments

We would like to thank Professor Ahmed Menad for her help and collaboration.

References

[1] A. Tonjes, M. Bluher, M. Stumvoll, Retinol-binding protein 4 and new adipocytokines in nonalcoholic fatty liver disease, Curr. Pharm. Design. 16 (2010) 1921–1928.
[2] R. Loomba, A.J. Sanyal, The global NAFLD epidemic, Nat. Rev. Gastroenterol. Hepatol. 10 (2013) 686–690.
[3] S.K. Erickson, Nonalcoholic fatty liver disease, J. Lipid. Res. 50 (2009) S412–S416.
[4] K.L. Donnelly, C.I. Smith, S.J. Schwarzenberg, J. Jessurun, M.D. Boldt, E.J. Parks, Sources of fatty acids stored in liver and secreted via lipoproteins in patients with nonalcoholic fatty liver disease, J. Clin. Invest. 115 (2005) 1343–1351.
[5] C. Postic, J. Girard, Contribution of de novo fatty acid synthesis to hepatic steatosis and insulin resistance: lessons from genetically engineered mice, J. Clin. Invest. 118 (2008) 829–838.
[6] K. Kantartzis, F. Schick, H.U. Haring, N. Stefan, Environmental and genetic determinants of fatty liver in humans, Dig. Dis. 28 (2010) 169–178.
[7] I. Shimomura, H. Shimano, B.S. Korn, Y. Bashmakov, J.D. Horton, Nuclear sterol regulatory element-binding proteins activate genes responsible for the entire program of unsaturated fatty acid biosynthesis in transgenic mouse liver, J. Biol. Chem. 273 (1998) 35299–35306.
[8] P. Ferre, F. Foufelle, SREBP-1c transcription factor and lipid homeostasis: clinical perspective, Horm. Res. 68 (2007) 72–82.
[9] P. Ferre, F. Foufelle, Hepatic steatosis: a role for de novo lipogenesis and the transcription factor SREBP-1c, Diabetes. Obes. Metab. 12 (2010) 83–92.
[10] P. Puri, F. Mirshahi, O. Cheung, R. Natarajan, J.W. Maher, J.M. Kellum, A.J. Sanyal, Activation and dysregulation of the unfolded protein response in nonalcoholic fatty liver disease, Gastroenterology 134 (2008) 568–576.
[11] D.L. Fang, Y. Wan, W. Shen, J. Cao, Z.X. Sun, H.H. Yu, Q. Zhang, W.H. Cheng, J. Chen, B. Ning, Endoplasmic reticulum stress leads to lipid accumulation through upregulation of SREBP-1c in normal hepatic and hepatoma cells, Mol. Cell. Biochem. 381 (2013) 127–137.
[12] Q.M. Anstee, R.D. Goldin, Mouse models in nonalcoholic fatty liver disease and steatohepatitis research, Int. J. Exp. Pathol. 1 (2006) 11–16.
[13] Y. Takahashi, Y. Soejima, T. Fukusato, Animal models of nonalcoholic fatty liver disease/nonalcoholic steatohepatitis, World. J. Gastroenterol. 18 (2012) 2300–2308.
[14] J. Folch, M. Lees, G.H. Sloane Stanley, A simple method for the isolation and purification of total lipides from animal tissues, J. Biol. Chem. 226 (1957) 497–509.
[15] H. Ohkawa, N. Ohishi, K. Yagi, Assay for lipid peroxides in animal tissues by thiobarbituric acid reaction, Anal. Biochem. 95 (1979) 351–358.
[16] S. Marklund, G. Marklund, Involvement of the superoxide anion radical in the autoxidation of pyrogallol and a convenient assay for superoxide dismutase, Eur. J. Biochem. 16 (1974) 469–474.
[17] H. Aebi, Catalase in vitro, Methods. Enzymol. 105 (1984) 121–126.
[18] W.H. Habig, M.J. Pabst, W.B. Jakoby, Glutathione-S-transferase. The first step in mercapturic acid formation, J. Biol. Chem 249 (1974) 7130–7139.
[19] G.L. Ellman, Tissue sulfhydryl groups, Arch. Biochem. Biophys. 82 (1959) 70–77.
[20] M.M. Bradford, A rapid and sensitive method for quantization of microgram quantities of protein utilizing the principle of protein-dye binding, Anal. Biochem. 72 (1976) 248–254.
[21] P. Chomczynski, N. Sacchi, Single-step method of RNA isolation by acid guanidinium thiocyanate-phenol-chloroform extraction, Anal. Biochem. 162 (1987) 156–159.
[22] A. Bobard, I. Hainault, P. Ferré, F. Foufelle, P. Bossard, Differential regulation of sterol regulatory element-binding protein 1c transcriptional activity by insulin and liver X receptor during liver development, .J. Biol. Chem. 280 (2005) 199–206.
[23] K. Wouters, P.J. van Gorp, V. Bieghs, M.J. Gijbels, H. Duimel, D. Lütjohann, A. Kerksiek, N. Maeda, B. Staels, M.V. Bilsen, R. Shiri-Sverdlov, M.H. Hofker, Dietary cholesterol rather than liver steatosis leads to hepatic infammation in hyperlipidemic mouse models of nonalcoholic steatohepatitis, Hepatology 48 (2008) 474–486.
[24] M.S. Brown, J.L. Goldstein, The SREBP pathway: regulation of cholesterol metabolism by proteolysis of a membrane-bound transcription factor, Cell 89 (1997) 331–340.

[25] M. Flamment, H.L. Kammoun, I. Hainault, P. Ferré, F. Foufelle, Endoplasmic reticulum stress: a new actor in the development of hepatic steatosis, Curr. Opin. Lipidol. 21 (2010) 239–246.
[26] J. Li, M. Ni, B. Lee, E. Barron, D.R. Hinton, A.S. Lee, The unfolded protein response regulator GRP78/BiP is required for endoplasmic reticulum integrity and stress-induced autophagy in mammalian cells, Cell. Death. Differ. 15 (2008) 1460–1471.
[27] M. Sanson, N. Auge, C. Vindis, C. Muller, Y. Bando, J.C. Thiers, M.A. Marachet, K. Zarkovic, Y. Sawa, R. Salvayre, A. Negre-Salvayre, Oxidized low-density lipoproteins trigger endoplasmic reticulum stress in vascular cells: prevention by oxygen-regulated protein 150 expression, Circ. Res. 104 (2009) 328–336.
[28] A.L. Fracanzani, L. Valenti, E. Bugianesi, M. Andreoletti, A. Colli, E. Vanni, C. Bertelli, E. Fatta, D. Bignamini, G. marchesini, S. Fargion, Risk of severe liver disease in nonalcoholic fatty liver disease with normal aminotransferase levels: a role for insulin resistance and diabetes, Hepatology 48 (2008) 792–798.
[29] G. Calamita, P. Portincasa, Present and future therapeutic strategies in nonalcoholic fatty liver disease, Expert. Opin. Ther Targets 11 (2007) 1231–1249.
[30] M.D. Jensen, Role of body fat distribution and the metabolic complications of obesity, J. Clin. Endocrinol. Metab. 93 (2008) S57–S63.
[31] H.H. Nam, D.W. Jun, H.J. Jeon, J.S. Lee, W.K. Saeed, E.K. Kim, Osthol attenuates hepatic steatosis via decreased triglyceride synthesis not by insulin resistance, World. J. Gastroenterol. 20 (2014) 11753–11761.
[32] M. Mamtani, H. Kulkarni, T.D. Dyer, L. Almasy, M.C. Mahaney, R. Duggirala, A.G. Comuzzie, J. Blangero, J.E. Curran, Waist circumference independently associates with the risk of insulin resistance and type 2 diabetes in Mexican American families, PLoS. One. 8 (2013) 153–159.
[33] P. Patel, N. Abate, Body fat distribution and insulin resistance, Nutrients 5 (2013) 2019–2027.
[34] R. Kohli, M. Kirby, S.A. Xanthakos, S. Softic, A.E. Feldstein, V. Saxena, P.H. Tang, L. Miles, M.V. Miles, W.F. Balistreri, S.C. Woods, R.J. Seeley, High-fructose, medium chain trans fat diet induces liver fibrosis and elevatesplasma coenzyme Q9 in a novel murine model of obesity and nonalcoholic steatohepatitis, Hepatology 52 (2010) 934–944.
[35] F. Armutcu, O. Coskun, A. Gürel, M. Kanter, M. Can, F. Ucar, M. Unalacak, Thymosin alpha 1 attenuates lipid peroxidation and improves fructose-induced steatohepatitis in rats, Clin. Biochem. 38 (2005) 540–547.
[36] L.L. Listenberger, X. Han, S.E. Lewis, S. Cases, R.V. Farese, D.S. Ory, J.E. Schaffer, Triglyceride accumulation protects against fatty acid-induced lipotoxicity, Proc. Natl. Acad. Sci. USA 100 (2003) 3077–3082.
[37] K. Nomura, T. Yamanouchi, The role of fructose-enriched diets in mechanisms of nonalcoholic fatty liver disease, J. Nutr. Biochem. 23 (2012) 203–208.
[38] L. Tappy, K.A. Le, C. Tran, N. Paquot, Fructose and metabolic diseases: new findings. New questions, Nutrition 26 (2010) 1044–1049.
[39] S. Valtueña, N. Pellegrini, D. Ardigò, D. Del Rio, F. Numeroso, F. Scazzina, L. Monti, I. Zavaroni, F. Brighenti, Dietary glycemic index and liver steatosis, Am. J. Clin. Nutr. 84 (2006) 136–142 [quiz 268–9].
[40] K.B. Scribner, D.B. Pawlak, D.S. Ludwig, Hepatic steatosis and increased adiposity in mice consuming rapidly vs. slowly absorbed carbohydrate, Obesity (Silver Spring) 15 (2007) 2190–2199.
[41] Y. Hu, G. Block, E.P. Norkus, J.D. Morrow, M. Dietrich, M. Hudes, Relations of glycemic index and glycemic load with plasma oxidative stress markers, Am. J. Clin. Nutr. 84 (2006) 70–76.
[42] M. Maersk, A. Belza, H. Stødkilde-Jørgensen, S. Ringgaard, S. Chabanova, S. Thomsen, S.B. Pedersen, A. Astrupe, B. Richeisen, Sucrose sweetened beverages increase fat storage in the liver, muscle, and visceral fat depot: a 6-morandomized intervention study, Am. J. Clin. Nutr. 95 (2012) 283–289.
[43] K.A. Page, O. Chan, J. Aroraetal, Effects of fructose vs glucose on regional cerebral blood flow in brain regions involved with appetite and reward pathways, JAMA 309 (2013) 63–70.
[44] E.J. Parks, L.E. Skokan, M.T. Timlin, C.S. Dingfelder, Dietary sugars stimulate fatty acid synthesis in adults, J. Nutr. 138 (2008) 1039–1046.
[45] F. Eytaz, S. de Giorgi, L. Hodson, N. Stefanoni, V. rey, P. Schnitter, V. Giusti, L. Tappy, Metabolic fate of fructose ingested with and without glucose in a mixed meal, Nutrients 6 (2014) 2632–2649.
[46] S. Solga, A.R. Alkhuraishe, J.M. Clark, M. Torbenson, A. Greenwald, A.M. Diehl, T. Magnuson, Dietary composition and nonalcoholic fatty liver disease, Dig. Dis. Sci. 49 (2004) 1578–1583.
[47] L.C. Hudgins, M.K. Hellerstein, C.E. Seidman, R.A. Neese, J.D. Tremaroli, J. Hirsch, Relationship between carbohydrate-induced hypertriglyceridemia and fatty acid synthesis in lean and obese subjects, J. Lipid. Res. 41 (2000) 595–604.
[48] D. Wang, Y. Wei, M.J. Pagliassotti, Saturated fatty acids promote endoplasmic reticulum stress and liver injury in rats with hepatic steatosis, Endocrinol. 147 (2006) 943–951.
[49] E.G. Lai, M.B. Bikopoulos, M. Wheeler, A. Rozakis-Adcock, A. Volchuk, Differential activation of ER stress and apoptosis in response to chronically elevated free fatty acids in pancreatic beta-cells, Am. J. Physiol. Endocrinol. Metab. 294 (2008) E540–E550.
[50] U. Ozcan, Q. Cao, E. Yilmaz, A.H. Lee, N.N. Lwakoshil, E. özdelen, G. Tunkman, C. Görgun, L.H. Glimcher, G.S. Hotamisligil, Endoplasmic reticulum stress links obesity, insulin action, and type 2 diabetes, Science 306 (2004) 457–461.
[51] L.H. Glimcher, A.H. Lee, From sugar to fat: how the transcription factor XBP1 regulates hepatic lipogenesis, Ann. NY. Acad. Sci. 1173 (2009) E2–E9.
[52] Y. Wang, W. Wu, D. Li, D. Wang, X. Wang, X. Feng, M. Xia, Involvement of oxygen-regulated protein 150 in AMP-activated protein kinase-mediated alleviation of lipid-induced endoplasmic reticulum stress, J. Biol. Chem. 286 (2011) 11119–11131.
[53] J.R. Clapper, M.D. Hendricks, G. Gu, C. Wittmer, C.S. Dolman, J. Herich, J. Athanasio, C. Villescaz, S.S. Soumitra, S. Ghosh, J.S. Heilig, C. Lowe, J.D. Roth, Diet-induced mouse model of fatty liver disease and nonalcoholic steatohepatitis reflecting clinical disease progression and methods of assessment, Am. J. Physiol Gastrointest. Liver. Physiol. 305 (2013) G483–G495.
[54] R. Bataller, D.A. Brenner, Hepatic stellate cells as a target for the treatment of liver fibrosis, Semin. Liver Dis. 21 (2001) 437–451.
[55] K.M. Thrailkill, R. Clay Bunn, J.L. Fowlkes, Matrix metalloproteinases: their potential role in the pathogenesis of diabetic nephropathy, Endocrine 35 (2009) 1–10.
[56] Y. Koyama, P. Wang, D.A. Brenner, T. Kisseleva, Stellate cells. portal myofibroblasts and epithelial-tomesenchymal transition, in: C.R. Gandhi, M. Pinzani (Eds.), Stellate cells in health and disease, Elsevier Inc., 2015, pp. 87–106.
[57] D. Hasegawa, M.C. Wallace, S.L. Friedman, Stellate cells and hepatic fibrosis, in: C.R. Gandhi, M. Pinzani (Eds.), Stellate cells in health and disease, Elsevier Inc., 2015, pp. 41–62.
[58] P. Pellicoro, P. Ramachandran, J.P. Iredale, J.A. Fallowfield, Liver fibrosis and repair: immune regulation of wound healing in a solid organ, Nat. Rev. Immunol. 14 (2014) 181–194.
[59] K. Kaji, H. Yoshiji, M. Kitade, Y. Ikenaka, R. Noguchi, Y. Shirai, Y. Aihara, T. Namisaki, J. Yoshii, K. Yanase, T. Tsujimoto, H. Kawaratani, H. Fukui, Combination treatment of angiotensin II type I receptor blocker and new oral iron chelator attenuates progression of nonalcoholic steatohepatitis in rats, Am. J. Physiol. Gastrointest. Liver Physiol. 300 (2011) G1094–G1104.
[60] Z. Bian, X. Ma, Liver fibrogenesis in nonalcoholic steato-hepatitis, Front. Physiol. 3 (2012) 248.
[61] E. Bugianesi, P. Manzini, S. D'Antico, E. Vanni, F. Longo, M. leone, P. Massarenti, A. Piga, G. Marchesini, M. Rizzetto, Relative contribution of iron burden, HFE mutations, and insulin resistance to fibrosis in nonalcoholic fatty liver, Hepatology 39 (2004) 179–187.
[62] G.H. Koek, P.R. Liedorp, A. Bast, The role of oxidative stress in nonalcoholic steatohepatitis, Clin. Chim. Acta. 412 (2011) 1297–1305.
[63] C. Garcia-Ruiz, A. Colell, A. Morales, N. Kaplowitz, J.C. Fernandez Checa, Role of oxidative stress generated form the mitochondrial electron transport chain and mitochondrial glutathione status in loss of mitochondrial function and activation of transcription factor nuclear factor-kappa B: studies with isolated mitochondria and rat hepatocytes, Mol. Pharmacol. 48 (1995) 825–834.
[64] D. Thong-Ngam, S. Samuhasaneeto, O. Kulaputana, N. Klaikeaw, N-acetylcysteine attenuates oxidative stress and liver pathology in rats with nonalcoholic steatohepatitis, World J. Gastroenterol. 13 (2007) 5127–5132.
[65] I.A. Leclercq, Antioxidant defence mechanisms: new players in the pathogenesis of nonalcoholic steatohepatitis, Clin. Sci. Lond. 106 (2004) 235–237.
[66] R. Crescenzo, F. Bianco, I. Falcone, P. Coppola, G. Liverini, S. Iossa, Increased hepatic de novo lipogenesis and mitochondrial efficiency in a model of obesity induced by diets rich in fructose, Eur. J. Nutr. 52 (2013) 537–545.
[67] P. Pasko, H. Barton, P. Zagrodzki, A. Izewska, M. Krosniak, M. Gawlik, M. Gawlik, S. Gorinstein, Effect of diet supplemented with quinoa seeds on oxidative status in plasma and selected tissues of high fructose-fed rats, Plant. Foods. Hum. Nutr. 65 (2010) 146–151.
[68] F. Francini, M.C. Castro, G. Schinella, M.E. Garcia, B. Maiztegui, M.A. Raschia, J.J. Gagliardino, M.L. Massa, Changes induced by a fructose-rich diet on hepatic metabolism and the antioxidant system, Life. Sci. 86 (2010) 965–971.
[69] A. Girard, S. Madani, F. Boukortt, M. Cherkaoui-Malki, J. Belleville, J. Prost, Fructose-enriched diet modifies antioxidant status and lipid metabolism in spontaneously hypertensive rats, Nutrition 22 (2006) 758–766.

C. R. Biologies 340 (2017) 37–46

Contents lists available at ScienceDirect

Comptes Rendus Biologies

www.sciencedirect.com



Taxonomy/Taxinomie

Wing geometry of *Phlebotomus stantoni* and *Sergentomyia hodgsoni* from different geographical locations in Thailand



Géométrie des ailes de Phlebotomus stantoni *et de* Sergentomya hodgsoni *originaires de différentes régions de Thailande*

Suchada Sumruayphol [a,*], Boonruam Chittsamart [a], Raxsina Polseela [b,c], Patchara Sriwichai [a], Yudthana Samung [a], Chamnarn Apiwathnasorn [a], Jean-Pierre Dujardin [d]

[a] Department of Medical Entomology, Faculty of Tropical Medicine, Mahidol University, 10400 Bangkok, Thailand
[b] Department of Microbiology and Parasitology, Faculty of Medical Science, Naresuan University, 65000 Phitsanulok, Thailand
[c] Centre of Excellence in Medical Biotechnology, Faculty of Medical Science, Naresuan University, 65000 Phitsanulok, Thailand
[d] UMR17 IRD–CIRAD INTERTRYP TA A 17/G, Campus international de Baillarguet, 34398 Montpellier cedex 5, France

ARTICLE INFO

Article history:
Received 27 June 2016
Accepted after revision 17 October 2016
Available online 24 November 2016

Keywords:
Phlebotomus stantoni
Sergentomyia hodgsoni
Geometric morphometrics
Sandfly
Thailand

ABSTRACT

Geographic populations of the two main sandflies genera present in Thailand were studied for species and population identification. Size and shape of *Phlebotomus stantoni* and *Sergentomyia hodgsoni* from different island and mainland locations were examined by landmark-based geometric morphometrics. Intraspecific and interspecific wing comparison was carried out based on 12 anatomical landmarks. The wing centroid size of *P. stantoni* was generally larger than that of *S. hodgsoni*. Within both species, wings from the continent were significantly larger than those from island populations. Size variation could be significant between geographic locations, but could also overlap between genera. The wing venation geometry showed non-overlapping differences between two species. The within-species variation of geometric shape between different geographical locations was highly significant, but it could not interfere with the interspecies difference. The lack of species overlapping in shape, and the high discrimination between geographic populations, make geometric shape a promising character for future taxonomic and epidemiological studies.

Mots clés :
Phlebotomus stantoni
Sergentomyia hodgsoni
Morphométrie géométrique
Phlébotome
Thaïlande

RÉSUMÉ

Quelques populations géographiques des deux genres principaux de phlébotomes présents en Thaïlande, *Phlebotomus* et *Sergentomyia*, ont été examinées sur la base de la géométrie alaire. En utilisant 12 repères anatomiques de l'aile, la taille et la forme des phlébotomes ont été comparées entre des populations insulaires et continentales. Deux espèces ont été examinées : *Phlebotomus stantoni* et *Sergentomyia hodgsoni*. La taille des ailes de *P. stantoni* était généralement plus importante que celle de *S. hodgsoni*, mais dans les deux espèces, les ailes des populations du continent étaient significativement plus grandes que celles des populations insulaires. La variation de la taille, même si elle pouvait être significative entre

* Corresponding author.
E-mail address: suchada.sum@mahidol.ac.th (S. Sumruayphol).

http://dx.doi.org/10.1016/j.crvi.2016.10.002

certaines localités, se chevauchait entre elles, et même quelque peu entre les deux genres. La géométrie de la nervation alaire n'a montré aucun chevauchement entre ces derniers. Au sein de chaque espèce, la géométrie de l'aile a montré des divergences très significatives entre zones géographiques. Cette distinction nette entre espèces et l'excellente discrimination géographique dans chacune d'elles font de la forme géométrique de l'aile un complément utile au diagnostic morphologique des phlébotomes, et un caractère prometteur pour les futures études épidémiologiques et biologiques de ces insectes.

1. Introduction

Phlebotomus stantoni (Newstead 1914) and *Sergentomyia hodgsoni* (Sinton 1933) are sandflies that belong to subfamily Phlebotominae (Diptera: Psychodidae). Sandflies are vectors of various pathogens, among which *Leishmania sp.*; therefore, their correct taxonomic identification is important for epidemiological investigations. *Phlebotomus* Rondani & Berte and *Sergentomyia* Franca & Parrot are *Leishmania* protozoa vectors in the Old World [1], while *Lutzomyia* spp. transmit New World leishmaniasis [1,2].

In Thailand, *P. stantoni* and *S. hodgsoni* are commonly found in cave dwellers [3–7]. These two species are sympatric in some places, especially on isolated islands in Chumphon province in the southern part of Thailand [8]. In particular, *Phlebotomus* and *Sergentomyia* specimens were found in swiftlet caves on Lang Ga Jiew Island of Chumphon province, and *S. hodgsoni* was the predominant sandfly species on isolated islands. The identification of sandfly species belonging to different genera is not difficult using morphological examination. Our objective was not to test for the morphometric recognition of different genera, but to assess the quality of species recognition within each genus in spite of possible geographic changes.

To set up the control strategies against leishmaniasis transmission, essentially an entomological surveillance program, it may be important to improve our knowledge about the distribution of vectors, or potential vectors. To reach such objective and to ensure regular updates require the use of low-cost, fast and accurate tools to identify sandflies. There have been very few studies on species variation of sandflies from different geographical locations, especially none in Thailand, using geometric morphometrics (GM). In this study, we investigated intraspecific and interspecific wing size and shape variation of *P. stantoni* and *S. hodgsoni* in different geographical locations, including between the mainland and isolated islands.

The information derived from this study could help to evaluate the morphometric approach as a routine characterizing tool for future epidemiological studies of sandflies in Thailand.

2. Materials and methods

2.1. Sandfly collection

Using Center for Disease Control (CDC) light traps, sandflies were collected in 2011 in seven different geographical locations across Thailand (Fig. 1). Isolated islands and mainland location sites were selected in this study. Three isolated islands, including Lang Ga Jiew (LGJ), Ka (KA), and Mapraw (MAP) Islands, were selected for sandfly collection; these three islands are located in the Gulf of Thailand, in Chumphon province, southern Thailand. LGJ Island is a small offshore island that covers an area of 0.063 km^2 and is located approximately 8 km away from the shore. MAP and KA islands are located approximately 1 km away from the shore. Four other mainland location sites were selected: a small sample from an urban location in Nonthaburi province (NTB), which is located in central Thailand, and other from limestone caves of Kanchanaburi province (KCB, western Thailand), Ratchaburi province (RCB, central Thailand) and mountainous areas of Kamphaeng Phet province (KPP, northern Thailand).

2.2. Sandfly preparation

Collected female sandflies were stored in 95% ethyl alcohol and mounted in Hoyer medium on glass microscopic slides. Morphological identification was based mainly on the keys of Lewis [9,10]. Subsequently, *P. stantoni* and *S. hodgsoni* were photographed using a Nikon DS-Ri1 SIGHT digital camera connected to stereomicroscope Nikon AZ 100 M (Nikon Corp., Tokyo, Japan) with a size scale provided on the picture. A total of 157 right wing pictures from *P. stantoni* and *S. hodgsoni* across different locations were processed for landmark-based GM analysis (Table 1).

2.3. Landmark-based GM analysis

Twelve landmarks were digitized (Fig. 2). When connected after a Procrustes superimposition onto the consensus configuration, they appear as polygons allowing an easier visual comparison of mean wing shape between sandfly species and populations. The Procrustes superposition was conducted according to the Generalized Procrustes Superimposition (GPA) procedure [11,12], generating both size (centroid size [CS]) and shape (partial warps [PW]) variables.

CS is defined as the square root of the sum of the squared distances between the center of the configuration of landmarks and each individual landmark [13]. Size comparisons were performed using a non-parametric permutation test (1000 cycles), and comparisons were illustrated by quantile boxes.



Fig. 1. Map of sandfly collection sites in this study.

The shape variables (partial warps scores [PW]) were processed by standard multivariate analysis to statistically compare groups. The principal components (PCA) of the PW (i.e., the relative warps [RW]) were computed to visualize the morphospace for sandfly species from different locations. The discriminant analysis (DA) used as input variables the RW, or a few first of them according to the sample sizes, and was illustrated by the corresponding factor maps. For these DA, the two localities with very low sample sizes were removed: NTB (6 individuals) and

Table 1
Number of female *Phlebotomus stantoni* and *Sergentomyia hodgsoni* wing pictures used for geometric morphometric analysis.

Species	Locations	Symbols	Area description	Number of wing pictures
P. stantoni	Lang Ga Jiew Island, Chumphon province	LGJ	Limestone swiftlet cave on an isolated island	21
P. stantoni	Nonthaburi province	NTB	Urban area in central Thailand	6
P. stantoni	Kamphaeng Phet province	KPP	Mountainous areas in northern Thailand	17
S. hodgsoni	Ka Island, Chumphon province	KA	Limestone swiftlet cave on an isolated island	7
S. hodgsoni	Lang Ga Jiew Island, Chumphon province	LGJ	Limestone swiftlet cave on an isolated island	57
S. hodgsoni	Mapraw Island, Chumphon province	MAP	Limestone swiftlet cave on an isolated island	13
S. hodgsoni	Kanchanaburi province	KCB	Limestone cave in western Thailand	14
S. hodgsoni	Ratchaburi province	RCB	Limestone cave in central Thailand	22
Total				157

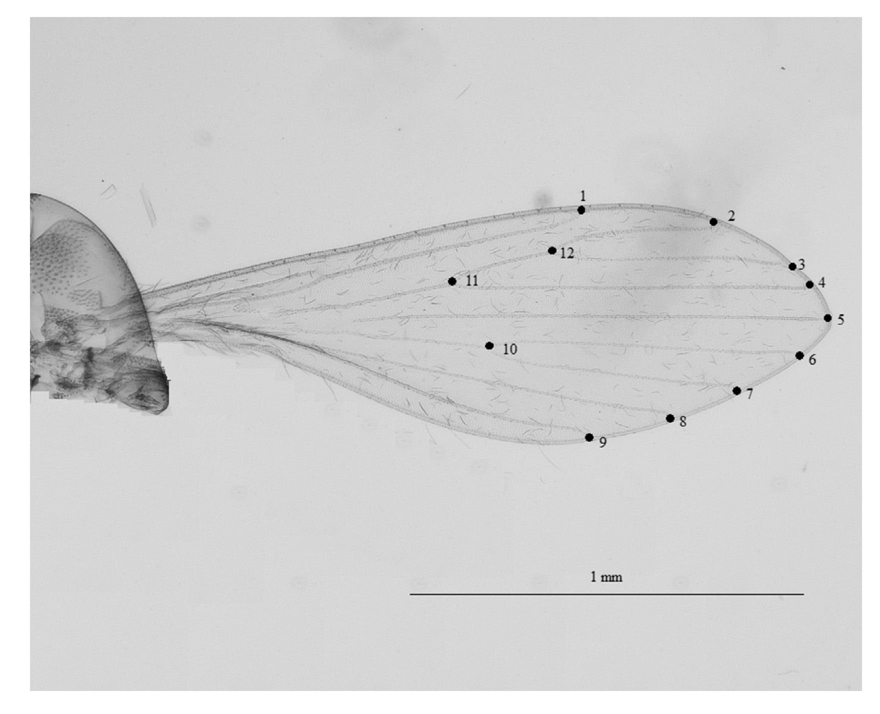


Fig. 2. Position of 12 landmarks digitized for female *Phlebotomus stantoni* and *Sergentomyia hodgsoni*.

KA (7 individuals). Validated reclassification scores were estimated after a DA on the two taxa, after the DA on the geographic populations within each species. In this validated reclassification, each individual was allocated to its closest group (Mahalanobis distance) without being used to help determine a group center [14]. The statistical significance ($P \leq 0.05$) of shape variation was analyzed using non-parametric methods (1000 runs) applied to the pairwise Mahalanobis distances. A neighbor-joining tree was generated based on Procrustes distances between sandflies from different locations.

The allometric effect on the discrimination between collecting sites was explored by regressing the discriminant factors on centroid size and computing the coefficient of determination.

2.4. Software

CLIC version 97 [15,16], freely available at http://mome-clic.com, was used to conduct the digitization of the images and subsequent multivariate analyses on the coordinate data. The following modules were used: COO for landmarks collection, MOG to generate centroid size and shape variables, as well as to compute Procrustes distances and VAR to compare the size between groups. The Procrustes distances were used to compute the neighbor-joining tree using the PHYLIP *neighbor* module [17], and the resulting tree was visualized using the NJPLOT software [18]. The module PAD of CLIC was used to perform discriminant analyzes between groups, as well as to compute Mahalanobis distances and the corresponding statistical significance.

3. Results

3.1. Wing size variation

Mean wing CS comparison of *P. stantoni* and *S. hodgsoni* from different geographical locations (Table 1) showed size variation (Fig. 3, Table 2). Mean wing CS was

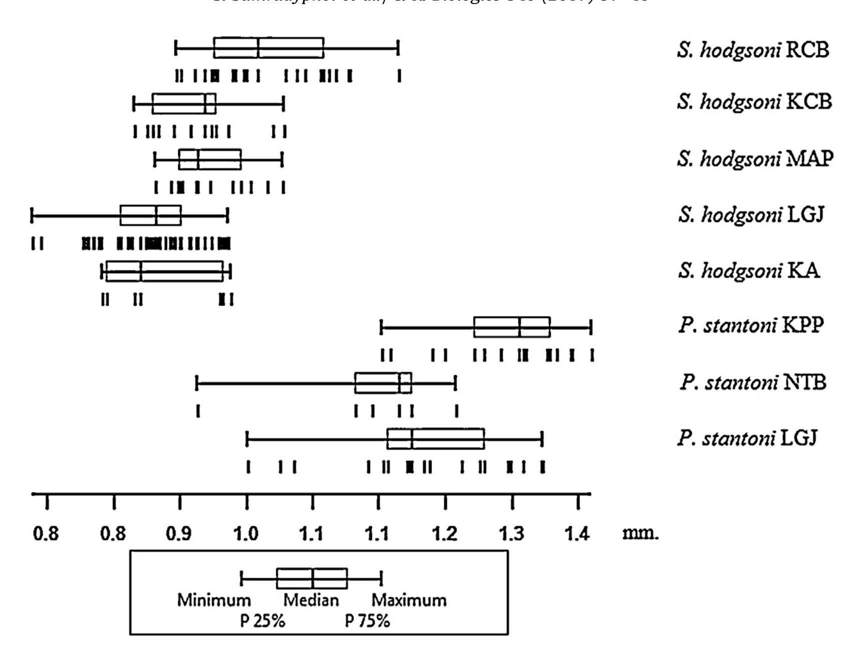


Fig. 3. Variation of the wing centroid size (in mm) of female *Phlebotomus stantoni* and *Sergentomyia hodgsoni* from different localities. Vertical bars represent individuals. P 25%, percentiles 25%, P 75%, percentiles 75%. Boxes are quantile boxes between P 25% and P 75%, with indication of the median position.

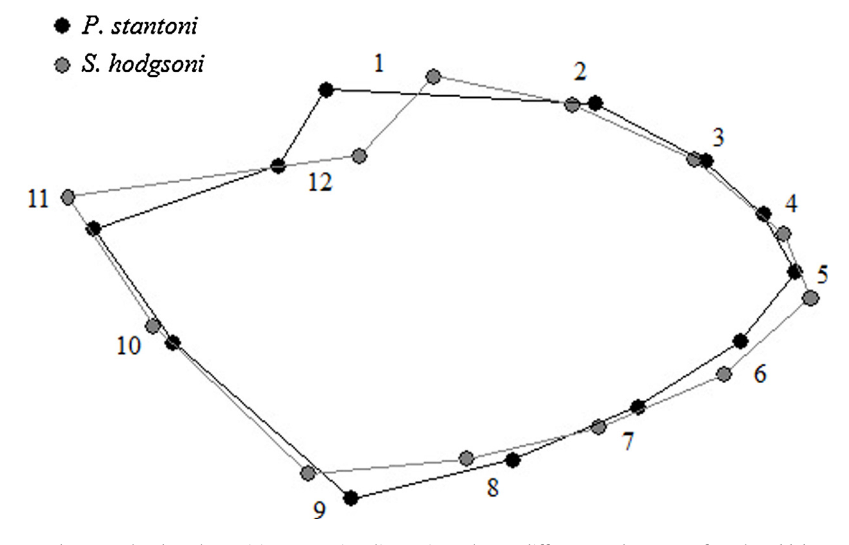


Fig. 4. Polygons as connected mean landmark positions to visualize wing shape differences between female *Phlebotomus stantoni* (black) and *Sergentomyia hodgsoni* (gray) after Procrustes superposition. No amplification applied.

significantly ($P < 0.05$) larger in *P. stantoni* than in *S. hodgsoni* (1.22 mm and 0.91 mm, respectively). *P. stantoni* from mainland in Kamphaeng Phet province had the largest wings (mean, 1.28 mm), significantly different from *P. stantoni* from Lang Ga Jiew Island and an urban location in Nonthaburi province ($P < 0.05$). However, the mean wing CS of *P. stantoni* from caves on Lang Ga Jiew Island and Nonthaburi province were not significantly different ($P > 0.05$). The wing CS of *S. hodgsoni* from a mainland cave in Ratchaburi province was the largest (mean, 1.02 mm), whereas *S. hodgsoni* from Lang Ga Jiew Island had the smallest wing CS (0.89 mm). Almost all populations of *S. hodgsoni* were significantly different ($P < 0.05$) from each other. However, there was no significant ($P > 0.05$) difference of wing size between *S. hodgsoni* from Ka Island and Lang Ga Jiew Island, Ka Island and Kanchanaburi province, or Mapraw Island and Kanchanaburi province.

3.2. Wing shape variation

After superimposition of the mean landmark configurations onto the consensus one, *P. stantoni* and *S. hodgsoni* wing shapes were clearly different (Fig. 4). Polygons of

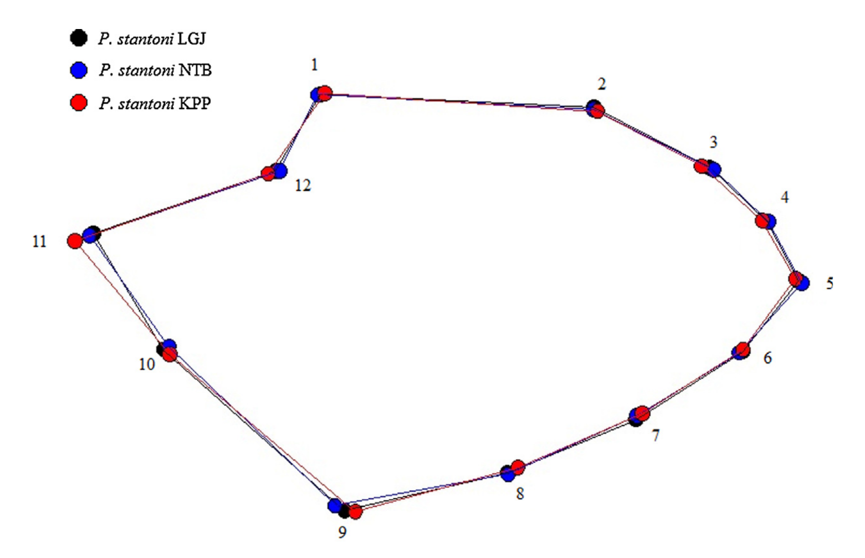


Fig. 5. Polygons as connected mean landmark positions to visualize the wing shape differences in female *Phlebotomus stantoni* from various geographical locations, as obtained after Procrustes superposition. No amplification applied.

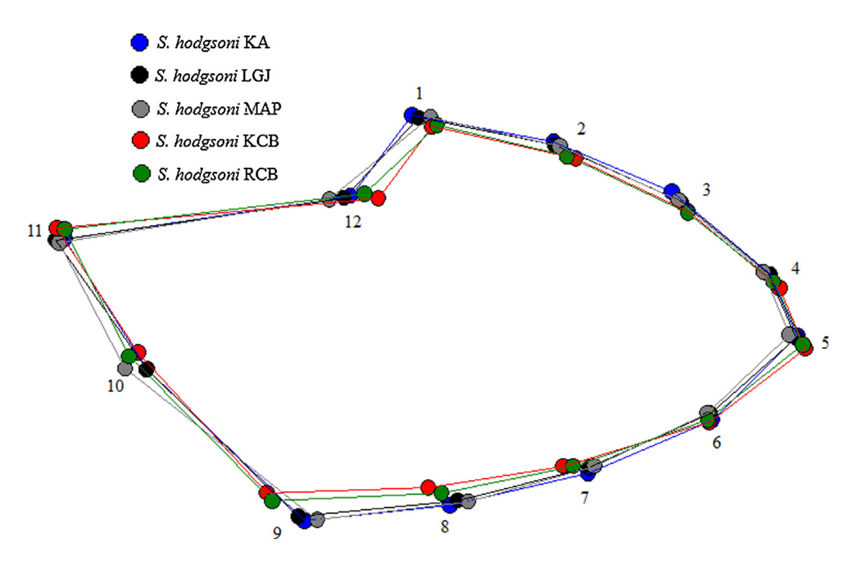


Fig. 6. Polygons as connected mean landmark positions to visualize wing shape differences of female *Sergentomyia hodgsoni* from various geographical locations, as obtained after Procrustes superposition. No amplification applied.

mean wing shape of within species samples are shown in Fig. 5 (*P. stantoni*) and Fig. 6 (*S. hodgsoni*). Consistent intraspecific variation was visible in both sandfly species.

In agreement with the polygon superimpositions, the RW–based morphospace showed no overlapping of wing shapes between *P. stantoni* and *S. hodgsoni*, as well as between some geographic localities within *S. hodgsoni* (Fig. 7). Within each species, significant geographic differences ($P < 0.05$) could be found (Table 3). *P. stantoni* from Lang Ga Jiew Island and Kamphaeng Phet province were significantly different ($P < 0.05$), as were *P. stantoni* from Nonthaburi province and Kamphaeng Phet province ($P < 0.05$).

The factor map of the DA clearly showed the large shape divergence between taxa, as well as some non-overlapping groups within both species: *P. stantoni* was almost completely subdivided into island and mainland samples (Fig. 8), while in *S. hodgsoni* the trend was similar, showing divergence between mainland (KCB, RCB) and island samples (LGJ, MAP), and, within these areas, between sampling sites (KCB versus RCB, and LGJ versus MAP) (Fig. 9). Statistical significance was frequently found, except with localities NTB and KA, represented by only a few individuals (Table 3). For *S. hodgsoni* the contribution of size to shape-based discrimination ranged from 0.099 (with DF1) to 0.165 (with DF2), and for *P. stantoni* (a single DF since two populations were compared), it was 0.117.

The validated reclassification scores (Table 4) confirmed the complete separation of the two taxa, providing an average correct assignment of 79% between two

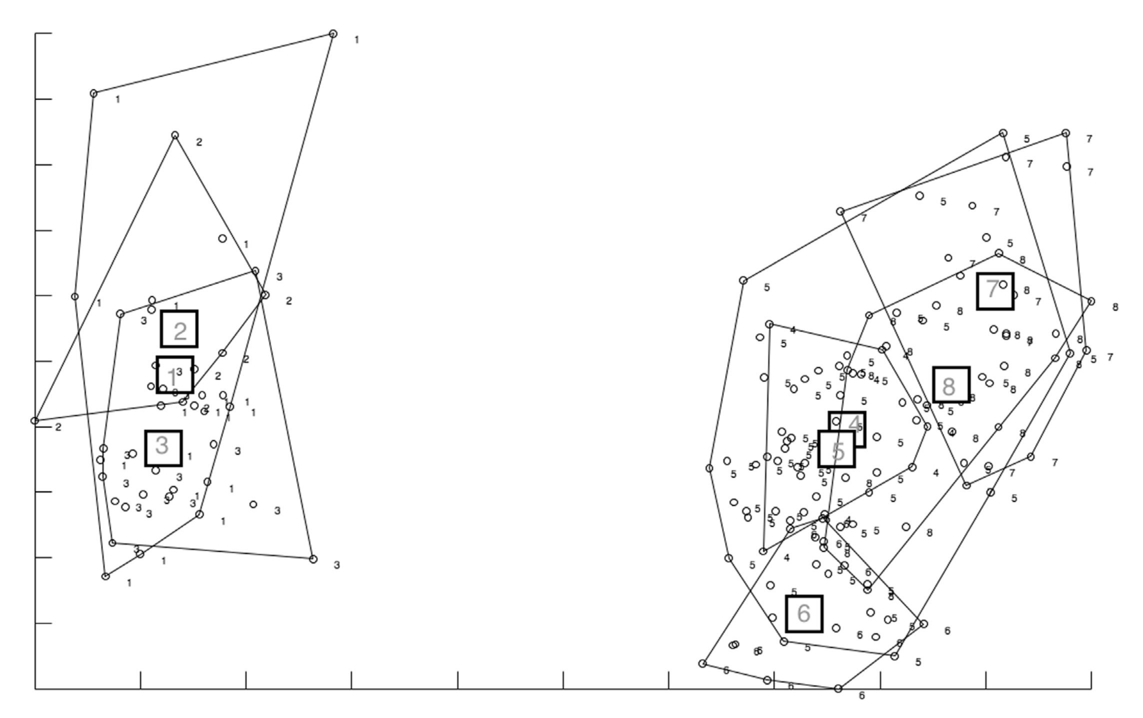


Fig. 7. Wing shape morphospace based on RW variables of female *Phlebotomus stantoni* (1, 2, 3) and *Sergentomyia hodgsoni* (4, 5, 6, 7, 8) samples, represented by convex hulls. The horizontal axis is the first relative warp (RW1), and the vertical axis is the second relative warp (RW2). 1, *P. stantoni* LGJ; 2, *P. stantoni* NTB; 3, *P. stantoni* KPP; 4, *S. hodgsoni* KA; 5, *S. hodgsoni* LGJ; 6, *S. hodgsoni* MAP; 7, *S. hodgsoni* KCB; 8, *S. hodgsoni* RCB.

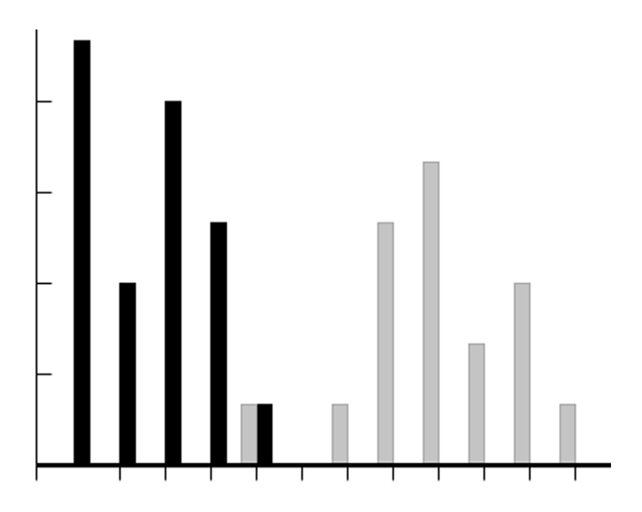


Fig. 8. Factor map of the discriminant factor separating LGJ island (black bars) and KPP northern mainland (grey bars) samples of female *Phlebotomus stantoni*, as derived from shape variables (16 first RW). The NTB sample has been removed from this analysis due to low sample size (6 individuals).

samples in *P. stantoni* (scores ranging from 71 to 88%), and of 65% between four samples in *S. hodgsoni* (scores ranging from 63 to 71%).

Based on Procrustes distances, the neighbor-joining tree first separated the two genera and then, within species, continental and islands locations (Fig. 10).

4. Discussion

This is the first GM study on sandflies from Thailand, here represented by various mainland and island geographic locations of two taxa: *P. stantoni* and *S. hodgsoni*. We selected the simplest and fastest geometric approach, i.e. the landmark-based approach. The wings of sandflies are hairy, which could represent a problem in accurately identifying some landmarks [19]. However, in our samples, manipulating the samples for dissection and mounting was generally enough to clear most of the hairy cover. Our results suggest that with no further changes in the entomological practice of dissecting and mounting sandflies, relevant information was provided with only 12 landmarks. We used the right wing of the specimens disregarding possible asymmetric effects. However, this source of variation has been estimated at a 1 or 2% of the interindividual variation [20], which should not interfere with our comparisons based on one side of the insect.

Size and shape provided taxonomic information of unequal values. The geometry of the wing venation distinguished both taxa without any possible confusion. This was in agreement with the likely high evolutionary divergence between two genera. The same geometric shape could also allow one to distinguish the geographic location within each species. *P. stantoni* from two geographical locations were almost completely distinct. *S. hodgsoni* from mainland and island, as well as within these areas, showed on average diverging geometric shapes, although with some overlapping. Discriminating

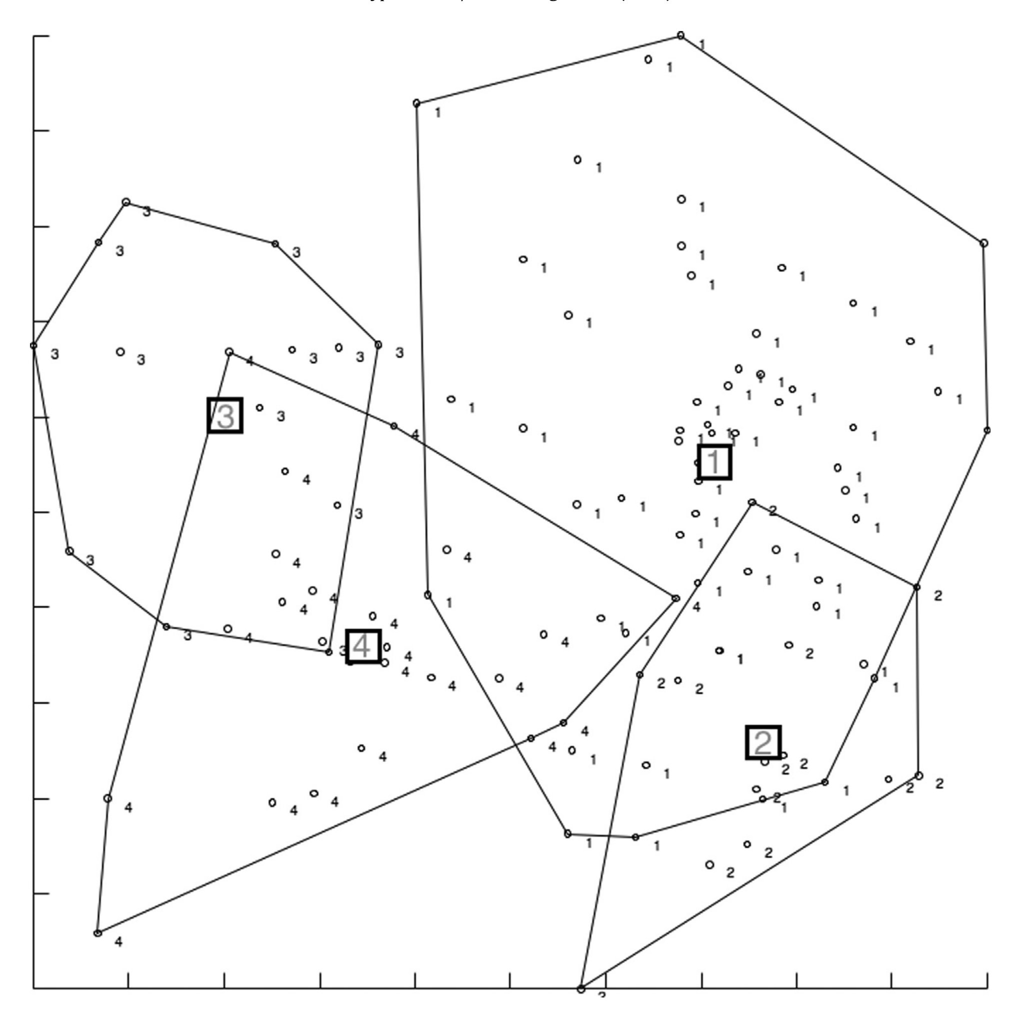


Fig. 9. Factor map of the two first discriminant factors (DF) derived from shape variables of *Sergentomyia hodgsoni* originating from various geographic locations: 1, LGJ island; 2, MAP island; 3, KCB western mainland; 4, RCB central mainland. Each point represents an individual. The horizontal axis is DF1; the vertical axis is DF2. The KA sample has been removed from this analysis due to low sample size (seven individuals).

between geographic localities was weakly under the influence of size variation, suggesting true shape variation.

The shape divergence between intraspecific sites has two possible origins: the environmental effects, or the genetic drift due to geographic isolation. There is a growing consensus claiming that, even if the environmental effect is probably acting in geometric shape differentiation, genetic drift is likely to be the primary force affecting it [21–26]. An argument supporting that hypothesis in our sample is that, in spite of significant and many times non-overlapping difference between geographic locations, there was no interference of this shape variation with the interspecific shape variation. Similar observation was already evidenced in a heterogeneous species sample of neotropical sandflies from various altitudes [27], and have been published for various other arthropods [23–26,28–30].

The size of the wings was computed as a global estimation, the centroid size, allowing one to compare it among samples based on a global, single value. Because wing size indicates specimen size [24], we can infer that *P. stantoni* specimens were generally larger ones than *S. hodgsoni*. More interestingly, in both taxa, specimens from the mainland were significantly larger than those from island populations. Alternatively, it can be said that in both species, northern populations showed larger sizes than southern ones. Such observation has been already made in sandflies: the New World *Lutzomyia ayrozai* and *L. geniculata* showed larger size in higher altitudes [27], the Old World *P. papatasi* also showed size difference in relation to different altitudes in Turkey [31]; and the same species from the northern Atlas Mountains of Morocco was larger than that from the southern Atlas Mountains [32]. This size variation may be related to environmental factors including temperature, host population, and other ecological or climatic effects [32], and appears to be in agreement with the Bergmann's rule [33]. This "rule" suffers some exceptions: for instance in our *P. stantoni* sample from an urban area, the specimens were smaller than those from the northern areas and island areas.

As such, the GM approach provides a powerful characterizing feature, the geometric shape, and represents a low-cost and useful tool to identify species and

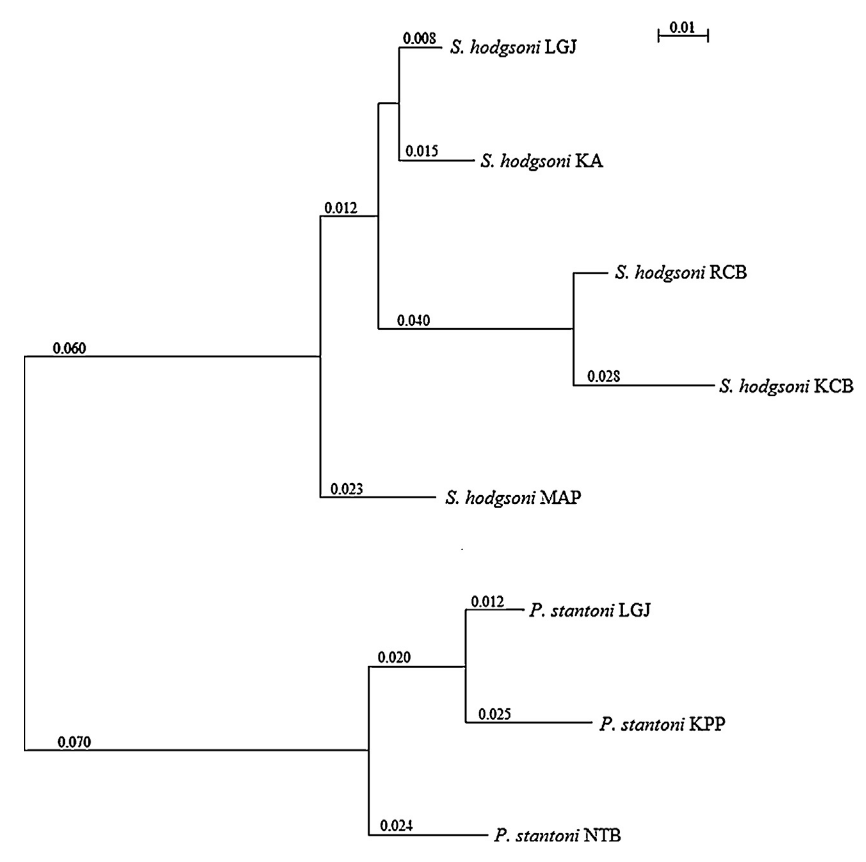


Fig. 10. Neighbor-joining tree based on Procrustes distances, with indication of the patristic distances values, for female *Phlebotomus stantoni* and *Sergentomyia hodgsoni* from different geographical locations.

Table 2
Mean wing centroid size of female *Phlebotomus stantoni* and *Sergentomyia hodgsoni*.

Species	Locations	N	Mean (Min–Max) (mm.)	S.D.	S.E.
P. stantoni	LGJ	21	1.19 (0.99–1.32)	0.09	0.02
P. stantoni	NTB	6	1.12 (0.94–1.23)	0.10	0.04
P. stantoni	KPP	17	1.28 (1.15–1.38)	0.07	0.02
S. hodgsoni	KA	7	0.91 (0.84–0.98)	0.06	0.02
S. hodgsoni	LGJ	57	0.89 (0.76–0.98)	0.05	0.007
S. hodgsoni	MAP	13	0.96 (0.90–1.04)	0.04	0.01
S. hodgsoni	KCB	14	0.94 (0.83–0.93)	0.05	0.01
S. hodgsoni	RCB	22	1.02 (0.92–1.16)	0.07	0.01

Min: minimum; Max: maximum; mm: millimeter; Mean: average centroid size; S.D.: standard deviation; S.E.: standard error. The location symbols correspond to Table 1.

Table 3
Mahalanobis distances between wing shapes of female *Phlebotomus stantoni* and *Sergentomyia hodgsoni*.

P. stantoni				*S. hodgsoni*					
	LGJ	NTB	KPP		KA	LGJ	MAP	KCB	RCB
LGJ	0.00			KA	0.00				
NTB	3.78	0.00		LGJ	2.37	0.00			
KPP	3.73[a]	5.65[a]	0.00	MAP	3.03	2.29[a]	0.00		
				KCB	4.46[a]	4.18[a]	4.91[a]	0.00	
				RCB	4.72[a]	3.67[a]	4.32[a]	3.04[a]	0.00

[a]Indicates statistical significance at $P < 0.05$ after a Bonferroni test. Distances and significance of populations with either NTB (six individuals) or KA (seven individuals) are indicative, and should be confirmed with larger samples.

Table 4
Validated reclassification scores between two species, *Phlebotomus stantoni* and *Sergentomyia hodgsoni*, between LGJ and KPP within *P. stantoni*, and between LGJ, MAP, KCB and RCB within *S. hodgsoni*.

Species	Assigned	Observed	Percent (%)
P. stantoni	38	38	100
S. hodgsoni	106	106	100
P. stantoni			
LGJ	15	21	71
KPP	15	17	88
Total	30	38	79
S. hodgsoni			
LGJ	36	57	63
MAP	9	13	69
KCB	10	14	71
RCB	14	22	64
Total	69	106	65

geographic populations. It could become a routine complement to morphological studies for future epidemiological investigation of leishmaniasis vectors in Thailand.

Disclosure of interest

The authors declare that they have no competing interest.

Acknowledgements

We would like to thank all staffs members of Lang Ga Jiew Island, Chumphon province for sandfly collection.

References

[1] D.J. Lewis, D.G. Young, G.B. Fairchild, D.M. Minter, Proposal for a stable classification of the phlebotomine sandflies (Diptera: Psychodidae), Syst. Entomol. 2 (1977) 319–332.
[2] U. Sharma, S. Singh, Insect vectors of *Leishmania*: distribution, physiology and their control, J. Vector Borne Dis. 45 (2008) 255–272.
[3] C. Apiwathnasorn, S. Sucharit, Y. Rongsriyam, S. Leemingsawat, V. Kerdpibule, T. Deesin, K. Surathin, S. Vutikes, N. Punavuthi, A brief survey of Phlebotomine sandflies in Thailand, Southeast Asian J. Trop. Med. Public Health 20 (1989) 429–432.
[4] C. Apiwathnasorn, S. Sucharit, K. Surathin, T. Deesin, Anthropophilic and zoophilic Phlebotomine sandflies (Diptera, Psychodidae) from Thailand, J. Am. Mosq. Control Assoc. 9 (1993) 135–137.
[5] R. Polseela, C. Apiwathnasorn, Y. Samung, Seasonal variation of cave-dwelling Phlebotomine sandflies (Diptera: Psychodidae) in Phra Phothisat Cave, Saraburi Province, Thailand, Southeast Asian J. Trop. Med. Public Health 38 (2007) 1011–1015.
[6] C. Apiwathnasorn, Y. Samung, S. Prummongkol, A. Phayakaphon, C. Panasopolkul, Cavernicolous species of phlebotomine sandflies from Kanchanaburi Province, with an updated species list for Thailand, Southeast Asian J. Trop. Med. Public Health 42 (2011) 1405–1409.
[7] R. Polseela, A. Vitta, S. Nateeworanart, C. Apiwathnasorn, Distribution of cave dwelling phlebotomine sand flies and their nocturnal and diurnal activity in Phitsanulok Province, Thailand, Southeast Asian J. Trop. Med. Public Health 42 (2011) 1395–1404.
[8] B. Chittsamart, S. Samruayphol, S. Sungvorayothin, R. Pothiwat, Y. Samung, C. Apiwathnasorn, Phlebotomine sand flies of edible-nest swiftlet cave of Lang Ga Jiew Island, Chumphon province, Thailand, Trop. Biomed. 32 (2015) 402–406.
[9] D.J. Lewis, The phlebotomine sandflies (Diptera: Psychodidae) of the oriental region, Bull. Br. Mus. Nat. Hist. Entomol. 37 (1978) 217–343.
[10] D.J. Lewis, A taxonomic review of the genus *Phlebotomus* (Diptera: Psychodidae), Bull. br. Mus. nat. Hist. Entomol. 45 (1982) 121–209.
[11] F.J. Rohlf, Rotational fit (Procrustes) methods, in: F.J. Rohlf, F.L. Bookstein (Eds.), Proceedings of the Michigan Morphometrics Workshop,, University of Michigan Museum of Zoology, 1990, pp. 227–236.
[12] F.J. Rohlf, D.E. Slice, Extensions of de Procrustes method for the optimal superimposition of landmarks, Syst. Zool. 39 (1990) 40–59.
[13] F.L. Bookstein, Morphometric tools for landmark data: geometry and biology, Cambridge University Press, New York, 1991, 435 p.
[14] B.F.J. Manly, Multivariate Statistical Methods: A Primer, Chapman and Hall/CRC Press, Boca Raton, 2004, 224 p.
[15] J.-P. Dujardin, D. Slice, Geometric morphometrics. Contributions to medical Entomology. Chap. 25, in: M. Tibayrenc (Ed.), Encyclopedia of Infectious Diseases. Modern Methodologies, Wiley & Sons, 2007, pp. 435–447.
[16] J.-P. Dujardin, D. Kaba, A.B. Henry, The exchangeability of shape, BMC Res. Notes 3 (2010) 266.
[17] J. Felsenstein, PHYLIP. Phylogeny Inference Package (Version 3.2), Cladistics 5 (1989) 164–166.
[18] G. Perrière, M. Gouy, WWW-Query: an on-line retrieval system for biological sequence banks, Biochimie 78 (1996) 364–369.
[19] A.M. Aytekin, A. Bulent, S.S. Caglar, Y. Ozbel, S. Kaynas, F.M. Simsek, O.E. Kasap, A. Belen, Phenotypic variation among local populations of phlebotomine sand flies (Diptera: Psychodidae) in southern Turkey, J. Vector Ecol. 32 (2007) 226–234.
[20] C.P. Klingenberg, Analyzing fluctuating asymmetry with geometric morphometrics: concepts, methods, and applications, Symmetry 7 (2015) 843–934.
[21] J.-P. Dujardin, Morphometrics applied to Medical Entomology, Infect. Genet. Evol. 8 (2008) 875–890.
[22] J.-P. Dujardin, Modern morphometrics of medically important insects, in: Genetics and Evolution of Infectious diseases, Elsevier Insights Series, Elsevier, Amsterdam, 2011, , pp. 473–501[ISBN 978–0-12–384890–1].
[23] A. Henry, P. Thongsripong, I. Fonseca-Gonzalez, N. Jaramillo-Ocampo, J.-P. Dujardin, The wing shape of dengue vectors from around the world, Infect. Genet. Evol. 10 (2010) 207–214.
[24] D. Kaba, S. Ravel, G. Acapovi-Yao, P. Solano, K. Allou, H. Bosson-Vanga, L. Gardes, E.K. N'Goran, C.J. Schofield, M. Koné, J.-P. Dujardin, Phenetic and genetic structure of tsetse fly populations (*Glossina palpalis palpalis*) in southern Ivory Coast, Parasit. Vectors 5 (2012) 153.
[25] J.-P. Dujardin, S. Kitthawee, Geographic structuring among populations of two *Bactrocera tau* cryptic species (Diptera: Tephritidae) infesting *Momordica cochinchinensis* (Cucurbitaceae), Zoology 116 (2013) 129–138.
[26] A. Perrard, M. Baylac, J.-M. Carpenter, C. Villemant, Evolution of wing shape in hornets: why is the wing venation efficient for species identification? J. Evol. Biol. 27 (2014) 2665–2675.
[27] J.-P. Dujardin, F. Le Pont, M. Baylac, Geographical versus interspecific differentiation of sandflies (Diptera: Psychodidae): a landmark data analysis, Bull. Entomol. Res. 93 (2003) 87–90.
[28] S. Kitthawee, J.-P. Dujardin, The geometric approach to explore the *Bactrocera tau* complex (Diptera: Tephritidae) in Thailand, Zoology 113 (2010) 243–249.
[29] R.E. Godoy, E.A.B. Galati, P. Cordeiroestrela, N.A.D. Souza, T.V. Dos Santos, L.C. De Sousa, E.F. Rangel, Comparative study of the phlebotomine sandfly species (Diptera: Psychodidae: Phlebotominae) of the genera Nyssomyia Barretto, 1962, Bichromomyia Artemiev, 1991, and Migonemyia Galati, 1995, vectors of American cutaneous leishmaniasis in Brazil, Zootaxa 3838 (2014) 501–517.
[30] H.A. Benítez, J. Pizarro-Araya, R. Bravi, M.J. Sanzana, F.M. Alfaro, Morphological variation on isolated populations of *Praocis* (*Praocis*) *spinolai*, J. Insect. Sci. 14 (2014) 11.
[31] A. Belen, B. Alten, A.M. Aytekin, Altitudinal variation in morphometric and molecular characteristics of *Phlebotomus papatasi* populations, Med. Vet. Entomol. 18 (2004) 343–350.
[32] J. Prudhomme, F. Gunay, N. Rahola, F.F. Ouanaimi, S. Guernaoui, A. Boumezzough, A.L. Bañuls, D. Sereno, B. Alten, Wing size and shape variation of *Phlebotomus papatasi* (Diptera: Psychodidae) populations from the south and north slopes of the Atlas Mountains in Morocco, J. Vector Ecol. 37 (2012) 137–147.
[33] K. Bergmann, Über die Verhältnisse der wärmeökonomie der Thiere zu ihrer Grösse, Göttinger Studien 3 (1847) 595–708.

C. R. Biologies 340 (2017) 47–62

Contents lists available at ScienceDirect

Comptes Rendus Biologies

www.sciencedirect.com



Biodiversity/Biodiversité

New case of lateral asymmetry in fishes: A new subfamily, genus and species of deep water clingfishes from Papua New Guinea, western Pacific Ocean☆



Nouveau cas d'asymétrie latérale chez les poissons : une nouvelle sous-famille, genre et espèce de porte-écuelles en eaux profondes de la Papouasie-Nouvelle-Guinée dans l'océan Pacifique ouest

Ronald Fricke [a,*], Jhen-Nien Chen [b], Wei-Jen Chen [b]

[a] *Im Ramstal 76, 97922 Lauda-Königshofen, Germany*
[b] *Institute of Oceanography, National Taiwan University, No. 1 Sec. 4, Roosevelt Road, 10617 Taipei, Taiwan*

ARTICLE INFO

Article history:
Received 10 September 2016
Accepted after revision 10 November 2016
Available online 12 December 2016

Keywords:
Gobiesocidae
Clingfishes
New subfamily
New genus
New species
Papua New Guinea
Molecular phylogeny
PAPUA NIUGINI biodiversity expedition

Mots clés :
Gobiesocidé
Porte-écuelles
Nouvelle sous-famille
Nouveau genre
Nouvelle espèce
Papouasie-Nouvelle-Guinée
Phylogénie moléculaire
Expédition biodiversité PAPUA NIUGINI

ABSTRACT

The unusual clingfish *Protogobiesox asymmetricus* n. gen, n. sp. is described on the basis of four specimens collected in deep water off the north coast of Papua New Guinea in 2012. The species is characterized by its 9–10 dorsal rays, 8 anal rays, 17–24 pectoral-fin rays, 15 principal caudal-fin rays, 3 gills, third arch with 3 gill rakers, 34–35 total vertebrae, with asymmetrical lateral bending starting behind the skull, bent at an angle of 85°–92°; skull asymmetrical in frontal view; skin naked, surface of head and body without striae; disc without adhesive papillae. A new subfamily Protogobiesocinae is described for this species and *Lepadicyathus mendeleevi* Prokofiev, 2005, which is redescribed. The new subfamily is compared within the family; keys to the subfamilies of Gobiesocidae and the species within the new subfamily are presented; its phylogenetic relationship to other gobiesocids is inferred based on a multi-locus DNA dataset.

RÉSUMÉ

Le porte-écuelle insolite *Protogobiesox asymmetricus* n. gen, n. sp. est décrit à partir de quatre spécimens collectés en 2012 dans les eaux profondes au large de la côte nord de la Papouasie-Nouvelle-Guinée. L'espèce se caractérise par sa nageoire dorsale avec 9–10 rayons, sa nageoire anale avec 8 rayons, sa nageoire pectorale avec 17–24 rayons, 15 rayons principaux sur la nageoire caudale, 3 branchies, un troisième arc branchial avec 3 branchiospines, une colonne vertébrale avec un total de 34–35 vertèbres, le corps arrière du crâne présentant une pré-asymétrie latérale et plié à un angle de 85°–92, un crâne asymétrique en vue de face, une peau nue, une surface de tête et un corps sans stries, un disque sans papille adhésive. Une nouvelle sous-famille, les Protogobiesocinae, est décrite pour cette espèce, et *Lepadicyathus mendeleevi* Prokofiev 2005 est décrit à nouveau. La

☆ ZooBank registration: http://zoobank.org/urn:lsid:zoobank.org:pub:F52192A6-C00E-499F-887A-C4C0EEE9AADB.
* Corresponding author.
E-mail address: ronfricke@web.de (R. Fricke).

http://dx.doi.org/10.1016/j.crvi.2016.11.002
1631-0691/

nouvelle sous-famille est comparée aux autres membres de la famille; des clés pour les sous-familles de Gobiesocidae et les espèces incluses dans cette nouvelle sous-famille sont présentées ; sa relation de parenté au sein des gobiesocidés est inférée à partir d'un jeu de données ADN multi-locus.

1. Introduction

The clingfishes of the family Gobiesocidae are predominantly marine fishes distributed worldwide in tropical and temperate seas, with only eight species of the genus *Gobiesox* Lacepède 1800 living in freshwater streams of the tropics. They occur on hard substrata, usually on rocky bottom or in coral reefs, mostly in shallow waters, but some live on the continental or insular shelf down to 337 m (*Kopua nuimata* Hardy 1984 from New Zealand; see Hardy [1]; Hutchins [2]). Clingfishes are small in body size (usually less than 50 mm in total length), characterized by an adhesive disc formed by the pelvic fins, the head depressed, the skin naked, one dorsal and anal fin each, and several specialized osteological characters. The family was revised by Briggs [3], who distinguished 30 genera and 85 species, with some divided in several subspecies. Springer & Fraser [4] examined the osteology of the species in the enigmatic perciform family Cheilobranchidae, and assigned its members (arranged in a single genus *Alabes* Cloquet 1816) to the Gobiesocidae. The following genera and species were described subsequently to the revisions of Briggs [3] and Springer & Fraser [4]: *Lecanogaster*, *L. chrysea* and *Opeatogenys cadenati* by Briggs [5], *Aspasmodes* and *A. briggsi* by Smith [6], *Gobiesox marijeanae* by Briggs [7], *Gobiesox fluviatilis* and *G. mexicanus* by Briggs & Miller [8], *Lepadichthys bolini* by Briggs [9], *Gobiesox lucayanus* by Briggs [10], *Lepadichthys ctenion* and *L. erythraeus* by Briggs & Link [11], *Diplecogaster bimaculata euxinica* by Murgoci [12], *Apletodon knysnaensis* by Smith [13] (synonym of *A. pellegrini* according to Briggs [14]), *Lepadichthys lineatus* by Briggs [15], *Lissonanchus* and *L. lusheri* by Smith [16], *Tomicodon prodomus* by Briggs [17], *Derilissus* and *D. nanus* by Briggs [18], *Lepadichthys caritus* by Briggs [19], *Arcos decoris*, *Rimicola brevis* and *Tomicodon bidens* by Briggs [20], *Tomicodon rhabdotus* by Smith-Vaniz [21], *Gymnoscyphus* and *G. ascitus* by Böhlke & Robins [22], *Derilissus kremnobates* and *D. vittiger* by Fraser [23], *Derilissus altifrons* by Smith-Vaniz [24], *Discotrema* and *D. crinophilum* by Briggs [25] as *D. crinophila*), *Modicus*, *M. minimus* and *M. tangaroa* by Hardy [26], *Cochleoceps bassensis* by Hutchins [27], *Propherallodus*, *P. briggsi*, *Pherallodichthys* and *P. meshimaensis* by Shiogaki & Dotsu [28], *Kopua* and *K. nuimata* by Hardy [29], *Aspasmogaster occidentalis* by Hutchins [30], *Tomicodon abuelorum* by Szelistowski [31], *Kopua kuiteri* by Hutchins [2], *Cochleoceps viridis*, *C. bicolor* and *C. orientalis* by Hutchins [32], *Posidonichthys* and *P. hutchinsi* by Briggs [33], *Gobiesox juniperoserrai* by Espinosa et al. [34], *Apletodon incognitus* by Hofrichter & Patzner [35], *Lepadichthys springeri* by Briggs [36], *Tomicodon reitzae* by Briggs [37], *Rimicola cabrilloi* by Briggs [38], *Tomicodon briggsi*, *T. clarkei*, *T. cryptus*, *T. lavettsmithi* and *T. leurodiscus* by Williams & Tyler [39], *Alabes elongata*, *A. gibbosa*, *A. obtusirostris*, *A. occidentalis* and *A. scotti* by Hutchins & Morrison [40], *Acyrtus pauciradiatus* by Sampaio et al. [41], *Lepadicyathus* and *L. mendeleevi* by Prokofiev [42], *Alabes bathys* and *A. springeri* by Hutchins [43], *Apletodon wirtzi* by Fricke [44], *Discotrema monogrammum* and *D. zonatum* by Craig & Randall [45], *Briggsia* and *B. hastingsi* by Craig & Randall [46], *Apletodon barbatus* by Fricke et al. [47], *Aspasmichthys alorensis* and *Lepadichthys akiko* by Allen & Erdmann [48], *Kopua japonica* by Moore et al. [49], *Derilissus lombardii* by Sparks & Gruber [50], *Acyrtus lanthanum* by Conway et al. [51], *Unguitrema* and *U. nigrum* by Fricke [52], *Diplecogaster tonstricula* by Fricke et al. [53], *Kopua vermiculata* by Shinohara & Katayama [54], and *Lepadichthys bilineatus* by Craig, Bogorodsky & Randall in Craig et al. [55].

At present, 166 species belonging to 48 genera of gobiesocids are recognized; they are currently classified into nine subfamilies (Briggs [3]; Conway et al. [56]): Aspasminae Briggs 1955, Cheilobranchinae Günther 1870, Chorisochisminae Briggs 1955, Diademichtyinae Whitley 1950, Diplocrepinae Briggs 1955, Gobiesocinae Bleeker 1859, Haplocyclicinae Briggs 1955, Lepadogastrinae Canestrini 1871–1872, Trachelochisminae Briggs 1955. A list of a generic classification within these subfamilies was provided by Conway et al. [56].

During the PAPUA NIUGINI Biodiversity Expedition in 2012, specimens of an unusual, laterally asymmetrical clingfish were collected in deep water off the north-eastern coast of Papua New Guinea. They were compared with the other known gobiesocid species and other taxa in gobiesocid-related fish families, and were found to represent an undescribed subfamily, genus and species of gobiesocid fishes, which is described in the present paper. In addition, the genus *Lepadicyathus* Prokofiev 2005, which is currently classified in the Aspasminae, is revised; the only known species, *Lepadicyathus mendeleevi* Prokofiev 2005, is redescribed.

2. Methods and materials

Our descriptive methods follow Briggs [3] and Fricke et al. [57]. Sex determination based on the presence or the absence of urogenital papillae is confirmed by internal examination (gonads). The abbreviation "SL" refers to the standard length (measured from the tip of the snout to the middle of the caudal fin base), "TL" to the total length (measured from the tip of the snout to the end of the caudal fin). The adhesive disc is divided into three different areas: region A is the anterior portion, region B is the posterior one, and region C is the centre of the disc (as illustrated by Briggs [3]). In the description of new taxa, data of the

holotype are given first, followed by data of the paratypes in parentheses. Fin rays are counted using the method of Fricke (1983), where spines are expressed as Roman numerals, unbranched soft rays are expressed as lower-case Roman numerals, and branched rays as Arabic numerals. Authors and dates of family-group taxa follow Laan et al. [58]. The updated key to subfamilies of Gobiesocidae is based on Briggs [3]. To elucidate the relationships of the unusual clingfish discovered in this study and to assign it to its proper higher hierarchic taxonomic rank, its multi-locus DNA sequences were generated and compared to those obtained from the representative taxa in the Gobiesocidae and other gobiesocid-related families determined by previous studies investigating acanthomorph phylogeny (Chen et al. [59,60]; Dettaï & Lecointre [61]; Near et al. [62]). The list of taxa used for the molecular analysis in this study was provided in Table 1. The collection of new molecular data was carried out by the following procedures. Small pieces of muscle or fin tissue were excised from the specimens, preserved in 95% ethanol, and stored at −20 °C in the Marine Biodiversity and Phylogenomics Laboratory at the Institute of Oceanography, National Taiwan University (NTU), Taipei. Genomic DNA was extracted using an automated DNA-extractor 199 (LabTurbo 48 Compact System with LGD 480–220 kits: Taigene 200 Bioscience Corporation, Taipei) following the manufacturer's 201 protocol. The polymerase chain reaction (PCR) was used to amplify the following targeting gene fragments: recombination activating gene 1 (RAG1), rhodopsin (RH), early growth response 2B (EGR2B), cytochrome oxidase subunit I (COI), 12S and 16S ribosomal RNAs (12S and 16S). The first three are encoded in the nuclear genome and the remaining three are part of the mitochondrial genome.

Table 1
Taxa, genes, and Genbank accession numbers for the gene sequences of representative species.

Taxon	Tissue ID	Voucher	GenBank accession no.					
			RAG1	Rhodopsin	EGR2B	COI	12S	16S
Pleuronectidae[a]								
Hippoglossus stenolepis Schmidt 1904	WJC148	NA	KF311999	KF312141	KF312079	AM749128	AM749128	AM749128
Carangidae[a]								
Parastromateus niger (Bloch 1795)	WJC11	NA	EF095654	EF095616	KC442131	KC442079	EF095562	EF095590
Embiotocidae								
Ditrema temminckii Bleeker 1853	WJC171	NA	KY126055	KY126046	KY126033	AP009129	AP009129	AP009129
Mugilidae								
Liza aurata (Risso 1810)	WJC18	NA	KF017112	KF017144	KF017049	JQ060457	EU715447	GQ252691
Pomacentridae								
Dascyllus aruanus (Linnaeus 1758)	WJC377	NA	EF095674	EF095632	KY126034	KJ968020	AF081228	AF119402
Cichlidae								
Astronotus ocellatus (Agassiz 1831)	WJC168	NA	EF095671	EF095629	JN231060	KC442077	EF095575	EF095603
Ambassidae								
Parambassis wolffii (Bleeker 1850)	WJC49	NA	EF095647	EF095612	KY126035	EF095558	EF095586	
Bedotiidae								
Bedotia geayi Pellegrin 1907	WJC399	NA	EF095640	AY141267	KC442117	AY290799	AY141339	AY141409
Adrianichthyidae								
Oryzias latipes (Temminck & Schlegel 1846)	NA	NA	EF095641	AB001606		AP004421	EF095555	EF095583
Clinidae								
Heterostichus rostratus Girard 1854	WJC118	SIO 01-179	HQ168866	HQ168988	KY126036	HQ168631	HQ158801	AY822076
Labrisomidae								
Labrisomus nuchipinnis (Quoy & Gaimard 1824)	WJC86	NA	KY126056	KY126047	KY126037	KF930015	AY098808	AY098848
Gobiesocidae								
Aspasminae								
Aspasma minima (Döderlein 1887)				EU637943		NC_008130	NC_008130	NC_008130
Cheilobranchinae								
Alabes hoesei Springer & Fraser 1976	WJC5173	I.45630-050	KY126057		KY126038	KY126065	KY126072	KY126080
Alabes scotti Hutchins & Morrison 2004	WJC5174	I.46305-001	KY126058	KY126048	KY126039	KY126066	KY126073	KY126081
Diademichthyinae								
Lepadichthys lineatus Briggs 1966	WJC5008	14-1309 Dili	KY126059	KY126049	KY126040	KY126067	KY126074	KY126082
Gobiesocinae								
Acyrtus lanthanum Conway, Baldwin & White 2014	WJC5006	01-033-Arsp	KY126060	KY126050	KY126041	KY126068	KY126075	KY126083
Gobiesox strumosus Cope 1870	WJC65	NA	KY126061	KY126051	KY126042	KY126069	KY126076	KY126084
Acyrtops beryllinus (Hildebrand & Ginsburg 1927)	WJC82	NA	KY126062	KY126052	KY126043	KY126070	KY126077	KY126085
Tomicodon humeralis (Gilbert 1890)		SIO 02-1-1	HQ168876	HQ169001		HQ168639		
Lepadogastrinae								
Apletodon dentatus (Facciolà 1887)	WJC305	NA	KY126063	KY126053	KY126044	KJ616456	KY126078	KY126086
Lepadogaster lepadogaster (Bonnaterre 1788)				AY141273		KF369136	AY141347	AY141417
Protogobiesocinae								
Protogobiesox asymmetricus n. sp.	PNG1169	NTUM10633	KY126064	KY126054	KY126045	KY126071	KY126079	KY126087

[a] Outgroups used for rooting the inferred phylogenetic tree.

Table 2
Primers used in this study.

Locus/Primer[a]		Primer sequences (5′-3′)	Source
RGA1	R1 2533F	CTGAGCTGCAGTCAGTACCATAAGATGT	López *et al.*, 2004
	R1 4078R	*TGAGCCTCCATGAACTTCTGAAGRTAYTT*	López *et al.*, 2004
	R1 4061R	*AATACTTGGAGGTGTAGAGCCAGT*	Chen *et al.*, 2007
	R1 4090R	*CTGAGTCCTTGTGAGCTTCCATRAAYTT*	López *et al.*, 2004
EGR2B	E2B 252F	CGCAACCAGACTTTCACCTAY	Chen *et al.*, 2013
	E2B 261F	TTCACCTAYATGGGNAAGTTCTCMAT	Chen *et al.*, 2013
	E2B 270F	ATGGGRAAGTTCTCCATCGAC	Chen *et al.*, 2013
	E2B 278F	AGTTTTCCATCGACTCSCAGTA	Chen *et al.*, 2008
	E2B 287F	TTGACTCSCAGTATCCAGGTAAC	Chen *et al.*, 2008
	E2B 1078R	*AATTTGCGNCCGCAGSAGTC*	Chen *et al.*, 2013
	E2B 1078R-bis	*GAACTTACGNCCGCAGAARTC*	Chen *et al.*, 2013
	E2B 1108R	*TTTTGTGTGTCTCTTTCTYTCGTC*	Chen *et al.*, 2008
	E2B 1112R	*ATTTTNGTGTGTCGYTTYCTC*	Chen *et al.*, 2013
	E2B 1117R	*AGGTGGATTTTGGTGTGTCTYTT*	Chen *et al.*, 2008
	E2B 1121R	*CCTCAGGTGGATTTTAGTGTGTC*	Chen *et al.*, 2013
Rhosopsin	RH 1F	ATGAACGGCACAGARGGAC	Chen *et al.*, 2003
	RH 193F	CNTATGAATAYCCTCAGTACTACC	Chen *et al.*
	RH 1039R	*TGCTTGTTCATGCAGATGTAGA*	Chen *et al.*
COI	CoxI_FishF1	TCAACCAACCACAAAGACATTGGCAC	Ward *et al.*, 2005
	CoxI_FishF2	TCGACTAATCATAAAGATATCGGCAC	Ward *et al.*, 2005
	CoxI_FishR1	*TAGACTTCTGGGTGGCCAAAGAATCA*	Ward *et al.*, 2005
	CoxI_FishR2	*ACTTCAGGGTGACCGAAGAATCAGAA*	Ward *et al.*, 2005
12S	L1090	AAAGCACGGCACTGAAGATGC	Palumbi *et al.*, 1991
	H1478	*TTTCATGTTTCCTTGCGGTAC*	Palumbi *et al.*, 1991
16S	arL	CGCCTGTTTAACAAAAACAT	Palumbi *et al.*, 1991
	brH	*CCGGTCTGAACTCAGATCAGT*	Palumbi *et al.*, 1991

RAG1, recombination activation gene 1; EGR2B: early growth response protein gene 2B; COI: mitochondrial cytochrome oxidase subunit 1; 12S, 16S, mitochondrial ribosomal RNA; R = A or G, Y = C or T, S = C or G.
[a] Reverse primers in italics

These genes were selected for their ability to provide sound phylogenetic information for inter- and intra-familiar relationships in several previous phylogenetic studies focusing on the percomorph fishes (e.g., Chen et al. [60]; Lo et al. [63]). Primer sequences in this study are listed in Table 2. Temperature cycling profiles for amplification consisted of an initial denaturation stage (95 °C, 5 min) followed by 35 cycles, each with a denaturation step (95 °C, 40 s), an annealing step (53 °C for RAG1 and EGR2B; 55 °C for the other genes, 40 s) and an elongation step (72 °C, 90 s for RAG1 and 60 s for the other genes), before a final extension stage (72 °C, 7 min). PCR products were purified using the AMPure magnetic bead clean-up protocol (Agencourt Bioscience Corp., USA). Purified PCR products were sequenced by Sanger sequencing using dye-labelled terminators. Sequence determinations from Sanger reaction products were generated on ABI 3730 analyzers (Applied Biosystems, USA) at Genomics BioSci & Tech (Taipei) and at the Center of Biotechnology (National Taiwan University). For each locus and specimen, the chromatograms of the sequences were checked and edited manually using the program CodonCode Aligner 3.7.2.2 (Codoncode Corporation, Dedham, MA, USA). Chromatograms were examined for evidence of sequencing artefacts or problematic base calls. Verified complementary chromatograms were then assembled to build consensus sequences. All sequences from the orthologous gene were aligned using the automatic multiple-alignment program Muscle (Edgar [64]). The resulting multiple sequence alignments were adjusted by eye using the inferred amino acid translation as a guide for inferred gap placement in protein coding genes and the loop/stem structure of 12S and 16S ribosomal RNAs to identify loop regions where site homology was difficult to ascertain with confidence. Alignments were edited using Se-Al v2.0a11 (Rambaut [65]). Short regions of the alignments from EGR2B, 12S and 16S in which homology assessment is uncertain were excluded from the further steps of phylogenetic analysis. Phylogenetic analysis was conducted based on the combined data matrix complied from the aligned DNA sequences from the six genes with a partitioned maximum likelihood (ML) method as implemented in the parallel version of RAxML 7.4.2 (Stamatakis [66]). A mixed-model analysis was used that allows the independent estimation of individual models of nucleotide substitution for each partition. Three partitions (by codon) were assigned for cytochrome *b* and rhodopsin. Fourteen partitions (by gene and by codon position of protein coding gene) were assigned. Because RAxML only provides GTR-related (Yang [67]) models of rate heterogeneity for nucleotide data (Stamatakis [66]), the nucleotide substitution model GTR + Γ+I was employed for the analysis. Optimal ML tree search was conducted with 100 separate runs using the default algorithm of the program for each run and the final tree with the best ML score was selected among the 100 ML trees of these runs. Finally, nodal support was assessed with bootstrapping (BS) (Felsenstein [68]) with the maximum likelihood (ML) criterion, based on 500 pseudo-replicates. The inferred phylogenetic tree was rooted by two non-"Ovalentaria" taxa: *Hippoglossus stenolepis* (Pleuronectidae) and *Parastromateus niger* (Carangidae). The specimens cited in the present paper

are deposited in the following collections: AMS, The Australian Museum, Sydney, Australia; MNHN, ''Muséum national d'histoire naturelle'', Paris, France; NTUM, National Taiwan University Museums, Taipei, Taiwan; ZIN, Laboratory of Ichthyology, Zoological Institute, Russian Academy of Sciences, St. Petersburg, Russia. The abbreviations of repositories of additional materials follow Fricke & Eschmeyer [69].

2.1. Comparative material for morphological examination

Acyrtops amplicirrus: CAS-SU 18101 (2 paratypes), St. Thomas, Virgin Islands. *Acyrtus artius*: CAS-SU 23254 (holotype), Curaçao, Netherlands West Indies; CAS-SU 47942 (1 paratype), Curaçao, Netherlands West Indies. *Alabes dorsalis*: SMNS 1694 (4), Murray River estuary, South Australia; SMNS 21395 (1), Cape Dromedary, New South Wales, Australia. *Apletodon barbatus*: SMNS 26427 (holotype), São Tiago Island, Cape Verde Islands; MNHN 2009-1592 (1 paratype), same data as the holotype; SMNS 24604 (1), Sal Island, Cape Verde Islands; SMNS 24605 (1), Sal Island, Cape Verde Islands; SMNS 26428 (19 paratypes), same data as the holotype; USNM 396967 (1 paratype), same data as the holotype. *A. dentatus*: CCML uncat. (2), Alegranza Island, Canary Islands; CCML uncat. (2), Lanzarote Island, Canary Islands; SMNS 12664 (1), Genoa, Italy. *A. incognitus*: NMW 93029 (holotype), Banyuls-sur-Mer, France; CCML uncat. (2), Gran Canaria, Canary Islands; CCML uncat. (1), La Graciosa, Canary Islands; SMNS 21814 (1), Faial, Azores Islands. *A. pellegrini*: SAIAB 10255 (1), Knysna, South Africa; SAIAB 10852 (11), Knysna, South Africa; SAIAB 14599 (7), South Africa; SAIAB 43756 (5), False Bay, South Africa; USNM 198169 (1 paratype), Knysna, South Africa; USNM 270272 (1), Algoa Bay, South Africa. *A. wirtzi*: SMNS 24130 (holotype), Bombom Island, São Tomé and Principe; MNHN 2005-0170 (1 paratype), same data as the holotype; SMNS 24446 (5 paratypes), same data as the holotype; SMNS 24132 (2 paratypes), same data as the holotype; SMNS 25472 (5), Limbe, Cameroon; USNM 381374 (1 paratype), same data as the holotype. *Arcos nudus*: SMNS 11301 (4), Rio San Juan, Dominican Republic; SMNS 11401 (12), Rio Baonico, Dominican Republic; SMNS 11408 (3), Rio Nazaito, Dominican Republic. *Aspasma minima*: NMW 76995 (2 syntypes), Sagami Bay, Japan. *Aspasmichthys ciconiae*: CAS-SU 7136 (1 syntype), Inland Sea, Japan; USNM 50760 (1 syntype), Inland Sea, Japan. *Aspasmogaster costata*: SMNS 14754 (9), Red Head, New South Wales, Australia. *Chorisochismus dentex*: USNM 119223 (1), Algoa Bay, South Africa. *Cochleoceps spatula*: SMNS 12519 (1), Cervantes Island, Western Australia. *Conidens laticephalus*: SMNS 24701 (10), Northeast Cape, Taiwan. *C. samoensis*: SMNS 21982 (1), Province Sud, Grande Terre, New Caledonia; SMNS 22836 (3), Province Sud, Grande Terre, New Caledonia. *Creocele cardinalis*: SMNS 14806 (1), Tasmania, Australia. *Dellichthys morelandi*: SMNS 13754 (5), North Island, New Zealand; SMNS 13762 (1), North Island, New Zealand; SMNS 13780 (4), North Island, New Zealand; SMNS 13827 (1), North Island, New Zealand; SMNS 14142 (4), North Island, New Zealand. *Derilissus altifrons*: ANSP 112690 (holotype), Dominica. *D. vittiger*: ANSP 109626 (holotype), Venezuela. *Diademichthys lineatus*: SMNS 18156 (2), Fiji, Viti Levu; SMNS 21975 (3), New Caledonia, Récif Goëland; SMNS 21977 (1), New Caledonia, Nouméa; SMNS 21979 (2), New Caledonia, Baie Maá; SMNS 21980 (2), New Caledonia, Bancs Nord; SMNS 22995 (1), New Caledonia, Baie de Pritzbue; SMNS 23522 (1), New Caledonia, Nouméa; SMNS 23997 (1), New Caledonia, Nouméa; SMNS 25414 (1), New Caledonia, Nouméa; SMNS 26545 (1), New Caledonia, Baie de Goro. *Diplecogaster bimaculata*: HUJ 20577 (7), Balearic Islands, S Mallorca; HUJ 20593 (1), Balearic Islands, NE Mallorca; HUJ 20602 (2), Balearic Islands, NW Mallorca; HUJ 20623 (1), Balearic Islands, SSE Mallorca; SMNS 12541 (1), Pyrenées Orientales, France; SMNS 13177 (1), Giglio Island, Italy; SMNS 14049 (2), Giglio Island, Italy; SMNS 19061 (2), Karavas Alsavcak Bay, Northern Cyprus; SMNS 19204 (2), Giglio Island, Italy; SMNS 20163 (8), Caniço de Baixo, Madeira; SMNS 20347 (1), Tabarca, Tunisia; SMNS 21202 (2), Porto Novo, Madeira. *D. ctenocrypta*: ZMUC P9037 (holotype), Gran Canaria, Canary Islands. *D. pectoralis*: SMNS 11916 (4), Faial Island, Azores Islands. *D. tonstricula*: ZSM 40089 (holotype), Dakar, Senegal; CCML uncat. (2 paratypes), Fuerteventura, Canary Islands; ZSM uncat. (5 paratypes), Dakar, Senegal. *Diplocrepis puniceus*: SMNS 10012 (2), North Island, New Zealand; SMNS 13755 (2), North Island, New Zealand; SMNS 13769 (1), North Island, New Zealand; SMNS 13782 (1), North Island, New Zealand; SMNS 13828 (8), North Island, New Zealand; SMNS 13832 (4), North Island, New Zealand; SMNS 13922 (42), South Island, New Zealand; SMNS 13936 (32), South Island, New Zealand; SMNS 13945 (24), South Island, New Zealand; SMNS 14003 (1), South Island, New Zealand; SMNS 14043 (1), South Island, New Zealand; SMNS 14069 (1), South Island, New Zealand. *Discotrema crinophilum*: SMNS 16677 (1), Philippines, Balicasag Island; SMNS 16678 (1), Philippines, Balicasag Island; SMNS 17896 (1), Society Islands, Moorea (**new record**); SMNS 21981 (1), New Caledonia, Nouméa. *D. monogrammum*: BPBM 39040 (holotype), Papua New Guinea, New Britain; BPBM 36504 (2), Indonesia, Flores. *D. zonatum*: BPBM 38972 (holotype), Fiji, Charybdis Reef. *Gastrocyathus gracilis*: SMNS 10011 (1), North Island, New Zealand; SMNS 14124 (1), North Island, New Zealand. *Gastroscyphus hectoris*: SMNS 13763 (1), North Island, New Zealand; SMNS 13770 (1), North Island, New Zealand; SMNS 13829 (3), North Island, New Zealand; SMNS 13834 (27), North Island, New Zealand; SMNS 13854 (1), North Island, New Zealand; SMNS 13862 (1), North Island, New Zealand; SMNS 13923 (26), South Island, New Zealand; SMNS 13924 (76), South Island, New Zealand; SMNS 13938 (6), South Island, New Zealand; SMNS 13947(9), South Island, New Zealand; SMNS 13948 (17), South Island, New Zealand; SMNS 13949 (30), South Island, New Zealand; SMNS 14008 (5), South Island, New Zealand; SMNS 14018 (1), South Island, New Zealand. *Gobiesox strumosus*: SMNS 13612 (1), Rio de Janeiro, Brazil. *Gouania willdenowi*: SMNS 421 (4), Hvar Island, Croatia; SMNS 576 (2), Hvar Island, Croatia; SMNS 13175 (1), Giglio Island, Italy; SMNS 13573 (1), Costa Brava, Spain; SMNS 13574 (1), Crete Island, Greece; SMNS 16808 (6), Sicily, Italy; SMNS 22064 (6), Cres Island, Croatia. *Gymnoscyphus ascitus*: ANSP 113587 (holotype), St. Vincent. *Haplocylix littoreus*: CAS-SU

47678 (2), North Island, New Zealand. *Kopua nuimata*: SMNS 10013 (1), North Island, New Zealand; SMNS 13737 (6), North Island, New Zealand; SMNS 13781 (1), North Island, New Zealand; SMNS 13826 (22), North Island, New Zealand; SMNS 13833 (2), North Island, New Zealand; SMNS 13943 (4), South Island, New Zealand; SMNS 13996 (20), South Island, New Zealand; SMNS 14030 (1), South Island, New Zealand; SMNS 14042 (2), Stewart Island, New Zealand; SMNS 14070 (1), South Island, New Zealand; SMNS 14127 (1), South Island, New Zealand; SMNS 14151 (2), South Island, New Zealand. *Lecanogaster chrysea*: BMNH 1958.7.3.1 (holotype), Lingo, Ghana. *Lepadichthys caritus*: BPBM 34140 (1), Indonesia, Flores. *L. coccinotaenia*: BPBM 21711 (1), South Africa, KwaZulu-Natal. *L. erythraeus*: SMNS 22550 (1), Red Sea, Gulf of Aqaba, Egypt, 14 km north of Nuweiba. *L. frenatus*: SMNS 21978 (1), New Caledonia, off Nouméa. *L. lineatus*: SMNS 22573 (4), Red Sea, Gulf of Aqaba, Egypt, 14 km north of Nuweiba. *L. minor*: SMNS 15130 (1), Fiji, Viti Levu; SMNS 17822 (2), Cook Islands, Aitutaki; SMNS 20909 (2), La Réunion, Les Filaos; SMNS 21020 (2), La Réunion, Les Filaos; SMNS 21161 (1), La Réunion, Les Filaos; SMNS 21178 (2), La Réunion, Saint-Leu; SMNS 22980 (1), Loyalty Islands, Lifou; SMNS 26966 (3), New Caledonia, Nouméa. *Lepadichthys* sp.: SMNS 21976 (1), New Caledonia, Baie Maá; SMNS 23962 (15), New Caledonia, Ile Nou; SMNS 26967 (4), New Caledonia, Nouméa; SMNS 26968 (1), New Caledonia, Nouméa. *Lepadogaster candolii*: SMNS 579 (1), Hvar Island, Croatia; SMNS 993 (1), Trieste, Italy; SMNS 2662 (6), Naples, Italy; SMNS 8996 (1), Senj, Croatia; SMNS 9416 (1), Cres Island, Croatia; SMNS 13176 (1), Giglio Island, Italy; SMNS 13575 (5), Saronic Gulf, Greece; SMNS 13576 (1), Elba Island, Italy; SMNS 13677 (1), Peloponnes, Greece; SMNS 13578 (3), Crete Island, Greece; SMNS 13579 (3), Muros, Galicia, Spain; SMNS 13580 (1), Saronic Gulf, Greece; SMNS 13581 (1), Costa Brava, Spain; SMNS 13582 (2), Elba Island, Italy; SMNS 13613 (1), Biograd, Croatia; SMNS 13614 (1), Sicily, Italy; SMNS 13615 (1), Sicily, Italy; SMNS 13616 (2), Corfu Island, Greece; SMNS 13620 (2), Corfu Island, Greece; SMNS 14700 (6), Reis Magos, Madeira; SMNS 14721 (2), Cres Island, Croatia; SMNS 16020 (1), Caniçal, Madeira; SMNS 16069 (1), Siciliy, Italy; SMNS 25479 (2), Caniço de Baixo, Madeira. *L. lepadogaster*: SMNS 1079 (1), Azores; SMNS 13556 (1), Biograd, Croatia; SMNS 13557 (1), Golfo di Trieste, Italy; SMNS 13558 (1), Bari, Italy; SMNS 13559 (1), Karlobag, Croatia; SMNS 13560 (2), Corfu Island, Greece; SMNS 13561 (5), Elba Island, Italy; SMNS 13562 (1), Collioure, Pyrenées-Orientales, France; SMNS 13563 (1), Crete Island, Greece; SMNS 13564 (1), Cap Negro, N Tétouan, Morocco; SMNS 13565 (2), Elba Island, Italy; SMNS 13566 (2), Sea of Marmara, Turkey; SMNS 13567 (1), İstanbul Province, Turkey, Black Sea; SMNS 13568 (1), Granada Province, Spain; SMNS 13569 (1), Banyuls-sur-Mer, France; SMNS 13570 (2), Gran Canaria, Canary Islands; SMNS 13617 (5), Costa Brava, Spain; SMNS 13618 (1), Corfu Island, Greece; SMNS 14699 (4), Reis Magos, Madeira; SMNS 16726 (6), Fuerteventura, Canary Islands; SMNS 19070 (1), Karavaş Alsavçak Bay, Northern Cyprus; SMNS 22609 (8), La Palma, Canary Islands; SMNS 25316 (1), Bodrum, Turkey; SMNS 25481 (2), Caniço de Baixo, Madeira. *L. purpurea*: SMNS 10295 (1), Lanzarote, Canary Islands; SMNS 12549 (1), Collioure, France; SMNS 13571 (1), Biograd, Croatia; SMNS 13572 (2), Saronic Gulf, Greece; SMNS 15286 (2), Cap Béar, Pyrenées Orientales, France; SMNS 15315 (2), La Palma, Canary Islands; SMNS 15328 (1), La Palma, Canary Islands; SMNS 16727 (4), Fuerteventura, Canary Islands; SMNS 16766 (2), Fuerteventura, Canary Islands; SMNS 22610 (4), La Palma, Canary Islands; SMNS 22623 (1), La Palma, Canary Islands; SMNS 23501 (5), El Hierro, Canary Islands. *Liobranchia stria*: USNM 149910 (holotype), Saipan, Marianas Islands. *Modicus minimus*: BMNH 1982.6.17.55 (1 paratype), North Island, New Zealand. *Opeatogenys cadenati*: MNHN 1959-0059 (holotype), Senegal; MNHN 1959-0060 (2 paratypes), Senegal. *Parvicrepis parvipinnis*: AMS I.7708 (5 syntypes), Sydney, New South Wales, Australia. *Pherallodichthys meshimaensis*: NSMT-P 46752 (holotype), Kyushu, Japan. *Pherallodiscus funebris*: CAS-SU 20 (9 paralectotypes), Gulf of California, Mexico. *Pherallodus indicus*: CAS-SU 47683 (1), Raroia, Tuamotu Archipelago. *P. smithi*: CAS-SU 31349 (holotype), KwaZulu-Natal, South Africa. *Posidonichthys hutchinsi*: AMS I.17615-002 (holotype), Fiddler's Bay, South Australia. *Propherallodus briggsi*: NSMT-P 46749 (holotype), Kyushu, Japan. *Rimicola muscarum*: CAS-SU 3030 (holotype), Monterey Bay, California, USA. *Sicyases sanguineus*: SMNS 390 (2), Chile. *Tomicodon humeralis*: CAS-SU 70 (5 syntypes), Gulf of California, Mexico. *Trachelochismus melobesia*: SMNS 13926 (1), South Island, New Zealand; SMNS 13940 (1), South Island, New Zealand. *T. pinnulatus*: SMNS 13925 (1), South Island, New Zealand; SMNS 13937 (1), South Island, New Zealand; SMNS 13939 (2), South Island, New Zealand; SMNS 13946 (4), South Island, New Zealand; SMNS 13950 (6), South Island, New Zealand; SMNS 13951 (34), South Island, New Zealand. *Unguitrema nigrum*: NTUM 10603 (holotype), Madang, Papua New Guinea; MNHN uncat. (1 paratype), same data as the holotype.

3. Results

3.1. Gobiesocid phylogeny

The combined dataset for inferring gobiesocid phylogeny contains the sequences of *RAG1* gene (1476 bp), *Rhodopsin* gene (819 bp), *EGR2B* gene (855 bp), *COI* gene (633 bp), *12S* gene (344 bp) and *16S* gene (334 bp) from a total of 22 examined taxa that include 11 gobiesocid representatives from five out of their nine currently recognized subfamilies (Table 1). The total of 4461 nucleotides comprise 2184 variable sites (49%) and 736 parsimony-informative sites. The resulting ML tree is shown in Fig. 1.

From the inferred tree, the monophyly of the Gobiesocidae as well as its subfamilies Gobiesocinae and Cheilobranchinae is confirmed with 100% bootstrap nodal support. The Lepadogastrinae is monophyletic, but it received only week support. Among the outgroup taxa, the blennioids are the most closely related to the Gobiesocidae and their sister-group relationship is supported by a strong bootstrap value of 99%. Within the family, our result divides the gobiesocid taxa sampled in

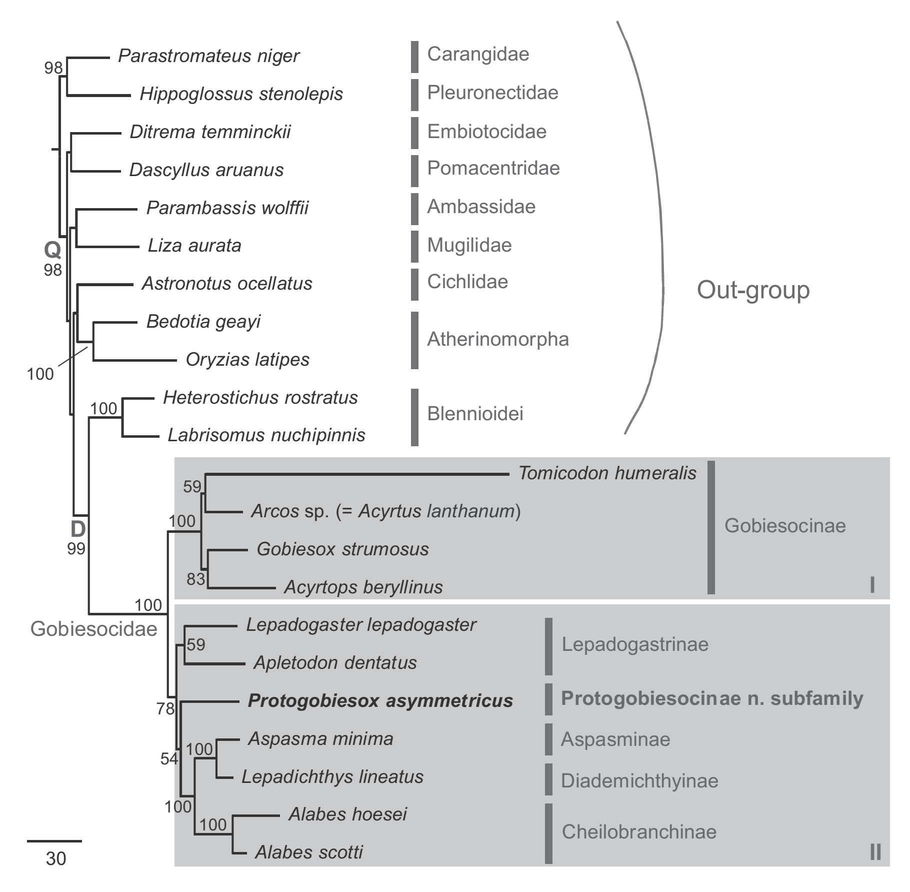


Fig. 1. Phylogenetic tree of the Gobiesocidae inferred by the partitioned maximum-likelihood method with the GTR + Γ+*I* nucleotide substitution model based on the combined dataset. Branch lengths are proportional to the inferred nucleotide substitutions. Numbers at nodes represent bootstrap values in percentage. Values below 50% are not shown. An undetermined specimen of *Arcos* sp. was further determined to represent a recently described species, *Acyrtus lanthanum* Conway, Baldwin & White 2014 by *COI* sequence similarity.

this study into two sub-groups (I and II), one containing the taxa from the Gobiesocinae and the other with the remaining gobiesocids in four subfamilies plus the newly discovered clingfish from deep water off the north coast of Papua New Guinea (see the description below) (Fig. 1). According to our phylogenetic result, we can induce that the new taxon is a gobiesocid of sub-group II, and it appears to be an independent gobiesocid lineage or subfamily as it is not tightly clustered with any known subfamilies of the Gobiesocidae, at least sampled in this study (Fig. 1).

3.2. *Protogobiesocinae new subfamily (Figs. 2–6)*

3.2.1. *Type genus*

Protogobiesox n. gen.

3.2.2. *Diagnosis*

A subfamily of gobiesocid fishes with a partial lateral asymmetry; head slightly asymmetrical when seen from the front; vertebral column laterally bent, at an angle of 40–92°; anus situated on the right-hand side of the body in males, and on the left-hand side in females; position of guts slightly asymmetrical to strongly asymmetrical; gills 3; pelvic fin disc rudimentary, in two parts, at most with a few rudimentary papillae basally in region B. Pelvic bones present, pelvic fin forming a double disc; scapula, pectoral radial and rays present; total vertebrae 33–35.

3.2.3. *Description*

Dorsal-fin rays ix–xii; anal-fin rays viii–x; pectoral-fin rays xvii–xxiv; caudal-fin rays (iv-v),x-xv,(iv-v). Gills 3; gill rakers on 3rd arch 0–3.

Head lateral line system with 2 pores in the nasal canal, 1–2 pores in the postorbital canal, 0–2 pores in the lacrimal canal, 0–2 pores in the preopercular canal, and 0–2 pores in the mandibular canal. Vertebrae 33–35 (15 + 18–20). Pleural ribs 12–13 pairs.

Head broad, depressed. Head and skull at least slightly asymmetrical in frontal view. Gill membranes attached to isthmus. Pelvic bones present. Body bent to the left-hand side (males) or right-hand side (females); vertebral column bent at angle of 40–92°, bending starts between skull and level of anus. Anus situated on right-hand side of the body (males) or the left-hand side of the body (females); male with a short urogenital papilla. Skin naked; surface of head and body may bear striae.

Dorsal fin origin on the left-hand side of the body (males), and on the right-hand side (females); anal fin origin on the right-hand side of the body (males) or the

left-hand side of the body (females). Dorsal and anal-fin bases attached to caudal-fin base by membranes. Pelvic fin forming a double disc; scapula, pectoral radial and rays present. Disc membrane inserting at the base of the 12th–16th pectoral-fin ray. Disc rudimentary, incomplete, completely or mostly without adhesive papillae.

3.2.4. Etymology

The name of the new subfamily is based on the type genus, *Protogobiesox*; its meaning is "ancestral gobiesocid," referring to the pelvic fins resembling the putative ancestral form of gobiesocids.

3.2.5. Distribution

The two described species are distributed off the north coast of the main island of Papua New Guinea, western Pacific Ocean (Fig. 7).

3.2.6. Comparisons

Within the family Gobiesocidae, this subfamily is unique in its lateral asymmetry. It further differs from the subfamily Cheilobranchinae in the presence of pelvic bones and a disc (pelvic bones and disc greatly reduced or absent in Cheilobranchinae), the presence of a scapula, pectoral radials and pectoral-fin rays (all these absent in the Cheilobranchinae, and the total vertebrae number 33–35 (60–78 in Cheilobranchinae), and from the other subfamilies in the presence of three gills (three and one half in the Chorisochisminae, Haplocyclicinae, Lepadogastrinae, Trachelochisminae), the gill membranes which are attached to the isthmus (free from isthmus in Diplocrepinae, Gobiesocinae, Haplocyclicinae, Trachelochisminae), the double disc (disc single in Chorisochisminae, Diademichthyinae, Gobiesocinae, Haplocyclicinae), and the disc region B lacking papillae or with very few rudimental papillae in 1–2 rows (with 6–10 rows of flattened papillae in the Aspasminae). A key to the subfamilies of the Gobiesocinae is presented below, as well as a key to the species of the Protogobiesocinae n. subfam.

3.2.7. Key to the subfamilies of the family Gobiesocidae

1a. Pelvic bones present, pelvic fin forming a single or double disc; scapula, pectoral radial and rays present; total vertebrae 25–54	2
1b. Pelvic bones and pelvic fin greatly reduced or absent; scapula, pectoral radial and rays absent; total vertebrae 60–78	Cheilobranchinae
2a. Gills three and one-half	3
2b. Gills three	6
3a. Gill membranes free from isthmus	4
3b. Gill membranes attached to isthmus	5
4a. Disc double (Indo-Pacific to Japan)	Trachelochisminae
4b. Disc single (New Zealand)	Haplocyclicinae
5a. Disc double (Eastern Atlantic and South Africa)	Lepadogastrinae
5b. Disc single (South Africa)	Chorisochisminae
6a. Gill membranes free from isthmus	7
6b. Gill membranes attached to isthmus	8
7a. Disc double (South Africa to Indo-Pacific; New Zealand)	Diplocrepinae
7b. Disc single (America plus South Africa)	Gobiesocinae
8a. Disc double (Indo-Pacific)	9
8b. Disc single (South Africa to Indo-Pacific)	Diademichthyinae
9a. Body laterally symmetrical, vertebral column not bent; disc region B with 6–10 rows of flattened papillae (Indo-Pacific)	Aspasminae
9b. Body laterally asymmetrical, vertebral column bent at an angle of 40–92°; disc region B lacking papillae or with very few rudimental papillae in 1–2 rows (Western Pacific)	Protogobiesocinae n. subfam

3.2.8. Key to the species of the subfamily Protogobiesocinae n. subfam

1a. Dorsal fin with 9–10 rays; anal fin with 8 rays; caudal fin with 15 principal rays; vertebral column strongly bent at an angle of 85–92°; bending starts behind skull; skin naked, without striae	*Protogobiesox asymmetricus* n. gen., n. sp.
1b. Dorsal fin with 11–12 rays; anal fin with 10 rays; caudal fin with 10 principal rays; vertebral column bent at an angle of 40–45°; bending starts just before level of anus; skin naked, with numerous, closely set, oblique striae consisting of minute tubercles	*Lepadicyathus mendeleevi*

3.3. Protogobiesox *new genus* (*Figs. 2–5*)

3.3.1. Type species

Protogobiesox asymmetricus n. gen., n. sp.

3.3.2. Diagnosis

A genus of protogobiesocine fishes with a partial lateral asymmetry; head slightly asymmetrical when seen from the front; vertebral column strongly bent towards the left in males, towards the right in females, at an angle of 85–92°; bending starts behind the skull; anus situated on the right-hand side of the body in males, on the left-hand side in females; position of guts strongly asymmetrical; gills 3; pelvic fin disc rudimentary, in two parts, without adhesive papillae. Dorsal fin with 9–10 rays; anal fin with 8 rays; caudal fin with 15 principal rays. Skin naked, without striae.

3.3.3. Description

Dorsal-fin rays x (ix–x); anal-fin rays viii (viii); pectoral-fin rays xxiv (xvii–xxiv); caudal-fin rays (v),xv,(iv) [(iv–v),xv,(iv)]. Gills 3 (3); gill rakers on 3rd arch 3 (3).

Detailed description see below under *Protogobiesox asymmetricus* n. gen. n. sp.

3.3.4. Etymology

The name of the new genus means "ancestral gobiesocid;" it refers to the pelvic fins resembling the putative ancestral form of gobiesocids. The gender is masculine.

3.3.5. Remarks

This genus is monotypic, with *Protogobiesox asymmetricus* n. gen., n. sp. as the only known species.

3.4. *Protogobiesox asymmetricus n. sp. (Figs. 2–5)*

Asymmetrical deep-water clingfish.

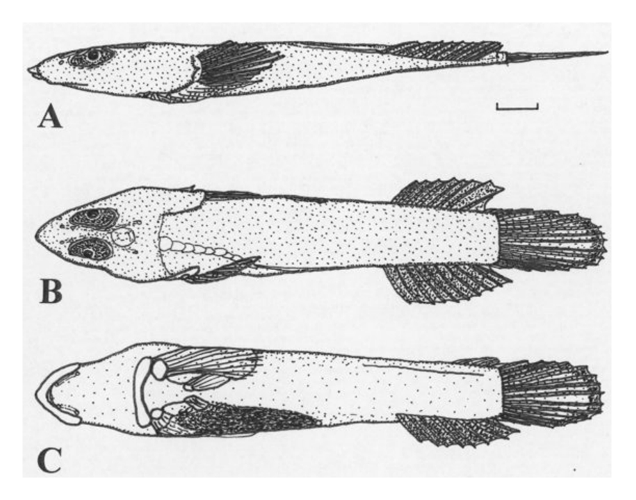


Fig. 2. *Protogobiesox asymmetricus* gen. nov., sp. nov., NTUM 10628, holotype, male, 60.0 mm SL, Papua New Guinea, Madang Province, northeast of Taviltae. **A** (upper) Lateral view; **B** (centre) dorsal view; **C** (lower) ventral view. Bar: 5 mm.

3.4.1. Type material

Holotype. NTUM 10628, male, 60.0 mm SL, Papua New Guinea, Madang Province, northeast of Taviltae, 4°31'S 145°31'E, 380-382 m depth, St. CP4035, sunken logs, some covered with sponges, W.-J. Chen, R/V Alis, 17 Dec. 2012.

Paratypes. Four specimens: MNHN 2016-03333, 1 female, 59.0 mm SL, same data as the holotype; NTUM 10633, 1 male, 53.6 mm SL, same data as holotype; NTUM 10629, 1 male, 56.0 mm SL, Papua New Guinea, Sandaun Province, northwest of Aitape, 3°01'S 142°16'E, 400–560 m in depth, St. CP4056, sand bottom with sunken logs, W.-J. Chen, R/V Alis, 20 Dec. 2012; NTUM 10674, 1 male, 51.8 mm SL, Papua New Guinea, West Sepik Province, 13.5 km northwest of Aitape, 3°03'S 142°18'E, 370–374 m depth, St. CP 4055, Wei-Jen Chen, R/V Alis, 20 Dec. 2012.

3.4.2. Diagnosis

Dorsal fin with 9–10 rays, anal fin with 8 rays, pectoral fin with 17–24 rays, principal caudal-fin rays 15, three gills, third arch with 3 gill rakers. Vertebral column with a total of 34–35 vertebrae, with asymmetrical lateral bending starting behind the skull, bent at an angle of 85°–92°. Skull asymmetrical in frontal view. Skin naked, surface of head and body without striae. Disc without adhesive papillae; posterior margin may be partially fringed; region B small, left- and right-hand sides separate, larger on the right-hand side than on left-hand side.

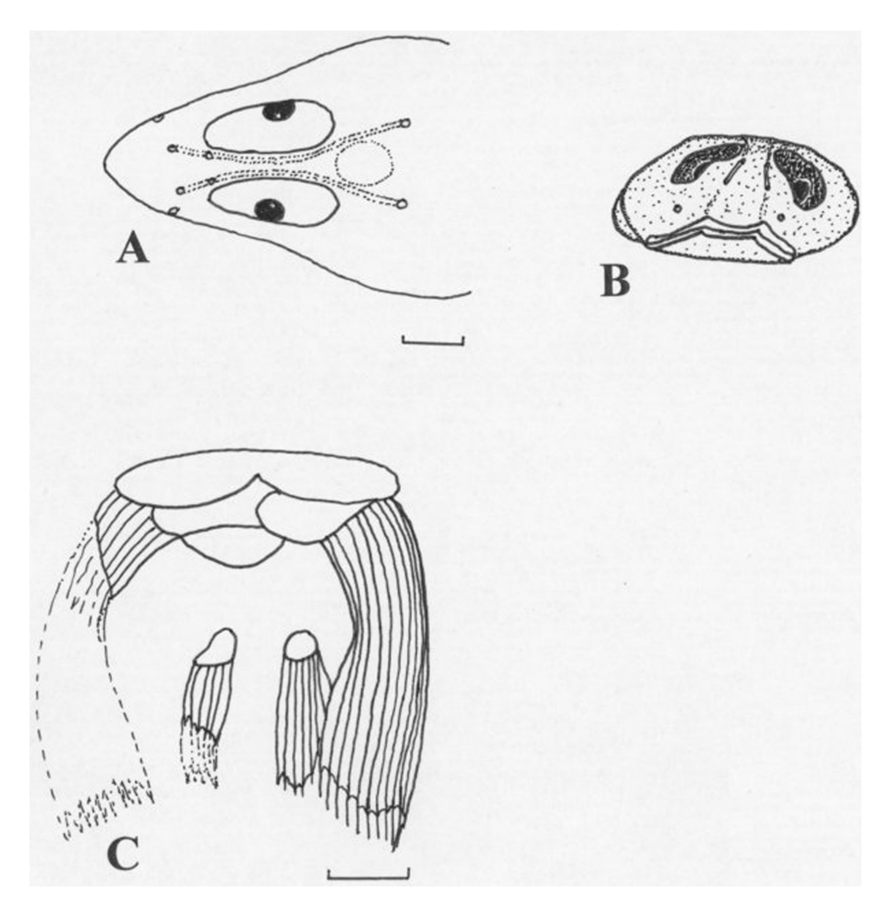


Fig. 3. *Protogobiesox asymmetricus* gen. nov., sp. nov., NTUM 10628, holotype, male, 60.0 mm SL, Papua New Guinea, Madang Province, northeast of Taviltae. **A** (upper left) Head, dorsal view, indicating lateral line canals and pores. **B** (upper right) head, frontal view, showing skull, eye and snout asymmetry. **C** (lower) pelvic fin disc. Bars: 3 mm.



Fig. 4. *Protogobiesox asymmetricus* gen. nov., sp. nov., NTUM 10628, holotype, male, 60.0 mm SL, Papua New Guinea, Madang Province, northeast of Taviltae. Photograph immediately after collection. Vertebral column bent towards the left-hand side.

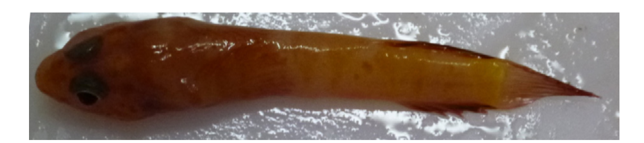


Fig. 5. *Protogobiesox asymmetricus* gen. nov., sp. nov., MNHN XXXX-XXXX, paratype, female, 59.0 mm SL, Papua New Guinea, Madang Province, northeast of Taviltae. Photograph immediately after collection. Vertebral column bent towards the right-hand side.

3.4.3. Description

Dorsal-fin rays x (ix–x); anal-fin rays viii (viii); pectoral-fin rays xxiv (xvii–xxiv); caudal-fin rays (v),xv,(iv) [(iv–v),xv,(iv)]. Gills 3 (3); gill rakers on 3rd arch 3 (3). Measurements of the holotype and paratypes, see Table 3.

Both upper and lower jaws with several series of undifferentiated conical teeth, no canines or incisors.

Head lateral line system with 2 pores in the nasal canal, 1 pore in the postorbital canal, lacrimal and preopercular canals missing, and 2 pores in the mandibular canal (Figs. 2 and 3).

Vertebrae 35 (34–35) [15 + 20 (15 + 19–20)]; asymmetrical bending of the vertebral column starting from the 1st (1st) vertebra. Pleural ribs 13 (13) pairs.

Head broad, depressed. Head and skull asymmetrical in frontal view (Fig. 3B). Head length 34.5 (32.0–33.6)% SL (2.9–3.1 in SL). Maximum body depth 10.7 (8.5–11.8)% SL (8.5–11.8 in SL). Maximum body width 19.2 (18.3–23.5)% SL (4.2–5.4 in SL). Maximum (horizontal) orbit diameter 8.8 (9.1–12.2)% SL (2.6–3.9 in head length). Snout relatively long, pointed (Fig. 3A). Preorbital length 7.3 (4.0–7.3)% SL (4.5–7.9 in head length). Interorbital distance narrow, 2.3 (1.1–2.7)% SL (12.3–30.0 in head length). Upper jaw length 13.5 (9.3–13.0)% SL. Lower jaw length 10.7 (7.9–12.4)% SL. Gill membranes attached to isthmus. Body bent to the left-hand side (males) or right-hand side (females); vertebral column bent at angle of 87° (85–92°), bending starts behind skull. Anus situated on the right-hand side of the body (male) or the left-hand side of the body (female); closer to anal-fin origin than the disc; male with a short urogenital papilla, its length 0.5 (0.4–0.5)% of SL (62–90 in

Table 3
Counts and measurements of the holotype and paratypes of *Protogrammus asymmetricus* n. gen. n. sp.

	Holotype NTUM 10628 Male	Paratype NTUM 10674 Male	Paratype NTUM 10629 Male	Paratype NTUM 10633 Male	Paratype MNHN 2016-03333 Female
Standard length	60.0	51.8	56.0	53.6	59.0
Head length	20.7	16.6	18.5	18.0	19.3
Body depth	6.4	4.4	5.4	6.3	6.0
Body width	11.5	9.5	10.8	12.6	11.4
Orbit diameter	5.3	6.3	5.1	4.9	5.8
Preorbital length	4.4	2.1	4.1	3.9	4.1
Interorbital distance	1.4	0.7	1.5	0.6	0.9
Upper jaw length	8.1	4.8	7.3	6.7	7.7
Lower jaw length	6.4	4.1	6.0	5.5	7.3
Preanus length	36.7	32.9	33.3	31.5	35.9
Urogenital papilla	0.3	0.2	0.3	0.2	–
PC length	5.3	5.5	4.6	4.7	6.1
PC depth	6.5	4.6	5.2	4.9	6.0
PC width	1.4	1.6	1.1	2.0	1.4
Predorsal length	43.9	35.9	42.1	38.4	42.4
Preanal length	45.6	40.0	41.4	40.4	46.2
Distance disc to anus	14.6	?	10.4	10.9	9.9
Distance anus to anal-fin origin	9.2	8.1	7.1	7.7	6.9
Prepectoral length	20.6	17.0	20.7	20.7	22.0
Predisc length	13.2	11.0	12.4	11.9	14.2
1st dorsal ray	5.3	3.2	5.1	4.8	4.1
Last dorsal ray	6.0	5.5	4.0	4.6	5.3
Dorsal-fin base	14.6	7.9	11.0	8.9	12.2
1st anal ray	4.5	2.5	3.9	2.7	2.9
Last but one anal ray	6.5	3.1	5.8	4.3	4.6
Last anal ray	5.1	2.4	4.7	3.9	4.1
Anal-fin base length	9.5	6.8	9.5	8.3	9.5
Pectoral-fin length	10.4	9.7	10.7	9.8	10.6
Pectoral-fin base	3.6	3.6	3.9	3.9	4.3
Disc length	16.0	?	11.4	11.0	13.9
Caudal-fin length	12.8	10.6	11.4	10.2	12.4

mm: measurements; PC: Caudal peduncle.

head length); distance between disc and anus 24.3 (16.8–20.3)% SL, distance between anus and anal-fin origin 15.3 (11.7–15.6)% SL. Pre-anus length 61.2 (58.8–63.5)% SL (1.6–1.7 in SL). Sides of body with an elongate dermal fold on left-hand side below the anal-fin base. Caudal-peduncle length 8.8 (8.2–10.6)% SL (9.4–12.2 in SL). Caudal-peduncle depth 10.8 (8.9–10.2)% SL (9.2–11.3 in SL). Caudal-peduncle width 2.3 (2.0–3.7)% SL (26.8–50.9 in SL). Skin naked; surface of head and body without striae.

Predorsal-fin length 73.2 (69.3–75.2)% SL (1.3–1.4 in SL). Pre-anal-fin length 76.0 (77.2–78.3)% SL (1.3–1.4 in SL). Dorsal fin origin on the left-hand side of the body (male), on the right-hand side of the body (female); anal fin origin on the right-hand side of the body (male), on the left-hand side of the body (female). Dorsal and anal-fin bases attached to caudal-fin base by membranes. Pre-pectoral-fin length 34.3 (32.8–38.6)% SL (2.6–3.0 in SL). Predisc length 22.0 (21.2–24.1)% SL (4.2–4.7 in SL). Disc length 26.7 (20.4–23.6)% SL (3.8–4.9 in SL). Disc membrane inserting at the base of the 13th (13th) pectoral-fin ray. Disc rudimentary, incomplete, with left- and right-hand parts of regions A and B separate, without adhesive papillae; fin-ray branches at distal margins with short filaments; region B small (Fig. 3C). Caudal-fin length 21.4 (19.0-21.0) % SL (4.7-5.2 in SL).

Colour in life (Figs. 4 and 5). Head and body brown, with an irregular, slightly darker banding, anteriorly reddish, posteriorly yellowish; eyes dark grey. Pectoral-fin rays reddish, caudal fin rose; dorsal and anal-fin rays rose, membranes blackish.

Colour in alcohol. Head and body uniformly yellowish brown, lower sides of head and body pale; eyes dark grey; occiput transparent, brain visible, yellowish white; peritoneum black. Dorsal and anal fins and distal margin of caudal fin dark grey.

3.4.4. Distribution

North coast of Papua New Guinea (Madang Province; Sandaun Province) (Fig. 7). This new species was collected at depths of 381–480 m.

3.4.5. Etymology

The name of the new species, *asymmetricus*, refers to the unusual asymmetry of head and body.

3.4.6. Comparisons

This new species is distinguished from the related species *Lepadicyathus mendeleevi* by its 9–10 dorsal-fin rays (11–12 in *L. mendeleevi*), the 8 anal-fin rays (10 in *L. mendeleevi*), 15 principal caudal-fin rays (10 in *L. mendeleevi*), the vertebral column strongly bent at an angle of 85–92° (40–45° in *L. mendeleevi*), the bending that starts behind the skull (just before the level of the anus in *L. mendeleevi*), and the naked skin without striae (with numerous, closely-set, oblique striae consisting of minute tubercles in *L. mendeleevi*). From other gobiesocids, it is distinguished by the characters of the subfamily (see above).

3.4.7. Remarks

This species is highly asymmetrical. While the head is normally orientated, the skull is already slightly asymmetrical when seen from the front (Fig. 3B), with an oblique mouth slit and the left eye situated lower than the right eye in the male holotype; the vertebral column inserts slightly on the left-hand side of the skull (Fig. 2B), and then strongly turns left, meeting the left-hand side of the body on the level of the dorsal fin insertion; it continues running along the left-hand side towards the hypural plate. The anal fin, consequently, inserts on the right-hand side of the body; the caudal fin lies flat on the ground. Asymmetries are also found in the position of the internal organs, which are restricted to the right half of the body (Fig. 2C); the anus is situated on the right-hand side. Asymmetries are observed also in the pectoral and pelvic fin skeletons; the fins and supporting elements on right-hand side and are much smaller than the corresponding elements on the left-hand side (disc asymmetry, see Fig. 3C). In the female paratype, the asymmetries are the other way around, with the vertebral column turning towards the right-hand side of the fish, and the anus and the internal organs shifted towards the left-hand side. These asymmetries are not artificial, as all four specimens of the type series show exactly the same pattern, which was already apparent in the freshly collected fish.

The right pectoral fins, and right lobes of the pelvic disc, were partially removed for molecular studies prior to the morphological examination.

This new species is found in relatively cool water in an area with temporary upwelling along the northern coast of Papua New Guinea (Kuroda [70], Lee et al. [71], Hasegawa et al. [72]). It was found in association with sunken logs; its specializations and especially the lateral asymmetry may be useful to be attached to these logs.

3.5. *Lepadicyathus* Prokofiev, 2005 (Fig. 6)

3.5.1. Synonymy

Lepadicyathus Prokofiev 2005: Prokofiev [42]: 559 [546] (type species: *Lepadicyathus mendeleevi* Prokofiev 2005 by original designation (also monotypic).

3.5.2. Diagnosis

A genus of protogobiesocine fishes with a partial lateral asymmetry; head slightly asymmetrical when seen from the front; vertebral column bent towards the left in males, towards the right in females, at an angle of 40–45°; bending starts slightly before level of anus; anus situated towards the right-hand side of the body in males, towards the left-hand side in females; position of guts slightly asymmetrical; gills 3; pelvic fin disc rudimentary, in two parts, with a few rudimentary papillae basally in region B. Dorsal fin with 11–12 rays; anal fin with 10 rays; caudal fin with 10 principal rays. Skin naked, surface of head and body covered with a dense pattern of obliquely arranged striae consisting of minute tubercles.

3.5.3. Description

Dorsal-fin rays xi–xii; anal-fin rays x; pectoral-fin rays xxiv; caudal-fin rays (v),x,(v). No gill rakers on 3rd arch; 1–2 gill rakers on the 1st and 2nd arches.

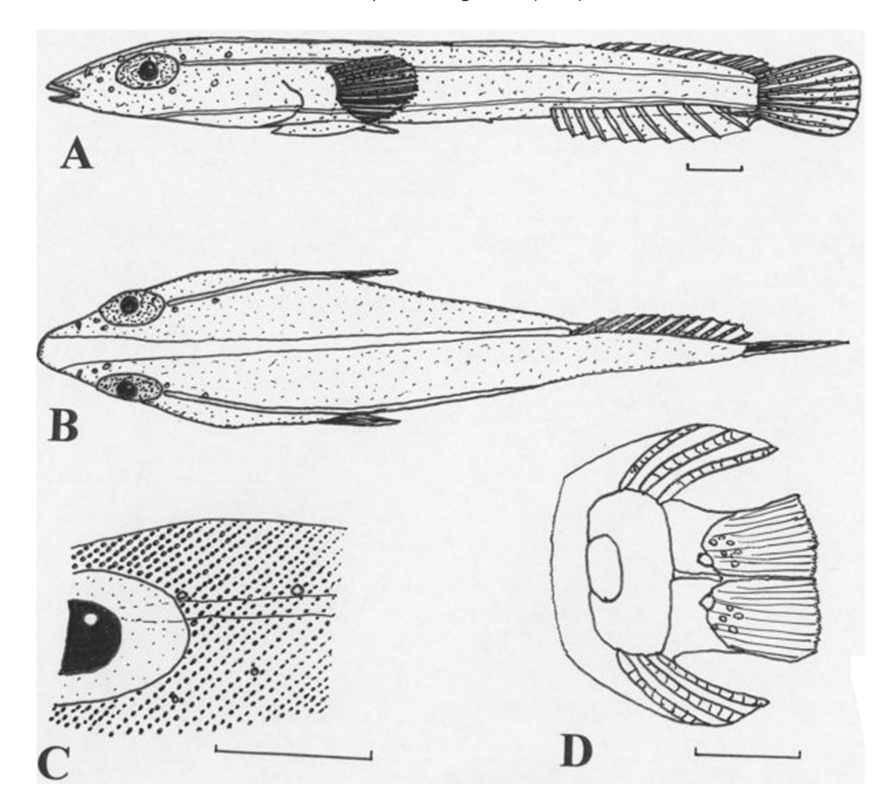


Fig. 6. *Lepadicyathus mendeleevi* Prokofiev, 2005, ZIN 53413, holotype, female, 13.6 mm SL, Papua New Guinea, Madang Province, near Bongu. **A** (upper) Lateral view. **B** (centre) dorsal view. **C** (lower left) detail of postorbital region showing striae. **D** (lower right) pelvic disc. Bars: 1 mm.

Premaxillary with a single row of incisor-like teeth, some with a hook-like appendage. Dentary with a single row of smaller incisor-like teeth, fused at the bases.

Head lateral line system with 2 pores in the nasal canal, 2 pores in the postorbital canal, 2 pores in the lacrimal canal, and 2 pores in the preopercular canal, pores in mandibular canal lacking.

Pelvic disc rudimentary, in two parts; anterior margin with small fringes; disc only with a few rudimentary papillae basally in region B.

Skin naked; surface of head and body covered with a dense pattern of obliquely arranged striae consisting of minute tubercles (Fig. 6C).

3.5.4. Remarks

The dermal striae found in *Lepadicyathus* are an unusual, specialised character not found in other gobiesocids. Prokofiev [42] compared it with *Liobranchia stria* of Briggs [3], which has deep grooves in the skin, but the state of *Liobranchia* is quite different from that of *Lepadicyathus*. *Liobranchia* has just grooves surrounded by folds, while the skin of *Lepadicyathus* is even, but covered with striae consisting of minute tubercles. This seems to be an independent specialisation, though we are unaware of the function of these striae. The tubercles may be based on reduced scales, which would support the primitive state of *Lepadicyathus*.

3.6. Lepadicyathus mendeleevi *Prokofiev, 2005 (Fig. 6)*

Mendeleev's clingfish.

3.6.1. Synonymy

Lepadicyathus mendeleevi Prokofiev 2005: Prokofiev [42]: 560 (547) (Papua New Guinea, near village of Bongu, Madang Province, 1 m depth. Holotype: ZIN 53413). Prokofiev [73]: 181 (discussion on systematic position).

3.6.2. Material

ZIN 53413 (holotype, female, 13.6 mm SL), Papua New Guinea, Madang Province, near Bongu, 1 m depth, in *Millepora* coral, R/V Dmitrii Mendeleev, Cruise 18,14 Feb. 1977. ZIN 53413a (1 paratype, male, 13.9 mm SL), same data as the holotype.

3.6.3. Diagnosis

Dorsal fin with 11–12 rays, anal fin with 10 rays, pectoral fin with 24 rays, principal caudal-fin rays 10, three gills, third arch without gill rakers. Vertebral column with a total of 33 vertebrae, with asymmetrical bending staring just before the level of the anus, bent at an angle of 40–45°. Skull not asymmetrical in frontal view. Skin naked, surface of head and body, with numerous, closely set, oblique striae consisting of minute tubercles. Disc without adhesive papillae, except a few basally in region B, arranged in two rows; posterior margin not fringed; region B small, left and right-hand sides connected by a membrane.

3.6.4. Description

Dorsal-fin rays xii (xi); anal-fin rays x (x); pectoral-fin rays xxiv (xxiv); caudal-fin rays (v),x,(v) [(v),x,(v)]. Gills 3 (3); no gill rakers on 3rd arch; 1-2 gill rakers on 1st and 2nd

Table 4
Counts and measurements of the holotype and paratype of *Lepadicyathus mendeleevi* Prokofiev, 2005.

	Holotype ZIN 53413 Female	Paratype ZIN 53413a Male
Standard length	13.6	13.9
Head length	4.9	4.4
Body depth	1.5	1.5
Body width	2.9	2.8
Orbit diameter	1.4	1.7
Preorbital length	1.2	1.5
Interorbital distance	1.0	1.0
Upper jaw length	0.6	0.6
Lower jaw length	0.4	0.4
Preanus length	8.4	10.3
Urogenital papilla	0.05	–
PC length	0.5	0.6
PC depth	1.1	1.2
PC width	0.7	0.8
Predorsal length	10.1	10.4
Preanal length	9.7	11.3
Distance disc to anus	1.2	2.4
Distance anus to anal-fin origin	1.2	2.45
Prepectoral length	5.5	5.8
Predisc length	4.4	4.1
1st dorsal ray	1.1	1.2
Last dorsal ray	ca. 0.8	1.0
Dorsal-fin base	3.0	4.4
1st anal ray	1.0	1.1
Last but one anal ray	1.4	1.5
Last anal ray	0.9	1.0
Anal-fin base length	2.4	2.9
Pectoral-fin length	1.5	1.3
Pectoral-fin base	1.0	1.4
Disc length	2.5	2.6
Caudal-fin length	1.9	ca. 1.8

mm: measurements; PC: Caudal peduncle.

arches. Measurements of the holotype and paratypes: see Table 4.

Premaxillary with a single row of incisor-like teeth, some with a hook-like appendage. Dentary with a single row of smaller incisor-like teeth, fused at bases.

Head lateral line system with 2 pores in the nasal canal, 2 pores in the postorbital canal, 2 pores in the lacrimal canal, and 2 pores in the preopercular canal, pores in the mandibular canal lacking.

Vertebrae 33 (15 + 18); asymmetrical bending of vertebral column starting from 11th vertebra. Pleural ribs 12 pairs.

Head moderately broad, depressed. Head and skull slightly asymmetrical in frontal view. Head length 36.0 (31.6)% SL (2.8–3.2 in SL). Maximum body depth 11.9 (10.8)% SL (9.1–9.4 in SL). Maximum body width 21.3 (20.1)% SL (4.7–5.0 in SL). Maximum (horizontal) orbit diameter 10.3 (12.2)% SL (2.6–3.5 in head length). Snout elongate, slightly pointed, tip rounded (Fig. 6B). Preorbital length 8.8 (10.8)% SL (2.9–4.1 in head length), in the male not longer than in the female. Interorbital distance 7.4 (7.2) %SL (4.4–4.9 in head length). Upper jaw length 4.4 (4.3)% SL. Lower jaw length 2.9 (2.9)% SL. Gill membranes attached to the isthmus. Body bent to the left-hand side (male) or the right-hand side (female); vertebral column bent at an angle of 40° (45°), bending starts just before the level of the anus. Anus situated in the middle between the disc and anal-fin origin; both sexes with a short urogenital papilla; distance between disc and anus 8.8 (17.3)% SL, distance between anus and anal-fin origin 8.8 (17.6)% SL. Anus situated only slightly towards the right-hand side of the body (male) or the left-hand side of the body (female). Pre-anus length 61.8 (74.1)% SL (1.4–1.6 in SL). Sides of body without an elongate dermal fold below the base of the anal fin. Caudal-peduncle length 3.7 (4.3)% SL (23.2–27.2 in SL). Caudal-peduncle depth 8.1 (8.6)% SL (11.6–12.4 in SL). Caudal-peduncle width 5.1 (5.8)% of SL (17.3–19.4 in SL).

Predorsal-fin length 74.3 (74.8)% SL (1.3-1.4 in SL). Preanal-fin length 71.3 (81.3)% SL (1.2–1.4 in SL). Dorsal fin origin towards the left-hand side of the body (male), the right-hand side of the body (female); anal fin origin near the right-hand side of the body (male), the left-hand side of the body (female). Prepectoral-fin length 40.4 (41.7)% SL (2.4-2.5 in SL). Predisc length 32.3 (29.5)% SL (3.1–3.4 in SL). Disc length 18.4 (18.7)% SL (5.3–5.4 in SL). Disc membrane inserting at the base of the 12th (16th) pectoral-fin ray. Pelvic disc rudimentary, in two parts; anterior margin of region A and posterior margin of region B with small fringes; disc only with a few rudimentary papillae basally in region B. Caudal-fin length 14.0% SL (7.2 in SL). Skin naked; surface of head and body covered with a dense pattern of obliquely arranged striae consisting of minute tubercles (Fig. 6C).

Colour in life.–Unknown.

Colour in alcohol.–The holotype and paratype are reddish brown, the head and anterior dorsal surface carmesine red, with 5 white stripes; one stripe running from the tip of the snout along the dorsal midline to the dorsal-fin base (Fig. 6B), a lateral stripe on each side from posterior margin of eye to the dorsal part of the caudal peduncle, and another lateral stripe on each side from below the dentary to the lower part of the caudal peduncle. Eye dark grey. Occiput not transparent. Fins reddish; caudal fin with a basal brown spot, central part of fin carmesine red.

3.6.5. Distribution

North coast of Papua New Guinea (Madang Province) (Fig. 7). This new species is known only from the type locality. It was collected at a depth of 1 m, inhabiting a *Millepora* coral.

3.6.6. Remarks

Prokofiev [42] noticed that the paratype of *Lepadicyathus mendeleevi* was "crumpled", but thought this to be artificial, and was apparently not aware of the lateral asymmetry. During a re-examination, however, the moderate asymmetry of this species was discovered both in the holotype and the paratype. In the female holotype, an ovary full of moderately large eggs was visible in the X-ray image.

While the head is normally orientated, the skull is already slightly asymmetrical when seen from the front, with a slightly oblique mouth slit and one cheek larger than the other; in the female holotype, the vertebral column is bent towards the right-hand side (Fig. 6B), with

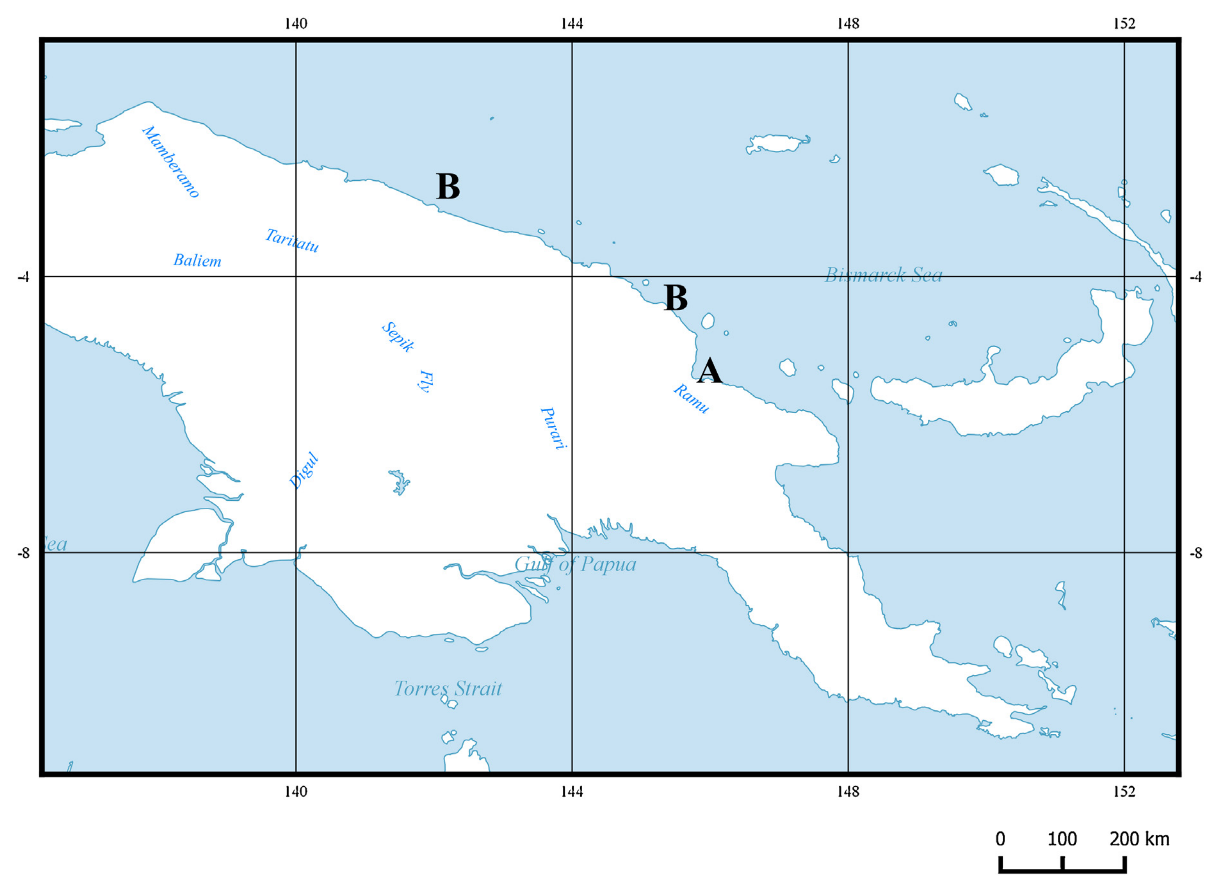


Fig. 7. Geographical distribution of the species of the subfamily Protogobiesocinae n. subfam. in Papua New Guinea. **A**. *Lepadicyathus medeleevi*. **B**. *Protogobiesox asymmetricus* gen. nov., sp. nov.

the anus placed slightly towards the left-hand side of the body; the vertebral column is bent to the left-hand side in the male paratype, with the anus closer to the right-hand side. A slight asymmetry is also found in the position of the internal organs, which are shifted towards the left-hand side of the body in the female holotype, but towards the right-hand side of the body in the male paratype.

In a note published subsequently to the original description, Prokofiev [73] noted that the absence of papillae on the disc of *Lepadicyathus mendeleevi* is not unique in Gobiesocidae, but resembles young specimens of the genus *Lepadichthys*. However, the holotype of *L. mendeleevi* is certainly to be considered as an adult specimen, as the ovary is full of eggs.

4. Discussion

Chen et al. [60], in a molecular phylogenetic analysis of the Acanthomorpha, demonstrated that the order Perciformes is polyphyletic, and that several of the discovered clades need formal recognition. From the phylogenetic results of Chen et al. [60], the Gobiesocidae formed a separate clade (Clade D) together with the blennioids; this clade was nested within the inferred clade Q (Chen et al. [60]; Dettaï & Lecointre [61]) or Ovalentaria (Wainwright et al. [74]) of the Percomorpha contained Atherinomorpha, Mugilidae, Pomacentridae ("Labroidei"), Cichlidae ("Labroidei"), Embiotocidae ("Labroidei"), Ambassidae, and some other perciform fishes from Pholidichthyidae, Pseudochromidae, Polycentridae, Plesiopidae, Opistognathidae, and Grammatidae (Near et al. [62]). Our phylogenetic result, by including the main taxa from the clade Q, confirms the previous hypothesis (Fig. 1), and suggest the clade including Blennioidei and Gobiesocidae should be formally named in the future. Very recently, Nelson et al. [75] classified the Gobiesociformes as a separate order for the single family Gobiesocidae, which they considered as closely related to the Blenniiformes (= Blennioidei) (see Lin & Hastings [76]). However, the authors these studies did not give the reason for their rearrangement of the taxonomic rank at the ordinal level; the classification should further be settled.

Within the family Gobiesocidae, a total of 9 subfamilies were previously distinguished (Briggs [3], Conway et al. [56]); five of these were included for the present molecular phylogenetic investigation. The new subfamily Protogobiesocinae is morphologically most similar to the subfamily Aspasminae. Species of the Aspasminae are distributed from East Africa east to Mariana Islands, north to Japan, south to southern Australia and New Zealand; they are known from very shallow to moderately deep water. The deepest occurring aspasmine species are *Aspasma minima*

(Döderlein, 1887) from Japan (183–274 m), and *Modicus tangaroa* Hardy, 1983 from New Zealand (20–149 m). However, our molecular results revealed that the sister-group of the Aspasminae is the Diademichthyinae, a group of the Indo-West Pacific distributed clingfishes specialized for a commensal relationship with certain shallow-reef crinoids. Interestingly, the enigmatic clingfishes from the subfamily Cheilobranchinae turned out to be the sister-group of the Aspasminae/Diademichthyinae clade in the inferred phylogenetic tree (Fig. 1). The species in the new subfamily Protogobiesocinae also possess a reduced or "ancestral" form of their adhesive disc formed by the pelvic fins, similar to the species of Cheilobranchinae. According to our phylogeny, this feature is apparently a derived state and has been evolved twice within the Gobiesocidae

Acknowledgments

The "Our Planet Reviewed" PAPUA NIUGINI Biodiversity Expedition was a joint project of Pro-Natura International (PNI), "Muséum national d'histoire naturelle", Paris (MNHN), "Institut de recherche pour le développement" (IRD) and the University of Papua New Guinea (UPNG) – the principal investigators were Philippe Bouchet, Claude Payri, and Sarah Samadi. The organizers acknowledge funding from the Total Foundation, the Prince Albert II of Monaco Foundation, the Fondation EDF, the Stavros Niarchos Foundation and Entrepose Contracting, Fonds Pacifique, the Government of New Caledonia, and the kind support from the Divine Word University (DWU). The expedition operated under a permit delivered by the Department of Environment and Conservation of Papua New Guinea.

We appreciate the support by Sarah Samadi (MNHN, Paris) who provided information on station data and photographs of specimens collected during the PAPUA NIUGINI Biodiversity Expedition. We would also like to thank M. McGrouther, D.F. Hoese and J.R. Paxton (AMS, Sydney), D. Didier (ANSP, Philadelphia), O. Crimmen, J. Maclaine, A. Wheeler and P.J.P. Whitehead [†] (BMNH, London), J.E. Randall and A.Y. Suzumoto (BPBM, Honolulu), L.J. Dempster, W.N. Eschmeyer, M. Hearne, T. Iwamoto and P.M. Sonoda (CAS-SU, San Francisco), A. Brito (CCML, La Laguna, Tenerife), M.-L. Bauchot, M. Desoutter, G. Duhamel and P. Pruvost (MNHN, Paris), H. Ahnelt, R. Hacker [†] and P. Kähsbauer [†] (NMW, Vienna), K. Matsuura (NSMT-P, Tokyo), M.E. Anderson and V. Mthombeni (SAIAB, Grahamstown), J.T. Williams (USNM, Washington D.C.), A.V. Balushkin (ZIN, St. Petersburg), M.A. Krag, P.R. Møller and J.C. Nielsen (ZMUC, Copenhagen) and who gave access to specimens in their care, and provided information and/or photographs. We are grateful to M.J. Zhukov (ZIN, St. Petersburg) who provided assistance and prepared x-rays of *Lepadicyathus mendeleevi*., and to G. Duhamel and P. Pruvost (MNHN, Paris) who provided a catalogue number for a paratype. We wish to thank Kevin Conway, Bruno Chanet, Masaki Miya and The Australian Museum Sydney (via Mark McGrouther) for the loan or gift of tissue samples. WJC appreciates the grant support from the Ministry of Science & Technology, Taiwan (MOST 102-2923-B-002 -001-MY3).

References

[1] G.S. Hardy, A new genus and species of deepwater clingfish (family Gobiesocidae) from New Zealand, Bull. Mar. Sci. 34 (1984) 244–247.
[2] J.B. Hutchins, Description of a new deepwater clingfish (Gobiesocidae) from New South Wales, Rec. W. Austr. Mus. 15 (2) (1991) 463–468.
[3] J.C. Briggs, A monograph of the clingfishes (order Xenopterygii), Stanford Ichthyol. Bull. 6 (1955), i-iv+1-224.
[4] V.G. Springer, T.H. Fraser, Synonymy of the fish families Cheilobranchidae (=Alabetidae) and Gobiesocidae, with descriptions of two new species of *Alabes*, Smithsonian Contr. Zool. 234 (1976), i-iii+1-i-iii+23.
[5] J.C. Briggs, A new genus and two new species of Eastern Atlantic clingfishes, Copeia (1957) 204–208.
[6] J.L.B. Smith, Fishes of Aldabra, Part VIII, Ann. Mag. Nat. Hist. (12) 10 (113) (1957) 395–400, pls. 13-14.
[7] J.C. Briggs, A new clingfish of the genus *Gobiesox* from the Tres Marias Islands, Copeia 1960 (3) (1960) 215–217.
[8] J.C. Briggs, R.R. Miller, Two new freshwater clingfishes of the genus *Gobiesox* from southern Mexico, Occas. Pap. Mus. Zool. Univ. Michigan 616 (1960) 1–15, pls. 1-4.
[9] J.C. Briggs, A new clingfish of the genus *Lepadichthys* from the New Hebrides, Copeia (1962) 424–425.
[10] J.C. Briggs, A new clingfish of the genus *Gobiesox* from the Bahamas, Copeia (1963) 604–606.
[11] J.C. Briggs, G. Link, New clingfishes of the genus *Lepadichthys* from the northern Indian Ocean and Red Sea (Pisces, Gobiesocidae), Senckenb. Biol. 44 (1963) 101–105.
[12] A.A. Murgoci, Contribution à la connaissance des gobiesocides (ordre des Xenopterygii) de la mer Noire, Rev. Roum. Biol., Sér. Zool. 9 (5) (1964) 297–306.
[13] J.L.B. Smith, The clingfishes of the western Indian Ocean and the Red Sea, Ichthyol. Bull. Dep. Ichthyol. Rhodes Univ. 30 (1964) 581–596, pls. 92-97.
[14] J.C. Briggs, Gobiesocidae, pp. 651-656, in: J.C. Hureau, T. Monod (Eds.), Check-list of the fishes of the north-eastern Atlantic and of the Mediterranean, Volume 1, CLOFNAM, UNESCO, Paris, 1973, pp. i–xxii+1-683.
[15] J.C. Briggs, A new clingfish of the genus *Lepadichthys* from the Red Sea, (Contribution to the knowledge of the Red Sea, no. 35), Bull. Min. Agric. Dep. Fish. Sea Fish. Res. Stat. Haifa 42 (1966) 37–40.
[16] J.L.B. Smith, A new clingfish from southern Mozambique, Ann. Mag. Nat. Hist. (13) 8 (95) (1966) 641–644 (pl. 19).
[17] J.C. Briggs, A new clingfish (Gobiesocidae) of the genus *Tomicodon* from Ecuador, Copeia (1969) 75–76.
[18] J.C. Briggs, A new genus and species of clingfish (family Gobiesocidae) from the Bahama Islands, Copeia (1969) 332–334.
[19] J.C. Briggs, A new species of *Lepadichthys* (Gobiesocidae) from the Seychelles, Indian Ocean, Copeia (1969) 464–466.
[20] J.C. Briggs, The clingfishes (Gobiesocidae) of Panama, Copeia (1969) 774–778.
[21] W.F. Smith-Vaniz, A new clingfish, *Tomicodon rhabdotus* family Gobiesocidae, from the Lesser Antilles, Proc. Biol. Soc. Washington 81 (1969) 473–477.
[22] J.E. Böhlke, C.R. Robins, A new genus and species of deep-dwelling clingfish from the Lesser Antilles, Notul. Nat. 434 (1970) 1–12.
[23] T.H. Fraser, Two new species of the clingfish genus *Derilissus* (Gobiesocidae) from the western Atlantic, Copeia (1970) 38–42.
[24] W.F. Smith-Vaniz, Another new species of the clingfish genus *Derilissus* from the western Atlantic (Pisces: Gobiesocidae), Copeia (1971) 291–294.
[25] J.C. Briggs, A new genus and species of clingfish from the western Pacific, Copeia (1976) 339–341.
[26] G.R. Hardy, A new genus and two new species of clingfishes (Gobiesocidae) from New Zealand, Copeia (1983) 863–868.
[27] J.B. Hutchins, Redescription of the clingfish *Cochleoceps spatula* (Gobiesocidae) from Western Australia and South Australia, with the description of a new species from Victoria and Tasmania, Rec. W. Austr. Mus. 11 (1) (1983) 33–47.
[28] M. Shiogaki, Y. Dotsu, Two new genera and two new species of clingfishes from Japan, with comments on head sensory canals of the Gobiesocidae, Jap. J. Ichthyol. 30 (2) (1983) 111–121.
[29] G.S. Hardy, A new genus and species of deepwater clingfish (family Gobiesocidae) from New Zealand, Bull. Mar. Sci. 34 (2) (1984) 244–247.
[30] J.B. Hutchins, Description of a new gobiesocid fish from south-western Australia, with a key to the species of *Aspasmogaster*, Rec. W. Austr. Mus. 11 (2) (1984) 129–140.
[31] W.A. Szelistowski, A new clingfish (Teleostei: Gobiesocidae) from the mangroves of Costa Rica, with notes on its ecology and early development, Copeia (1990) 500–507.

[32] J.B. Hutchins, Description of a new deepwater clingfish (Gobiesocidae) from New South Wales, Rec. W. Austr. Mus. 15 (1991) 463–468.
[33] J.C. Briggs, New genus and species of clingfish (Gobiesocidae) from southern Australia, Copeia (1993) 196–199.
[34] H. Espinosa Pérez, J.L. Castro-Aguirre, A new freshwater clingfish (Pisces: Gobiesocidae) from Baja California Sur, México, Bull. S. Calif. Acad. Sci. 95 (3) (1996) 120–126.
[35] R. Hofrichter, R.A. Patzner, A new species of *Apletodon* from the Mediterranean Sea and the eastern Atlantic with notes on the differentiation between *Apletodon* and *Diplecogaster* species (Pisces: Teleostei: Gobiesociformes: Gobiesocidae), Senckenb. Biol. 77 (1997) 15–22.
[36] J.C. Briggs, New species of *Lepadichthys* from the Philippine Islands, Copeia (2001) 499–500.
[37] J.C. Briggs, New clingfish (Gobiesocidae) from Isla Grande, Colombia, Copeia (2001) 745–746.
[38] J.C. Briggs, New species of Rimicola from California, Copeia (2002) 441–444.
[39] J.T. Williams, J.C. Tyler, Revision of the Western Atlantic clingfishes of the genus *Tomicodon* (Gobiesocidae), with descriptions of five new species, Smithson Contrib Zool. 621 (2003) 1–26.
[40] J.B. Hutchins, S. Morrison, Five new species of the genus *Alabes* (Gobiesocidae: Cheilobranchinae), Rec. Austr. Mus. 56 (2) (2004) 147–158.
[41] C.L.S. Sampaio, J. de Anchieta, C.C. Nunes, L.F. Mendes, *Acyrtus pauciradiatus*, a new species of clingfish (Teleostei: Gobiesocidae) from Fernando de Noronha Archipelago, Pernabuco State, northeastern Brazil, Neotrop. Ichthyol. 2 (4) (2004) 205–208.
[42] A.M. Prokofiev, A new genus and species of clingfish (Gobiesociformes: Gobiesocidae) from New Guinea, Vopr. Ikht. 45 (4) (2005) 559–563, [In Russian. English translation appeared in *J. Ichthyol*. 45 (7) 2005, 546–550].
[43] J.B. Hutchins, Description of two new species of shore-eels (Gobiesocidae: Cheilobranchinae: Alabes) from south-eastern Australia and Norfolk Island, Mem. Mus. Vict. 63 (1) (2006) 25–28.
[44] R. Fricke, A new species of the clingfish genus *Apletodon* (Teleostei: Gobiesocidae) from Sao Tome and Principe, Eastern Central Atlantic, Ichthyol. Res. 54 (2007) 68–73.
[45] M.T. Craig, J.E. Randall, Two new species of the Indo-Pacific clingfish genus *Discotrema* (Gobiesocidae), Copeia (2008) 68–74.
[46] M.T. Craig, J.E. Randall, *Briggsia hastingsi*, a new genus and species of clingfish from Oman, Zootaxa 2271 (2009) 64–68.
[47] R. Fricke, P. Wirtz, A. Brito, A new species of the clingfish genus *Apletodon* (Teleostei: Gobiesocidae) from the Cape Verde Islands, Eastern Central Atlantic, Ichthyol. Res. 57 (2010) 91–97.
[48] G.R. Allen, M.V. Erdmann, Reef fishes of the East Indies, Volumes I-III, Tropical Reef Research, Perth, 2012.[vol. I: pp. x+1-424+end note; vol. II: pp. 425-855; vol. III: preface, map, contents and pp. 857-1260; including Appendix 1 (new species descriptions) and Appendix II (addendum).].
[49] G.I. Moore, J.B. Hutchins, M. Okamoto, A new species of the deepwater clingfish genus *Kopua* (Gobiesociformes: Gobiesocidae) from the East China Sea – an example of antitropicality? Zootaxa 3380 (2012) 34–38.
[50] J.S. Sparks, D.F. Gruber, A new mesophotic clingfish (Teleostei: Gobiesocidae) from the Bahamas, Copeia (2012) 251–256.
[51] K.W. Conway, C.C. Baldwin, M.D. White, Cryptic diversity and venom glands in Western Atlantic clingfishes of the genus *Acyrtus* (Teleostei: Gobiesocidae), PLoS ONE 9 (5) (2014) 1–17 (art. e97664).
[52] R. Fricke, *Unguitrema nigrum*, a new genus and species of clingfish (Teleostei: Gobiesocidae) from Madang, Papua New Guinea, J. Ocean Sci. Found. 13 (2014) 35–42.
[53] R. Fricke, P. Wirtz, A. Brito, *Diplecogaster tonstricula*, a new species of cleaning clingfish (Teleostei: Gobiesocidae) from the Canary Islands and Senegal, eastern Atlantic Ocean, with a review of the *Diplecogaster-ctenocrypta* species-group, J. Nat. Hist. 50 (11–12) (2015) 731–748.
[54] G. Shinohara, E. Katayama, A new species of the clingfish genus *Kopua* Gobiesociformes: Gobiesocidae) from Japan [Electronic prepublication], Ichthyol. Res. (2015) 1–8.
[55] M.T. Craig, S.V. Bogorodsky, J.E. Randall, A.O. Mal, *Lepadichthys bilineatus*, a new species of clingfish from Oman (Teleostei: Gobiesocidae), with a redescription of *Lepadichthys erythraeus* Briggs and Link from the Red Sea, Zootaxa 3990 (1) (2015) 113–122.
[56] K.W. Conway, N.G. Bertrand, Z. Browning, T.W. Lancon, F.J. Clubb Jr., Heterodonty in the New World: An SEM investigation of oral jaw dentition in the clingfishes of the subfamily Gobiesocinae (Teleostei: Gobiesocidae), Copeia 103 (4) (2015) 973–998.
[57] R. Fricke, A method of counting caudal fin rays of actinopterygian fishes, Braunschw. Naturk. Schr. 1 (1983) 729–733.
[58] R. van der Laan, W.N. Eschmeyer, R. Fricke, Family-group names of recent fishes, Zootaxa 3882 (2) (2014) 1–230.
[59] W.-J. Chen, C. Bonillo, G. Lecointre, Repeatability of clades as a criterion of reliability: a case study for molecular phylogeny of Acanthomorpha (Teleostei) with larger number of taxa, Mol. Phylogenet. Evol. 26 (2003) 262–288.
[60] W.-J. Chen, R. Ruiz-Carus, G. Ortí, Relationships among four genera of mojarras (Teleostei: Perciformes: Gerreidae) from the western Atlantic and their tentative placement among percomorph fishes, J. Fish Biol. 70 (2007) 202–218.
[61] A. Dettaï, G. Lecointre, Further support for the clades obtained by multiple molecular phylogenies in the acanthomorph bush, C. R. Biologies 328 (2005) 674–689.
[62] T.J. Near, A. Dornburg, R.I. Eytan, B. Keck, W.L. Smith, K.L. Kuhn, J.A. Moore, S.A. Price, F.T. Burbrink, M. Friedman, P.C. Wainwright, Phylogeny and tempo of diversification in the superradiation of spiny-rayed fishes, Proc. Natl. Acad. Sci. U. S. A. 110 (2013) 12738–12743.
[63] P.-C. Lo, S.-H. Liu, N.L. Chao, F.K.E. Nunoo, H.-K. Mok, W.-J. Chen, A multi-gene dataset reveals a tropical New World origin and Early Miocene diversification of croakers (Perciformes: Sciaenidae), Mol. Phylogenet. Evol. 88 (2015) 132–143.
[64] R.C. Edgar, MUSCLE: multiple sequence alignment with high accuracy and high throughput, Nucl. Acids Res. 32 (2004) 1792–1797.
[65] A. Rambaut, Sequence alignment editor version 1.0 a1. (1996) Available from http://evolve.zoo.ox.ac.uk/Se-Al/Se-Al.html.
[66] A. Stamatakis, RAxML-VI-HPC: maximum likelihood-based phylogenetic analyses with thousands of taxa and mixed models, Bioinformatics 22 (2006) 2688–2690.
[67] Z. Yang, Maximum likelihood phylogenetic estimation from DNA sequences with variable rates over sites: approximate methods, J. Mol. Evol. 39 (1994) 306–314.
[68] J. Felsenstein, Confidence limits on phylogenies: an approach using the bootstrap, Evolution 39 (1985) 783–791.
[69] R. Fricke, W.N. Eschmeyer, Guide to fish collections in the Catalog of fishes. Online version, updated 9 August 2016, Internet publication, California Academy of Sciences, San Francisco, http://research.calacademy.org/research/Ichthyology/Catalog/collections.asp.
[70] Y. Kuroda, Variability of currents off the northern coast of New Guinea, J. Oceanogr. 56 (2000) 103–116.
[71] T. Lee, I. Fukumori, D. Menemenlis, Z.-F. Xing, L.-L. Fu, Effects of the Indonesian throughflow on the Pacific and Indian Oceans, J. Phys. Oceanogr. 32 (2002) 1404–1429.
[72] T. Hasegawa, K. Ando, K. Mizuno, R. Lukas, Coastal upwelling along the north coast of Papua New Guinea and SST cooling over the Pacific warm pool: a case study for the 2002/03 El Niño event, J. Oceanogr. 65 (2009) 817–833.
[73] A.M. Prokofiev, Systematic position of *Lepadicyathus mendeleevi* (Teleostei: Gobiesocidae), Aktual'niie Problemii Sobremennoi Nauki 1 (7) (2007) 181–182 [in Russian].
[74] P.C. Wainwright, W.L. Smith, S.A. Price, K.L. Tang, J.S. Sparks, L.A. Ferry, K.L. Kuhn, R.I. Eytan, T.J. Near, The evolution of pharyngognathy: a phylogenetic and functional appraisal of the pharyngeal jaw key innovation in labroid fishes and beyond, Syst. Biol. 61 (2012) 1001–1027.
[75] J.S. Nelson, T.C. Grande, M.V.H. Wilson, Fishes of the world, 5th ed., NJ (Wiley), Hoboken, 2016, i–xli+1-707.
[76] H.-C. Lin, P.A. Hastings, Phylogeny and biogeography of a shallow water fish clade (Teleostei: Blenniiformes), BMC Evol. Biol. 13 (2013) 1–18.